

CERN-THESIS-2022-154  
CERN-PBC-NOTES-2022-007

2022-10-14

David.Mate.Parragh@cern.ch

## Hydrogen Embrittlement of TiZrV Non-Evaporable Getter Coating

*D.M. Parragh*

Catholic University of Leuven, Leuven, Belgium

**Keywords:** LHCb, SMOG, gas target, TiZrV, NEG coating, hydrogen embrittlement

---

### Abstract

The study presented in this thesis work was performed to gain better understanding on the hydrogen saturation behavior of the TiZrV NEG coating, as well as on the effects of hydrogen sorption on the functionality of the coating. H<sub>2</sub> saturation experiments were conducted on two TiZrV coated stainless steel pipes subjected to two experimental conditions: instantaneous injections of H<sub>2</sub> at 1 mbar injection pressure throughout 6 cycles, and continuous injection of H<sub>2</sub> at  $5 \times 10^{-7}$  mbar to simulate saturation behavior at conditions similar to that of the H<sub>2</sub> injections part of the fixed target experiments at the LHCb experiment. The results demonstrated that at the injected hydrogen quantities, the sticking coefficient and the H<sub>2</sub> sorption rate of the TiZrV coating show a clear dependence on the absorbed hydrogen content, both decreasing at increased hydrogen absorption. The H<sub>2</sub> sorption limit was established as at minimum 0.407 H/TiZrV mol/mol at the 1 mbar injection condition and as 0.026 H/TiZrV mol/mol at the  $5 \times 10^{-7}$  mbar continuous injection condition. Visual signs of embrittlement were not observed on the coating in the stainless steel pipes, proving the TiZrV alloy robust against hydrogen embrittlement. While embrittlement was not observed on the coating on the stainless steel pipes, the residual hydrogen content was observed to impose a limit on the H<sub>2</sub> sticking coefficient of the coating, highlighting the importance of ensuring sufficiently high hydrogen release kinetics and hydrogen removal rate during the reactivation. Besides, by characterization of witness samples from the 1 mbar injection experimental condition it was determined that the repeated cycles of activation, H<sub>2</sub> injection, and venting decrease the efficiency of activation, motivating further investigation on the effect of hydrogen sorption on the activatability and the SEY of the NEG coating.

---

# Hydrogen Embrittlement of TiZrV Non-Evaporable Getter Coating

Dávid Máté Parragh

Thesis submitted for the degree of  
Master of Science in Materials  
Engineering, option Metals and  
Ceramics

**Thesis supervisors:**

Prof. dr. ir. Martine Wevers  
Prof. dr. ir. Jozef Vleugels  
Ir. Ivo Wevers

**Assessors:**

Prof. dr. ir. Marc Seefeldt  
Prof. dr. ir. Maria Seo

**Mentors:**

Ir. Josef Sestak  
Dr. ir. Giuseppe Bregliozzi

© Copyright KU Leuven

Without written permission of the thesis supervisors and the author it is forbidden to reproduce or adapt in any form or by any means any part of this publication. Requests for obtaining the right to reproduce or utilize parts of this publication should be addressed to Dept. MTM - KU Leuven, Kasteelpark Arenberg 44 bus 2450, B-3001 Heverlee.

A written permission of the thesis supervisors is also required to use the methods, products, schematics and programmes described in this work for industrial or commercial use, and for submitting this publication in scientific contests.

# Preface

*“Ezért tehát nem azé, aki akarja, és nem is azé, aki fut, hanem a könyörülő Istené.”*  
Róma 9:16



There is an innumerable amount of people I would like to thank, and in fact, I will not be able to provide a fully exhaustive list of everyone I am grateful for for supporting me in the achievement of having written this thesis.

First of all, I would like to thank all my professors and educators at MTM who taught, inspired, and motivated me during my journey in the master’s program. I am especially indebted to my supervisors, Prof. Wevers and Prof. Vleugels, without whose guidance, challenging questions, and thorough supervision I couldn’t have completed this thesis project, and I would like to express my most sincere gratitude to both of them.

I would also like to thank all my colleagues in the Vacuum, Surfaces and Coating group at CERN who provided an exceptionally welcoming environment. I would specifically like to thank my supervisors Ivo Wevers, Giuseppe Bregliozzi, and Josef Sestak, as well as group leader Paolo Chiggiato, and the members of the Physics Beyond Colliders – Fixed Target working group and its group leader Massimiliano Ferro-Luzzi who made the unexampled opportunity to work on this research project for my thesis possible, and contributed to it with both guidance and support. I would like to especially thank Ivo Wevers, whose daily supervision, patience, insights, training, and practical help has been beyond invaluable and instrumental this past year.

I would also like to specifically acknowledge the help of and give many thanks to Martino Rimoldi for his help with the XPS measurements, as well as Stephan Pfeiffer and Alice Moros for their help in the XRD, FIB, and SEM measurements, Didier Glaude for his help in optical profilometry, Yorick Maxence Delaup for his help regarding the coating deposition, Jerome Gilles Chaure for his help with the endoscopy, and Rowan Cape Hill-James, Orlando Santos, and many others for their help in the laboratory activities.

Lastly, I want to say thank you to all my friends that supported me during these past years and were part of my life, as well as my family for all the support they provided me.

*Dávid Máté Parragh*

# Contents

<b>Preface</b>	<b>i</b>
<b>Abstract</b>	<b>iii</b>
<b>List of Figures and Tables</b>	<b>v</b>
<b>List of Abbreviations and Symbols</b>	<b>xi</b>
<b>1 Introduction</b>	<b>1</b>
<b>2 Literature Review</b>	<b>5</b>
2.1 Vacuum Fundamentals . . . . .	5
2.2 TiZrV Non-Evaporable Getter Coating . . . . .	9
2.3 Hydrogen-Getter Interactions and Embrittlement . . . . .	15
<b>3 Materials and Methods</b>	<b>21</b>
3.1 Sample Preparation . . . . .	21
3.2 High Pressure Experiment . . . . .	23
3.3 Low Pressure Experiment . . . . .	29
3.4 Reference Activation . . . . .	30
3.5 Materials Characterization Techniques . . . . .	31
3.6 Simulation Methods . . . . .	33
3.7 Overview of Sample Characterization Matrix . . . . .	35
<b>4 Results and Discussion</b>	<b>39</b>
4.1 As-deposited and Reference Activated Sample Characterization . . .	39
4.2 High Pressure Experiment . . . . .	44
4.3 Low Pressure Experiment . . . . .	70
<b>5 Conclusion</b>	<b>81</b>
<b>A Appendix</b>	<b>87</b>
A.1 Literature Review . . . . .	87
A.2 Materials and Methods . . . . .	88
A.3 Results and Discussions . . . . .	91
<b>Bibliography</b>	<b>103</b>

# Abstract

Non-evaporable getters (NEGs) are solid materials capable of chemisorbing gas molecules, as well as regaining their surface capacity after reaching complete surface coverage, by dissolving their native oxide layer during activation at elevated temperatures. Owing to their utility, NEG materials are widely used as chemical capture pumps in high vacuum applications, such as in the non-cryogenic parts of modern particle accelerators. The state-of-the-art NEG coating is a nanocrystalline/amorphous TiZrV alloy which provides an efficient and compact solution for distributed pumping in vacuum designs with long and narrow geometries when deposited on the inside of beam pipes and other vacuum surfaces. The sorption of  $H_2$  by the TiZrV coating, contrary to other getter gases, involves the dissociation of the  $H_2$  molecule on the getter surface followed by the monoatomic diffusion of hydrogen atoms into the bulk of the coating. While the  $H_2$  sorption properties of the TiZrV coating have previously been extensively studied below its saturation limit, its sorption behavior at higher hydrogen quantities where saturation, hydride formation, and the consequent embrittlement of the coating can occur previously has not been reported on.

Accordingly, the goal of this work was defined to study the sorption behavior of the state-of-the-art TiZrV NEG coating to gain a better understanding of its  $H_2$  saturation behavior and provide an estimate for its embrittlement limit, a parameter of high technical importance. In the experimental part of this work,  $H_2$  saturation experiments were conducted on TiZrV coated stainless steel pipes at two experimental conditions to study the room temperature sorption and saturation behavior of the coating at instantaneous injections of  $H_2$  at 1 hPa injection pressure throughout 6 cycles, as well as during the continuous injection of  $H_2$  at  $5 \times 10^{-7}$  hPa to simulate its saturation behavior at conditions similar to that of the Large Hadron Collider beauty (LHCb) experiment at the European Organization for Nuclear Research (CERN) during fixed target experiments.

The results of this work demonstrated that at the injected hydrogen quantities, the sticking coefficient and the  $H_2$  sorption rate of the TiZrV coating shows a clear dependence on the absorbed hydrogen content, both decreasing at increased hydrogen absorption. The  $H_2$  sorption limit was established as at minimum 0.4 H/TiZrV (mol/mol) at the 1 hPa injection condition, and as 0.026 H/TiZrV (mol/mol) at the  $5 \times 10^{-7}$  hPa continuous injection condition. Visual signs of embrittlement were not observed on the coating in the stainless steel pipes, proving the TiZrV alloy much more robust against hydrogen embrittlement than other getter

materials. While embrittlement was not observed on the coating on the stainless steel pipes, the residual hydrogen content was observed to impose a limit on the pumping capability of the coating, highlighting the importance of ensuring sufficiently high hydrogen release kinetics by the reactivation condition. Besides, by characterization of witness samples from the 1 hPa injection experimental condition it was determined that the repeated cycles of activation,  $H_2$  injection, and venting decrease the efficiency of the ability of the coating to achieve the metallic state of its surface during the activation, motivating that care has to be taken when assessing the sorption quantities of the TiZrV coating in critical applications.

# List of Figures and Tables

## List of Figures

1.1	Schematic representation of surface oxide, carbide, and nitride layer dissolution from the surface of the TiZrV alloy during activation . . . .	2
1.2	The accelerator complex at CERN showing the various parts of the complex together with their pressure requirements . . . . .	3
2.1	Simulated pressure profiles of a beam pipe demonstrating the effect of distributed pumping by the NEG coating . . . . .	10
2.2	Crystallinity map of alloys in the Ti-Zr-V system as a function of their elemental composition (at%) . . . . .	11
2.3	Schematic temperature profile of the bake-out and NEG activation process of TiZrV coated beam pipes in the Large Hadron Collider (LHC)	12
2.4	Pumping speed deterioration of H <sub>2</sub> , CO and N <sub>2</sub> of St 707 ribbon as a function of sorbed quantity of the same single gas . . . . .	14
2.5	Pumping speed deterioration of H <sub>2</sub> , CO and N <sub>2</sub> of TiZrV coating during progressive saturation of the surface with CO . . . . .	14
2.6	Pumping speed deterioration of H <sub>2</sub> , CO and N <sub>2</sub> of TiZrV coating during progressive saturation of the surface with N <sub>2</sub> . . . . .	15
2.7	Octahedral (O) and tetrahedral (T) interstitial sites (solid dots) in face-centered cubic (fcc), hexagonal close-packed (hcp), and body-centered cubic (bcc) crystal lattices . . . . .	16
2.8	Mechanisms and pathways proposed and observed for hydride formation of metals or metallic systems . . . . .	19
3.1	Intertwisted Ti, Zr, and V wire serving as the cathode for the TiZrV direct current magnetron sputtering shown as inserted into the test pipe	22
3.2	Top perspective view of the solenoid used in the TiZrV direct current magnetron sputtering deposition process . . . . .	22
3.3	Witness samples placed inside the test pipes at their entrance before the start of the experiments . . . . .	22
3.4	Test bench 1 used for the high pressure experiment with heating equipment and Al foil insulation installed . . . . .	25
3.5	Schematic of the test bench in fig. 3.4 used for the high pressure experiment	25

3.6	Pressure profile of one single high pressure experimental cycle with the different stages labeled . . . . .	28
3.7	Geometry of the test bench used for the low pressure experiments as recreated in Molflow+ with green lines tracking the path of simulated gas particles . . . . .	34
3.8	Transfer curve for the transmission ratio and the sticking coefficient obtained by Molflow+ simulations on the Test bench 2 geometry . . . .	35
3.9	Transfer curve for the capture probability and the sticking coefficient obtained by Molflow+ simulations on the Test bench 2 geometry . . . .	35
4.1	Focused ion beam (FIB) imaging of the cross-section of the as-deposited TiZrV coating used in the high pressure (a) and low pressure (b) experiment . . . . .	40
4.2	Top surface of the bare stainless steel substrate (a) and the as-deposited HP-0 sample (b) as imaged by scanning electron microscopy (SEM) . .	41
4.3	X-ray diffraction (XRD) pattern of the powdered TiZrV coating from an as-deposited HP-0 sample . . . . .	42
4.4	Reference XRD patterns of $\text{Ti}_{0.28}\text{Zr}_{0.28}\text{V}_{0.44}$ coatings after deposition (reference), after being subjected to 10 repeated activation-venting cycles at different temperatures (“cycled”), and after a 240 h anneal before venting and after deposition at different temperatures (“annealed”) . . .	42
4.5	Top SEM images of the high pressure (HP) sample before (a) and after (b), and the low pressure (LP) sample before (c) and after (d) the reference activation . . . . .	43
4.5	Top SEM images of the HP sample before (a) and after (b), and the LP sample before (c) and after (d) the reference activation (cont.) . . . . .	44
4.6	Calculated $\text{H}_2$ equilibrium pressure as a function of H / TiZrV hydrogen fraction in the TiZrV coating at 20 °C and 230 °C, with potential hydrogen fraction region of embrittlement indicated with a rectangle . .	45
4.7	Sticking coefficient evolution over the high pressure experimental cycles	47
4.8	The ultimate pressure evolution over the high pressure experimental cycles	48
4.9	Pressure evolution in static vacuum after the 1 hPa $\text{H}_2$ injections in cycle 1-3 (a) and 4-6 (b) . . . . .	49
4.10	Pressure evolution during the high pressure experiment activations . . .	50
4.11	Pressure evolution during the high pressure experiment activations with focus on the ramp up . . . . .	50
4.12	Pressure evolution during the high pressure experiment reactivations, with the 1 <sup>st</sup> activation pressure profile as well for reference . . . . .	52
4.13	Mass balance of the experimental cycles as calculated from the (re)activation pressure (a) and the injection curves (b) . . . . .	53
4.14	Perspective view of the TiZrV coating during the visual inspection (a) and the endoscopy (b) after the 6 <sup>th</sup> high pressure cycle . . . . .	54
4.15	Top SEM images of the witness samples from the high pressure experiments	55
4.15	Top SEM images of the witness samples from the high pressure experiments (cont.) . . . . .	56

4.16	SEM image of the top surface of the HP-3 sample, showing representative peel-off of the witness samples as a result of witness sample handling (bending and unbending) . . . . .	56
4.17	Evolution of the normalized O 1s peak area throughout the in-situ activations as measured with X-ray photoelectron spectroscopy (XPS) .	58
4.18	Evolution of the normalized C 1s peak area throughout the in-situ activations as measured with XPS . . . . .	59
4.19	XPS spectra of the C 1s peaks of the witness samples in as-received condition and after the in-situ activation . . . . .	60
4.20	Relative mole fraction of the alloying elements of the HP witness samples: bulk composition measured with X-ray fluorescence spectroscopy (XRF) (striped), and surface composition at as-received condition at room temperature, and after the in-situ activation measured with XPS (solid fill)	62
4.21	XPS spectra of the Ti 2p peaks of the witness samples in as-received condition and after the in-situ activation . . . . .	63
4.22	XPS spectra of the Zr 3d peaks of the witness samples in as-received condition and after the in-situ activation . . . . .	64
4.23	XPS spectra of the V 2p peaks of the witness samples in as-received condition and after the in-situ activation . . . . .	65
4.24	Secondary electron yield (SEY) of the witness samples from the high pressure experiment after the in-situ activation, with the SEY curve of the as-deposited sample in as-received condition included . . . . .	67
4.25	Reference secondary electron yield measurements of the TiZrV coating in its as-received state, and after up to 10 venting cycles . . . . .	67
4.26	Thermal desorption spectroscopy (TDS) spectra of H <sub>2</sub> (2 m/z) as a function of temperature normalized to unit mass of the TiZrV coating .	70
4.27	Evolution of the sticking coefficient for H <sub>2</sub> , N <sub>2</sub> and CO during the low pressure injection experiment . . . . .	72
4.28	Pressure evolution during the activation and the reactivation during the low pressure experiment . . . . .	73
4.29	Perspective view of the TiZrV coating during the endoscopy after the low pressure experiment . . . . .	74
4.30	SEM images of the as-deposited LP-0 sample (a) and the LP-1 witness sample after the low pressure experiment (b) . . . . .	75
4.31	Evolution of the normalized O 1s peak area throughout the in-situ activation as measured with XPS on the witness samples from the low pressure experiment . . . . .	76
4.32	Evolution of the normalized C 1s peak area throughout the in-situ activation as measured with XPS on the witness samples from the low pressure experiment . . . . .	76
4.33	XPS spectra of the C 1s peaks of the witness samples from the low pressure experiment in as-received condition and after the in-situ activation	77
4.34	XPS spectra of the Ti 2p peaks of the witness samples from the low pressure experiment in as-received condition and after the in-situ activation	78

4.35	XPS spectra of the Zr 3d peaks of the witness samples from the low pressure experiment in as-received condition and after the in-situ activation	78
4.36	XPS spectra of the V 2p peaks of the witness samples from the low pressure experiment in as-received condition and after the in-situ activation	79
4.37	SEY of the witness samples in as-received condition of the as-deposited LP-0 sample, and after the in-situ activation of the LP-0, LP-0A, and LP-1 samples from the low pressure experiment . . . . .	79
A.1	The temperature profile during the bake-out of the test bench followed by the activation of the coated test pipe . . . . .	88
A.2	Pressure profile during a typical transmission method measurement where H <sub>2</sub> is injected into the test dome in steps of increasing flow rates	89
A.3	Pressure profile during the high pressure (1 hPa) H <sub>2</sub> injections showing the ramp up to the target pressure (at the 90 s mark in the plot) after which the variable leak valve is closed, the full-range gauge (FRG) is turned off, and the TiZrV coating is allowed to pump the injected H <sub>2</sub> in static vacuum . . . . .	90
A.4	FIB micrograph of the cross-section of an as-deposited LP-0 sample displaying a groove at the right end of the cross-section extending through the thickness of the TiZrV coating . . . . .	91
A.5	Simulated ternary phase diagram of the Ti-Zr-V material system at 293.15 K and 1 atm pressure . . . . .	92
A.6	Simulated ternary phase diagram of the Ti-Zr-V material system at 393.15 K and 1 atm pressure . . . . .	93
A.7	Normalized mass-to-charge spectra showing the composition of vacuum throughout the high pressure experimental cycles measured 24 h after cooling down to room temperature after the activation in each cycle . .	94
A.8	X-ray photoelectron spectroscopy spectra of the O 1s peaks of the witness samples in as-received condition and after the in-situ activation	97
A.9	Diffusion length after 2 h for H, C, O, and N in Ti (a), Zr (b), and V (c) as a function of heating temperature, with extrapolated data in dashed lines	99
A.9	Diffusion length after 2 h for H, C, O, and N in Ti (a), Zr (b), and V (c) as a function of heating temperature, with extrapolated data in dashed lines (cont.) . . . . .	100
A.10	Electron penetration depth as a function of incident electron energy from simulations with Casino software on a multilayer of 1000 nm Ti <sub>31</sub> Zr <sub>18</sub> V <sub>52</sub> on top of a 304L stainless steel substrate . . . . .	100

## List of Tables

2.1	Degrees of vacuum and their corresponding pressure range with examples for their different applications and pumps used to attain them . . . . .	6
2.2	Number density ( $\rho_N$ ), mean free path ( $\lambda$ ) and impingement rate ( $J$ ) of a single gas at $T = 295$ K at different degrees of vacuum . . . . .	8

2.3	Different non-evaporable getter materials with their respective minimum activation temperature . . . . .	9
2.4	Tetrahedral ( $r_{th.}$ ) and octahedral ( $r_{oh.}$ ) site radius of $\alpha$ and $\beta$ phases of Ti and Zr, together with their respective diffusion activation energy ( $E_A$ ), $D_0$ maximal diffusion coefficient, and $\sqrt{D\tau}$ diffusion transport distance for hydrogen . . . . .	17
2.5	Crystal structure of Ti, Zr, and V in their stable phases at standard temperature and pressure together with the observed structure of their hydrides, with the formation enthalpy ( $\Delta H$ ) and formation entropy ( $\Delta S/k$ ) of the stoichiometric hydride phases included. The temperature ranges pertaining to the thermodynamic data are included as well . . .	18
3.1	Deposition parameters of TiZrV coating of the two 304L stainless steel pipes serving as the test pipes for the low pressure (NEG1) and the high pressure (NEG2) $H_2$ saturation experiments . . . . .	23
3.2	Witness sample characterization matrix for the high pressure (HP) and the low pressure (LP) experiments, with “-0” referring to as-deposited samples, “-0A” referring to activated reference samples, else witness samples subjected to the ascribed number of cycles . . . . .	37
4.1	TiZrV coating thickness and composition as determined from witness samples for the two test pipes by XRF measurement . . . . .	40
4.2	Root mean square ( $R_q$ ) surface roughness of the substrate, the as-deposited (-0), and the reference activated (-0A) samples as measured by optical profilometry at two magnifications . . . . .	44
4.3	Pressure maxima ( $p_{max}$ ) and plateau pressures ( $p_{plateau}$ ) of the activations and reactivations in the high pressure experiments . . . . .	52
4.4	Relative surface oxygen content decrease as a result of activation, relative surface carbon content decrease as a result of activation, and carbon-to-carbide conversion ratio . . . . .	61
4.5	Maximum SEY values of the witness samples from the high pressure experiment . . . . .	68
4.6	Overview of the sticking coefficients measured before the low pressure injection, after the low pressure injection, and after reactivation over the course of the low pressure experiment . . . . .	71
4.7	Relative surface oxygen content decrease as a result of activation, relative surface carbon content decrease as a result of activation, and carbon-to-carbide conversion ratio of the witness samples from the low pressure experiment . . . . .	77
A.1	Solubility limit of H, O, N, and C in atomic % in pure Ti, Zr, and V . .	87
A.2	Heat of dissolution of oxygen ( $\Delta H_{ss}$ ) in pure metals compared to the heat of formation of the stable oxide ( $\Delta H_{ox}$ ) containing the lowest number of oxygen atoms per atom of metal . . . . .	87

## LIST OF FIGURES AND TABLES

---

A.3	Calibration constants of the different ionization gauges used at the test benches of the vacuum experiments. Dividing the read out N <sub>2</sub> equivalent pressures by the calibration constants yields the H <sub>2</sub> or CO equivalent pressures . . . . .	88
A.4	Correction factors for the H <sub>2</sub> equivalent residual pressure reading of the ionizing gauges obtained from the transmission method measurements of the calibration run on Test bench 1 and Test bench 2 using the reference uncoated test pipe . . . . .	90
A.5	Elemental surface composition in mole fractions of the witness samples from the high pressure experiment as measured with XPS in as-received condition at room temperature (20 °C), and after 1 h in-situ activations at temperatures of 160 °C, 200 °C, and 250 °C . . . . .	95
A.6	Reference spectral lines for the analysis of the X-ray photoelectron spectroscopy measurements . . . . .	96
A.7	Elemental surface composition in mole fractions of the witness samples from the low pressure experiment as measured with XPS in as-received condition at room temperature (20 °C), and after 1 h in-situ activations at temperatures of 160 °C, 200 °C, and 250 °C . . . . .	101

# List of Abbreviations and Symbols

## Abbreviations

ACG	active capacitance gauge
bcc	body-centered cubic
CERN	the European Organization for Nuclear Research
DC	direct current
ECG	emitting cathode gauge
EDX	energy dispersive X-ray spectroscopy
fcc	face-centered cubic
FIB	focused ion beam
FRG	full-range gauge
hcp	hexagonal close-packed
HP	high pressure
LEP	Large Electron-Positron Collider
LHC	Large Hadron Collider
LHCb	Large Hadron Collider beauty
LP	low pressure
NEG	non-evaporable getter
RGA	residual gas analyzer
SEM	scanning electron microscopy
SEY	secondary electron yield
SMOG	System for Measuring Overlap with Gas
SMOG2	System for Measuring Overlap with Gas 2
TDS	thermal desorption spectroscopy
TMP	turbomolecular pump
WDX	wavelength dispersive X-ray spectroscopy
XPS	X-ray photoelectron spectroscopy
XRD	X-ray diffraction
XRF	X-ray fluorescence spectroscopy

## Symbols

$A$	area	(cm <sup>2</sup> )
$C$	conductance	(dm <sup>3</sup> /s)
$CP$	capture probability	(-)
$c_{av}$	mean velocity	(m/s)
$d$	diameter	(m)
$I$	current	(mA)
$J$	impingement rate	(1/cm <sup>2</sup> /s)
$Kn$	Knudsen number	(-)
$M$	molar mass	(g/mol)
$N$	number of particles	(-)
$n$	number of particles	(mol)
$p$	pressure	(hPa)
$Q$	gas flow rate	(hPa dm <sup>3</sup> /s)
$S$	pumping speed	(dm <sup>3</sup> /s)
$s$	gauge calibration constant	(1/hPa)
$T$	temperature	(K)
$V$	volume	(dm <sup>3</sup> )
$wt$	mass fraction	(g/g)
$x$	molar fraction	(mol/mol)
$\alpha$	sticking coefficient	(-)
$\Delta H$	reaction enthalpy	(J)
$\lambda$	mean free path	(m)
$\rho$	density	(g/cm <sup>3</sup> )
$\rho_N$	number density	(1/m <sup>3</sup> )

## Constants

$k$	Boltzmann constant	= 1.3806 J/K
$R$	ideal gas constant	= 8.3145 J/mol/K

# Chapter 1

## Introduction

Vacuum requirements in modern particle accelerators necessitate pumping solutions that ensure stable and low pressure levels along the length of the beam pipes, in combination with surfaces that exhibit limited outgassing; even under radiation, or particle bombardment, associated with the operation of the accelerator [1]. The technology of depositing TiZrV<sup>1</sup> non-evaporable getter (NEG) coatings on the inside of the beam pipes, developed at the European Organization for Nuclear Research (CERN) between 1995–2002 meets both of these aspects [2, 4]; as a getter material, after a heating process under vacuum called activation, it achieves low and stable pressure levels by chemisorbing and/or absorbing residual gas molecules from the vacuum, characterized by exceptional pumping rates and pumping capacities [5, 6]. On the other hand, TiZrV acts as a barrier between the vacuum and its substrate, and exhibits low photon-induced, ion-induced, and electron-induced outgassing itself, making it an ideal coating inside the accelerator [2, 7, 8]. Accordingly, the TiZrV getter coating is increasingly used in particle accelerators and synchrotron radiation facilities around the world [9–11], including 6 km of the room temperature long straight sections (LSSs) of the Large Hadron Collider (LHC) where it aids reaching pressures below  $1 \times 10^{-12}$  hPa since its commissioning in 2008 [12].

Non-evaporable getters such as the TiZrV coating are chemical capture pumps; they provide pumping until their available surface sites are consumed, and are called non-evaporable as they are characterized by the ability to regenerate the available surface sites by a heating process during which sorbed atoms diffuse into the bulk of the layer (see fig. 1.1) [13]. Accordingly, the main concern during the operation of a NEG coating is first and foremost monitoring and predicting the saturation of its surface where the free metallic sites chemically bind active gases such as CO, CO<sub>2</sub>, N<sub>2</sub>, O<sub>2</sub>, and H<sub>2</sub>O [14, 15]. As the surface sites are consumed, the pumping speed of the getter deteriorates, which, at a critical limit requires the reactivation of the getter [16]. The oxides, carbides, and nitrides that formed on the surface of the

---

<sup>1</sup>The stoichiometry of the state-of-the-art TiZrV alloy is cited as Ti<sub>0.3</sub>Zr<sub>0.3</sub>V<sub>0.4</sub> as nominally deposited from intertwisted elemental cathode wires [2], however, as the Ti-Zr-V system is observed to form nanocrystalline or amorphous microstructure over a wide range of compositions which yield functionally identical getter coatings [3], the designation TiZrV is used in this work to refer to Ti-Zr-V alloys with nanocrystalline microstructures with a nominal composition of Ti<sub>0.3</sub>Zr<sub>0.3</sub>V<sub>0.4</sub>.

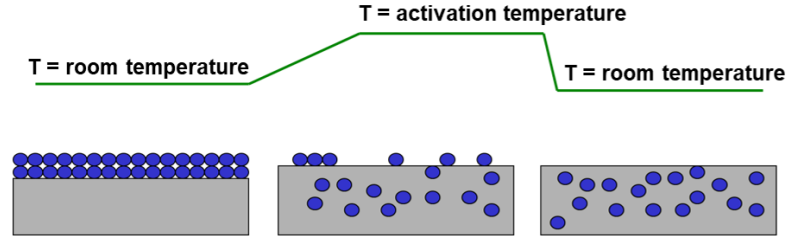


**Figure 1.1:** Schematic representation of surface oxide, carbide, and nitride layer dissolution from the surface of the TiZrV alloy during activation. Adapted from [17]

TiZrV alloy diffuse and dissolve into its bulk during activation [4], which means that their solubility limit defines the lifetime of the getter material, translated into the number of permissible saturation/venting-activation cycles. While the value of the regainable pumping speed decreases during repeated saturation/venting-activation cycles, with appropriately chosen activation temperatures, up to 30 cycles have been observed to be possible with only a pumping speed reduction of a factor of two of the TiZrV NEG layer [2].

H<sub>2</sub>, which is the dominant gas in the static vacuum of baked vacuum systems, contrary to other gettered gases, is pumped by dissociating and monoatomically diffusing into the bulk of the TiZrV alloy in a thermally reversible process [4, 18, 19]. While the capacity of TiZrV for H<sub>2</sub> sorption is much larger than that of other gases at room temperature, and is generally compatible with typical operation conditions of a particle accelerator, in the case of higher H<sub>2</sub> loads, the concern of embrittlement emerges. The empirically obtained embrittlement limit indicates the absorbed H<sub>2</sub> quantity above which hydrides start forming in the alloy [20]. Besides the loss of pumping speed, the formation of hydrides create mechanical stresses within the layer, which, in extreme cases, can even cause flaking, or peel-off of the NEG coating [21]. Therefore, the embrittlement of the getter layer, by losing its functionality and mechanical integrity, endangers the safe operation of the particle accelerator.

The Large Hadron Collider beauty (LHCb) experiment at CERN consists of a single arm forward spectrometer detector located at the 8<sup>th</sup> interaction point of the LHC (fig. 1.2) and is designed primarily to study matter-antimatter asymmetry by studying beauty-quark decays from proton-proton collision [22]. It is also equipped with an internal gas target called System for Measuring Overlap with Gas (SMOG), which offers the possibility of injecting noble gases into the beam pipe at a nominal pressure of  $2 \times 10^{-7}$  hPa for proton-gas collision experiments. The SMOG2 upgrade, completed in the beginning of 2022 took place to make injections of a larger variety of gases –including H<sub>2</sub>– and at even higher possible gas densities possible [22–25]. As several parts of the LHCb machine are coated with TiZrV NEG and rely on its proper functioning, during the planned H<sub>2</sub> injections, the concern of H<sub>2</sub> induced embrittlement of the getter coating emerges. In the context of this upgrade, the goal

of this work is to study the sorption behavior and the potential degradation of the TiZrV getter coating in the presence of H<sub>2</sub> gas which was previously not studied in literature.

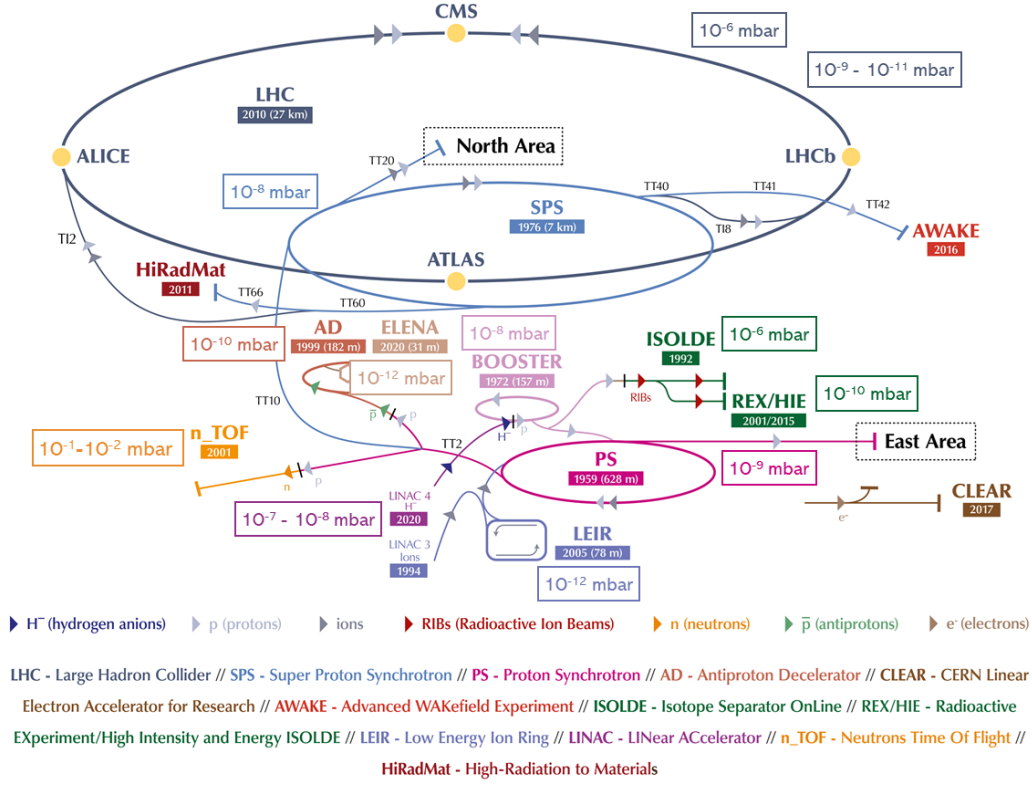


**Figure 1.2:** The accelerator complex at CERN showing the various parts of the complex together with their pressure requirements [26]

In order to study the H<sub>2</sub> sorption and the potential, consequent degradation of the TiZrV non-evaporable getter coating, two experimental conditions were defined at two injection pressures; H<sub>2</sub> saturation experiments were conducted on TiZrV coated stainless steel beam pipes at a high injection pressure (1 hPa) and a low injection pressure ( $5 \times 10^{-7}$  hPa) and the functionality and materials properties of the coating were characterized as a function of injected H<sub>2</sub> quantity. In the high pressure experimental condition, H<sub>2</sub> was injected instantaneously at 1 hPa in 6 repeated cycles which served the purpose of contributing to determining the embrittlement limit of the TiZrV coating, as well as testing the effect of repeated injections and venting cycles on the vacuum and materials properties of the coating. In the low pressure experiment, H<sub>2</sub> was injected over an extended period at  $5 \times 10^{-7}$  hPa to simulate the saturation condition at the LHCb experiment and study the evolution of the pumping capability of the coating as a function of sorbed hydrogen quantity in ultra-high vacuum. The goal of the experiments were defined as obtaining information on the embrittlement limit of the TiZrV coating, as well as studying how the H<sub>2</sub> sorption

affects the pumping functionality, as well as the materials properties of the coating.

The layout of the thesis work is as described in the following. Firstly, chapter 2 presents the necessary background information and literature review for the context of this work. The details of the experiments realized as part of this work are then discussed in chapter 3, and the obtained results are presented and analyzed in chapter 4. Finally, the achievements of the thesis work are summarized in chapter 5.

## Chapter 2

# Literature Review

In this chapter, the necessary background information and literature review on the fundamental vacuum calculations in section 2.1, the development and description of the TiZrV non-evaporable getter (NEG) coating in section 2.2, and the sorption, hydride formation, and embrittlement phenomena concerning hydrogen and the relevant metallic system in section 2.3 are discussed, providing a theoretical framework and a scientific context for the experimental part of this work, the details of which are described in the following chapter.

### 2.1 Vacuum Fundamentals

Vacuum refers to a volume of space in which the gas density is lower than that of a gas at the same temperature at atmospheric pressure. Vacuum is commonly divided into degrees, distinguished by different pumping solutions, applications and gas flow properties as shown in table 2.1 [6, 13, 20, 27].

A note on the used units has to be made, since deviation from SI units is not uncommon practice in vacuum technology due to historical and practical reasons. Pressure, besides Pa, is often expressed in bar or mbar, Torr, and atm, with standard atmospheric pressure being 1 atm, 101325 Pa, 1013.25 mbar, or 760 Torr. As for volume, mostly due to the practical volumes used in laboratory settings, L is often used instead of m<sup>3</sup>, with 1 m<sup>3</sup> = 1000 L [13]. As in the relevant publications on TiZrV NEG coating pressure and volume is most often expressed in mbar and L, respectively, this work uses the value-equivalent units of hPa for pressure and dm<sup>3</sup> for volume.

#### 2.1.1 Ideal Gas Law, Kinetic Theory of Gases and Gas Flow Regimes

Vacuum refers to a volume in which gas is rarefied, and the level of rarity can be quantified by the number density ( $\rho_N$ ) defined as

$$\rho_N = \frac{N}{V} \tag{1}$$

## 2. LITERATURE REVIEW

Vacuum degree	Pressure (hPa)	Application	Pump type
Low (or rough) vacuum	$10^3$ – $1$	Degassing, drying, filtration	Oil-sealed rotary pumps
Medium vacuum	$1$ – $10^{-3}$	Distillation Chemical Vapor Deposition	Dry pumps Liquid ring pumps
High vacuum	$10^{-3}$ – $10^{-9}$	Physical Vapour Deposition	Diffusion pumps Turbomolecular pumps
Ultra-high vacuum	$10^{-9}$ – $10^{-12}$	Surface spectroscopies	Cryopumps Turbomolecular pumps
Extreme high vacuum	$< 10^{-12}$	Fusion research Particle accelerators Synchrotron radiation sources	Diffusion pumps Sputter ion pumps Getter pumps

**Table 2.1:** Degrees of vacuum and their corresponding pressure range with examples for their different applications and pumps used to attain them [27, 28]

referring to the ratio of  $N$  number of particles occupying  $V$  volume [20]. The relationship between the quantity of gas and its state variables is established by the ideal gas law as in

$$p = \rho_N kT \quad (2)$$

or

$$pV = nRT \quad (3)$$

where  $p$  denotes pressure,  $k$  the Boltzmann constant (1.3806 J/K),  $T$  temperature,  $n$  number of particles in mol, and  $R$  the ideal gas constant (8.3145 J/mol/K) [13, 27]. The ideal gas law can be applied to virtually all situations encountered in vacuum systems [13]. From eq. (2) it is clear that under isothermal conditions, the value of pressure directly indicates the rarity of gas in vacuum.

In the kinetic theory of gases, gas particles are modeled by perfectly elastic hard spheres with radius  $r$  that move and collide according to the laws of classical mechanics in a constant, rapid and chaotic fashion, and are separated by distances, and occupy volumes comparably larger than their diameter [13]. As derived in this framework, the velocities of the particles of such an ideal gas follow a Maxwell-Boltzmann distribution with a mean velocity of

$$c_{av} = \sqrt{\frac{8RT}{\pi M}} \quad (4)$$

where  $M$  denotes the molar mass of the gas, showing that gases consisting of heavier particles have a lower mean velocity at a given temperature [27]. The mean normal component of the mean velocity of a gas obtained as  $c_{av}/4$  is a highly useful quantity as it numerically equals the maximum area related pumping speed of a pump [27]. Accordingly, the impingement rate of a gas  $J$  is defined as

$$J = \frac{\rho_n c_{av}}{4} \quad (5)$$

which gives the number of gas particles impinging on a unit area of a surface per s [13].

Another important metric obtained from the kinetic theory of gases is the mean free path ( $\lambda$ ) referring to the average distance that a gas particle travels between two successive collisions, and is obtained for a single gas from

$$\lambda = \frac{1}{\sqrt{2}\pi d^2 \rho_N} \quad (6)$$

where  $d$  denotes the diameter of the idealized, spherical gas particle [20].

From eq. (6) it is clear that the more rarefied the vacuum, characterized by a lower number density, the less frequently the gas particles collide with each other. Accordingly, in high enough vacuum, the collisions between gas particles can be neglected and the behavior of the gas is dominated by particle-wall collisions, resulting in a substantially different behavior than at atmospheric pressure. The Knudsen number ( $Kn$ ) is defined as the ratio of the mean free path of the gas and the characteristic dimension ( $d_c$ ) of the vacuum duct as in

$$Kn = \frac{\lambda}{d_c} \quad (7)$$

and is used to delineate the different flow regimes of a gas in a duct [27]. In the continuum flow regime ( $Kn < 0.01$ ) the motion of the gas particles is defined by the collisions between them resulting in viscous flow, while in the molecular flow regime ( $Kn > 5$ ) the mean free path of the gas particles are larger than the characteristic dimension of the duct, meaning that the particles mostly move in zigzag motion in straight lines between the walls [27].

Table 2.2 lists different number density, mean free path, and impingement rate values of a gas, from which it is clear that in ultra-high and extreme high vacuum the molecular flow regime is applicable to practical vacuum systems [13].

### 2.1.2 Gas Flow Rate and Getter Performance Quantification

The gas flow rate ( $Q$ ), which can refer to various mass transfer processes of a gas including leak, outgassing, or flow through a defined orifice, is most typically given as  $p\dot{V}$  (hPa dm<sup>3</sup>/s) throughput, which, by specifying the temperature of the gas, is equivalent with the flow rate of number of particles in the gas as based on eq. (3) [6].

## 2. LITERATURE REVIEW

$p$ (hPa)	$\rho_N$ (1/m <sup>3</sup> )	$\lambda$	$J$ (1/cm <sup>2</sup> /s)
$1 \times 10^3$	$2.5 \times 10^{25}$	64 nm	$2.9 \times 10^{23}$
1	$2.5 \times 10^{22}$	64 $\mu$ m	$2.9 \times 10^{20}$
$1 \times 10^{-3}$	$2.5 \times 10^{19}$	64 mm	$2.9 \times 10^{17}$
$1 \times 10^{-6}$	$2.5 \times 10^{16}$	64 m	$2.9 \times 10^{14}$
$1 \times 10^{-10}$	$2.5 \times 10^{12}$	640 km	$2.9 \times 10^{10}$

**Table 2.2:** Number density ( $\rho_N$ ), mean free path ( $\lambda$ ) and impingement rate ( $J$ ) of a single gas at  $T = 295$  K at different degrees of vacuum [13]

The pumping speed ( $S$ ) of a pump is defined as a volumetric flow rate  $\dot{V}$  (dm<sup>3</sup>/s), and assuming continuity in the vacuum system, in steady state, the gas flow rate can be calculated from

$$Q = S \cdot p \quad (8)$$

for a system equipped with a pump with pumping speed  $S$  [6].

While the interpretation of the dimension of pumping speed for positive-displacement pumps is straight-forward as they operate by removing fluid quantities in constant volume per unit time, pumping speed is equally used to describe the rate of evacuation provided by capture pumps, where, however, the removed volume is thought of as an abstract volume [6, 13]. A more intuitive quantity to describe the pumping capability of capture pumps such as non-evaporable getters is the sticking coefficient. The sticking coefficient  $\alpha$  of a getter pump shows the probability with which an impinging gas particle will be sorbed on its surface and therefore takes up values between 0–1 [6]. The relationship between the sticking coefficient and the pumping speed of a pump is obtained as

$$S = \alpha C \quad (9)$$

where  $C$  denotes conductance, with conductance being the inverse of the resistance of a pipe or an orifice to gas flow [6]. The sticking coefficient quantifies the pumping quality of the getter pump, and it is not only dependent on the material of the getter, but also on its roughness and surface coverage, meaning its level of saturation, as well as the type of gas sorbed [2, 29].

The conductance of an orifice or aperture, such as an entrance of a pipe, with area  $A$  for a given gas is obtained as

$$C = \sqrt{\frac{RT}{2\pi M_{gas}}} A = 11.8 A \sqrt{\frac{M_{N_2}}{M_{gas}}} \quad (10)$$

in the molecular flow regime [6], as commonly written with the constant 11.8 obtained from substituting  $M_{N_2}$  at 293.15 K [13]. Conductance has the same dimensions as pumping speed (dm<sup>3</sup>/s), and indeed equals the maximum pumping speed attainable through the given aperture or pipe.

## 2.2 TiZrV Non-Evaporable Getter Coating

Getters are solid materials that are able to chemically bind gas molecules to their surface, which is why they are categorized as chemical pumps. Non-evaporable getters are distinguished by the ability to regain their pumping speed during an in-situ heating process under vacuum called activation, which, by dissolving the gettered species from the surface, produces a clean metallic surface with regained pumping speed [4]. NEG pumps have multiple advantages over other types of pumps that are commonly used at room temperature to achieve ultra-high and extreme-high vacuum (see table 2.1). In contrast to turbomolecular pumps (TMPs), they provide vibration-free pumping without continuous power consumption [20]. Compared to evaporable getter pumps, such as sputter-ion pumps or Ti sublimation pumps, the use of NEG pumps avoids material deposition within the vacuum system [16, 20]. NEG coatings, a subset of NEG pumps, offer simpler vacuum vessel design and provide distributed pumping which is especially important in systems with limited available space and using narrow vacuum pipes, which is the case for modern particle accelerators and synchrotron radiation facilities [7, 16, 30, 31].

NEG pumps can be made as strips, wafer modules, cartridges, and coatings [13] and are composed of group 4 transition metal elements as they have high oxygen solubility, which are often alloyed with group 5 transition metal elements to enhance the oxygen diffusivity of the getter [4, 13]. First developed by SAES Getters in 1961 [6], their two most well-known NEG pumps are made of  $\text{Zr}_{0.57}\text{V}_{0.36}\text{Fe}_{0.7}$  (with brand name St 707) and  $\text{Zr}_{0.61}\text{Al}_{0.39}$  (St 101), in atomic percent [13]. These, and two other NEG materials developed at the European Organization for Nuclear Research (CERN) are shown in Table 2.3 together with their activation temperature.

Getter material	Activation temperature for 24 h (°C)
$\text{Zr}_{0.61}\text{Al}_{0.39}$ (St 101)	600
$\text{Zr}_{0.57}\text{V}_{0.36}\text{Fe}_{0.7}$ (St 707)	350
$\text{Ti}_{0.5}\text{Zr}_{0.5}$	250
$\text{Ti}_{0.3}\text{Zr}_{0.3}\text{V}_{0.4}$	180

**Table 2.3:** Different non-evaporable getter materials with their respective minimum activation temperature [4, 32]

### 2.2.1 Development of TiZrV Coating

As the length of the particle accelerator rings increased together with the reduction of their beam pipe cross-section in order to increase their attainable beam intensity, providing vacuum solely by frequently spaced pumps, commonplace before the 1970s, has become increasingly impractical [32]. In the Large Electron-Positron Collider (LEP) –the predecessor of the Large Hadron Collider (LHC)–, which was operational between 1989–2000, an ante-chamber beam pipe design was implemented, where St 101 NEG strips placed in the ante-chamber connected to the beam line provided

## 2. LITERATURE REVIEW

vacuum together with frequently spaced sputter-ion pumps [16, 32]. While this achieved a more uniform pressure and more effective pumping, while also reducing the required pump dimensions, the pressure in this system was still limited by the outgassing of the surfaces in the vacuum system, namely, from the beam line [32]. An even more compact beam pipe design was required for the LHC envisioned to be achieved by coating the inside of the beam pipe itself with a getter material, converting the beam pipe from a source of outgassing into an effective, distributed pumping solution, as demonstrated in fig. 2.1. This exact solution, technology, and getter material was developed and researched between 1995–2002 at CERN.

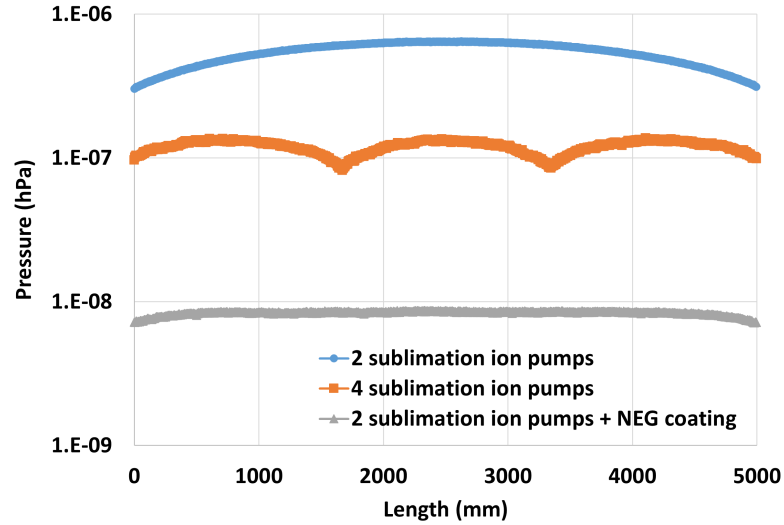


**Figure 2.1:** Simulated pressure profiles along a 5000 mm long and 50 mm diameter beam pipe with  $1 \times 10^{-9}$  hPadm<sup>3</sup>/cm<sup>2</sup>/s outgassing rate with 2 sublimation ion pumps ( $5 \times 10^{-2}$  sticking coefficient) at its extremities in blue, 4 sublimation ion pumps ( $5 \times 10^{-2}$  sticking coefficient) distributed along the length of the pipe in orange, and a non-evaporable getter coated beam pipe ( $1 \times 10^{-2}$  sticking coefficient) with 2 sublimation ion pumps at its extremities ( $5 \times 10^{-2}$  sticking coefficient) in grey

The main criteria for the development of the NEG coating was, besides excellent pumping properties, a low secondary electron yield (SEY) in order to avoid electron multipacting during accelerator operation [8], and sufficiently low activation temperature that is compatible with the maximum allowable temperatures for the materials in the vacuum system of the LHC, namely 200 °C for Al alloys and Be, 250 °C for Cu alloys, and 400 °C for stainless steel [2, 29, 33]. Direct current (DC) magnetron sputtering was used to deposit coatings of group 4 elements (Ti, Hf, Zr) and their binary alloys, as they have a sufficiently high solubility limit for oxygen (>10 %), and the lowest activation temperature of 300 °C was achieved with Ti<sub>0.5</sub>Zr<sub>0.5</sub> [9, 32, 34]. With the addition of V to enhance oxygen diffusivity of the getter, an even lower activation temperature of 180–200 °C was achieved by the ternary alloy of Ti, Zr, and V [2, 4, 32]. The adequate microstructure for the low activation temperature was

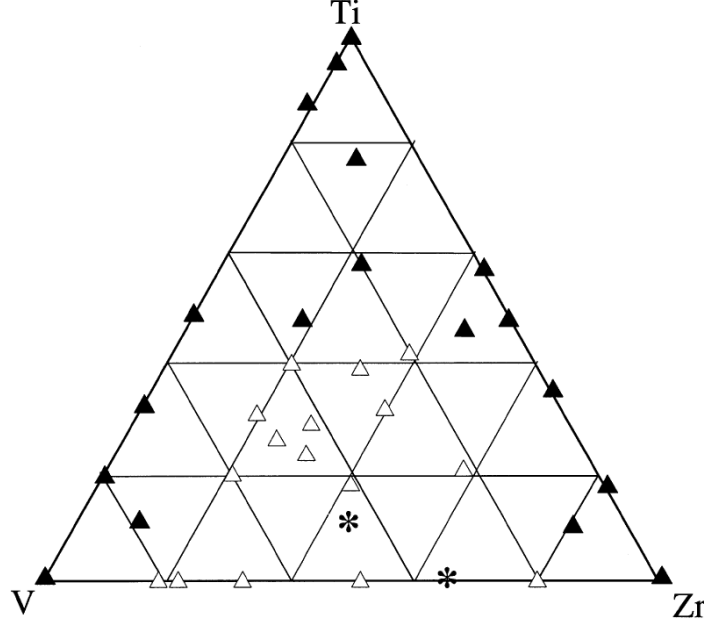


**Figure 2.2:** Crystallinity map of alloys in the Ti-Zr-V system as a function of their elemental composition (at%) from the study of Prodromides et al. [3]. Full triangles refer to polycrystalline microstructure ( $>100$  nm grain size), empty triangles refer to nanocrystalline microstructure (3–5 nm grain size), and stars refer to samples with no observed crystallinity

found to be either amorphous or nanocrystalline which was found to be achievable in a wide composition range (see fig. 2.2) [4]. A DC magnetron sputtering solution in a custom built solenoid was then adapted for deposition on the inside of beam pipes [2], in which elemental, intertwined cathode wires of Ti, Zr, and V were used to deposit a  $1\text{ }\mu\text{m}$  thick nanocrystalline TiZrV alloy coating with a nominal composition of  $\text{Ti}_{30}\text{Zr}_{30}\text{V}_{40}$ , which was found to meet all the design criteria and is considered the state-of-the-art NEG coating used in modern particle accelerators. This NEG coating was first used in the European Synchrotron Radiation Facility in 2000, followed by the Italian Synchrotron Light source Elettra in 2002, and most importantly for the context of this work, it is also used as an inner coating of 6 km of the beam pipes in the LHC which is operational since 2008 [2, 7, 32].

### 2.2.2 Operation Principle of Pumping Behavior

**Activation** When a NEG material is exposed to air, even if only for a short period of time, its surface becomes saturated by oxide, carbide and nitride formation, which blocks its pumping ability [4, 13]. Therefore, when installing a NEG pump into a vacuum system, be it a cartridge or a coating, it is required to be activated for it to become functional. The activation is carried out under vacuum and typically after

the bake-out of the rest of the vacuum system, as it is shown in the bake-out and activation temperature profile in fig. 2.3 that is used for NEG coated beam pipes in the LHC [12]. The bake-out is a heating process which accelerates the outgassing –primarily of  $\text{H}_2\text{O}$ – from the surfaces of the vacuum system, so that low pressure levels are achieved in a shorter time by the auxiliary pumps, as it would take considerably longer if only pumped at room temperature [35]. During the bake-out, the NEG pump is kept at an elevated temperature but below the activation temperature while the stainless steel parts are baked out at  $250^\circ\text{C}$  [12]. Although  $180^\circ\text{C}$  was found to be a sufficiently high temperature for the TiZrV coating to be fully activated in 24 h [29], a higher temperature of  $230^\circ\text{C}$  is used in the LHC in order to ensure complete activation, and a more homogeneous and sufficient dissolution of oxygen and carbon into the thickness of the getter layer [2, 12, 33].

As highlighted by the solubility limit of oxygen in pure Ti, Zr, and V metals in table A.1, as well as by a comparison of the energy of oxygen dissolution with the energy of oxide formation by the respective metals in table A.2 from the work of Prodromides [4], it has been shown that oxygen is thermodynamically favored to be dissolved in Ti and Zr at all temperatures up to its solubility limit is reached, and the dissolution is hindered by the kinetic limitations of oxygen diffusion, which is the reason behind the activation during which, at an elevated temperature, the oxygen diffusion rate is increased, allowing for oxygen dissolution.

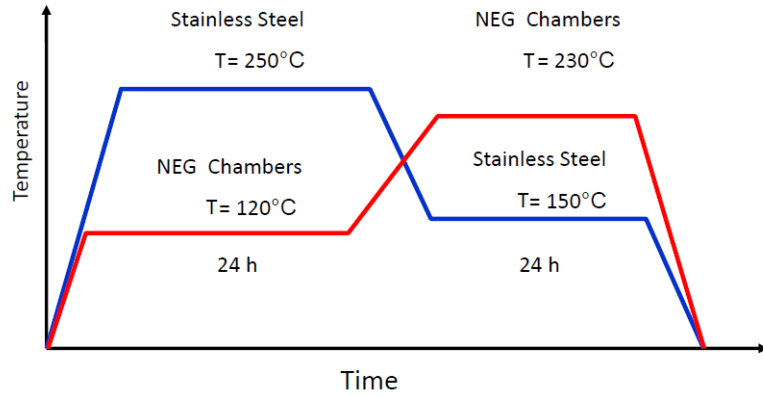


**Figure 2.3:** Schematic temperature profile of the bake-out and NEG activation process of TiZrV coated beam pipes in the LHC. Adapted from [12]

As  $\text{H}_2$  is pumped by dissociating on the TiZrV surface and monoatomically diffusing into its bulk in a thermally reversible process, the hydrogen content from the getter does accordingly outgas during activation, contrary to other gettered species, and can be pumped away by an auxiliary pump [16]. The relationship between the concentration of monoatomic hydrogen in the getter material ( $c$ ), the temperature ( $T$ ), and the dissociation pressure of hydrogen ( $p_{\text{H}_2}$ ) is given by Sievert's law, in which

$$p_{\text{H}_2} = a \cdot c^2 \cdot e^{\frac{\Delta H}{kT}} \quad (11)$$

where  $a$  and  $\Delta H$  are the material dependent entropic contribution of the  $H_2$  dissociation reaction and the reaction enthalpy, respectively [4]. Accordingly, during activation, by increasing the temperature, the hydrogen content of the getter material can be reduced by outgassing it and pumping it away.

**Sorption** After activation the NEG coating obtains a clean metallic surface. Different gases are gettered differently by the NEG coating and are distinguished accordingly; active gases are either chemisorbed ( $CO$ ,  $CO_2$ ,  $N_2$ ,  $O_2$ ), or absorbed ( $H_2$  and its isotopes), and  $H_2O$  dissociates on the surface and its constituents are sorbed separately. Hydrocarbons, including  $CH_4$  may be sorbed after cracking at elevated temperatures, but are not pumped at room temperature, and noble gases are inert and not pumped by NEG pumps [14]. TiZrV coating deposited on stainless steel at  $100^\circ C$  has a reported  $8 \times 10^{-3}$  maximum sticking coefficient for  $H_2$ , 0.7 for  $CO$  and  $1.5 \times 10^{-2}$  for  $N_2$ , the main gases used to benchmark getter pumping [2]. As  $CO$  and  $N_2$  is pumped by the getter surface, their surface capacity is reported as well as  $8 \times 10^{14}$  molecules  $cm^{-2}$  and  $1.5 \times 10^{14}$  molecules  $cm^{-2}$  respectively [2]. The capacity for  $H_2$  pumping is in practice limited not by the bulk capacity for  $H_2$  sorption, but by surface blocking by other gettered gases, or hydride formation and embrittlement of the getter [6, 21].

**Saturation** As the surface sites are consumed during pumping, the pumping speed for gettered gases decreases due to the reduction of available sites, and/or due to surface blocking by other gases when a gas mixture is pumped, which is the normative operational condition [4]. With generalizable data shown for St 707 getter material in fig. 2.4, it is seen that when only a single gas is pumped, the pumping speed for that gas deteriorates the most rapidly for  $N_2$ , followed by  $CO$ , while up to similar pumped quantities, the pumping speed of the getter for  $H_2$  stays relatively unchanged [28]. This is in accordance with the differing mechanisms that  $N_2$  and  $CO$  are chemisorbed on the surface of the getter, while  $H_2$  diffuses and dissolves in the bulk of the layer, consequently having a larger pumping capacity [4].

From experiments of progressive saturation of TiZrV coating with single gases, the effect of surface blocking can be understood by comparing the pumping speed of  $H_2$ ,  $CO$  and  $N_2$  during surface chemisorption of  $CO$  (fig. 2.5), and  $N_2$  (fig. 2.6). These results show that  $CO$  saturation dominantly blocks the getter for both  $N_2$  and  $H_2$  sorption before pumping speed for  $CO$  would decrease, while  $CO$  pumping speed is not affected during saturating the surface with  $N_2$  [5]. This is in accordance with the measured difference in the surface capacities of  $CO$  and  $N_2$  [2], and the proposed explanation that while  $CO$  is chemisorbed by the very surface of the getter,  $N_2$  is also pumped by underlayer sorption and requires 6-8 sites per N atom [4]. The pumping speed for  $H_2$  of the TiZrV coating in both cases decreases, while pumping single  $H_2$  gas does not affect the pumping speed of other gases below the embrittlement limit according to [16], and it is also noted that complete barrier for  $H_2$  can never be created due to the size and mobility of  $H_2$  [6].

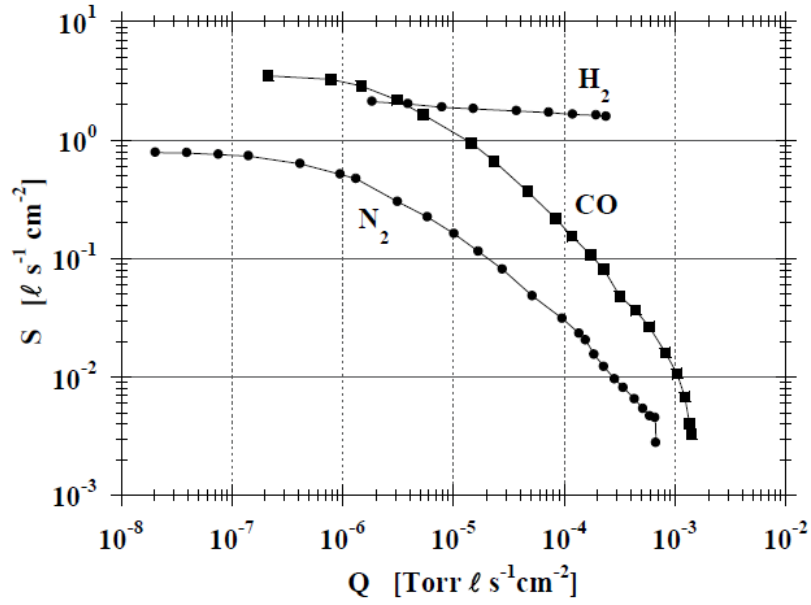


**Figure 2.4:** Pumping speed deterioration of  $\text{H}_2$ ,  $\text{CO}$  and  $\text{N}_2$  of St 707 ribbon as a function of sorbed quantity of the same single gas [28]

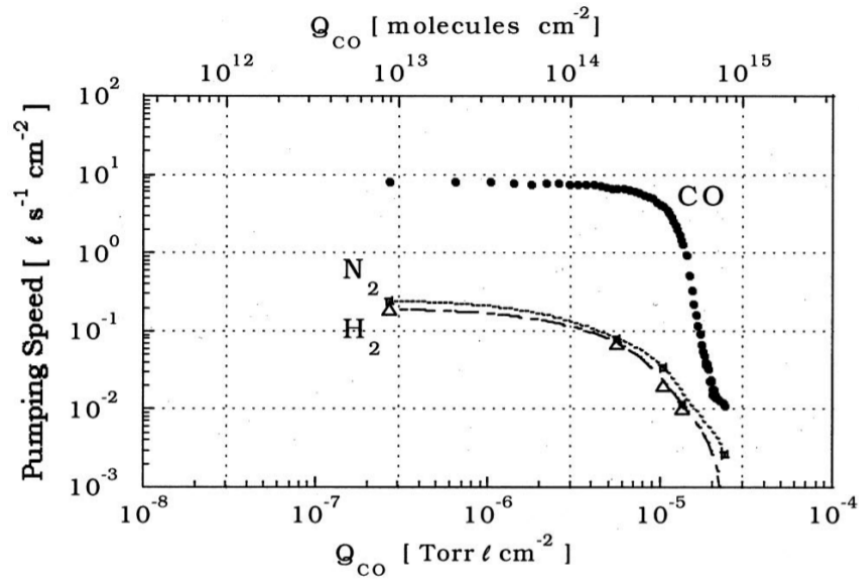


**Figure 2.5:** Pumping speed deterioration of  $\text{H}_2$ ,  $\text{CO}$  and  $\text{N}_2$  of TiZrV coating during progressive saturation of the surface with  $\text{CO}$  [5]

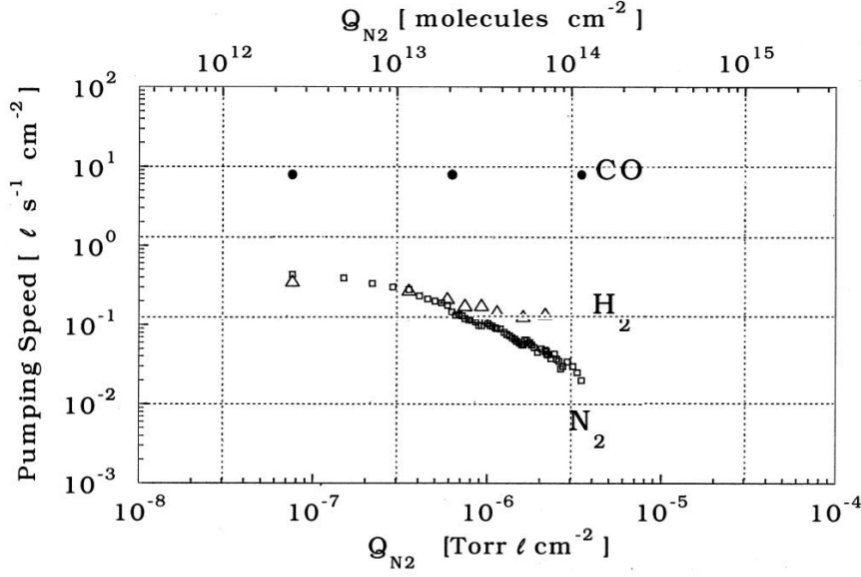


**Figure 2.6:** Pumping speed deterioration of  $H_2$ , CO and  $N_2$  of TiZrV coating during progressive saturation of the surface with  $N_2$  [5]

**Aging** Aging refers to the deterioration of the effectiveness of activation of a getter during repeated saturation/venting-activation cycles. The main explanation for aging is that if the activation temperature is not high enough, C and O does not dissolve into the bulk homogeneously, creating a gradient within the thickness of the NEG coating, which progressively hinders the dissolution of further surface gettered species during the next activation [2, 12, 29, 33, 36]. Aging affects the  $H_2$  sticking probability as well which is known to decrease with venting cycles [2]. For the TiZrV coating, 230–250 °C is found to be a sufficiently high temperature for activation, and pumping speed reduction due to aging can be counteracted by increasing the activation temperature if the application allows [2, 36].

## 2.3 Hydrogen-Getter Interactions and Embrittlement

The current section presents the relevant and available information in literature on the interaction between hydrogen and metallic getter materials. In accordance with the focus of this work, where data is available, the process of hydrogen sorption (section 2.3.1), hydride formation (section 2.3.2), and hydrogen induced embrittlement (section 2.3.3) of TiZrV alloys is discussed, otherwise the more abundantly studied H-Ti, H-Zr, and H-V systems, and their alloys are used as a reference to draw conclusions from.

### 2.3.1 Hydrogen Sorption

The process of  $H_2$  sorption consists of several consecutive steps with each of its own associated energy barrier: (i) physisorption of  $H_2$  on the getter surface, (ii) dissociation of the  $H_2$  molecule at two-site dissociation sites and formation of metal-hydrogen bond, (iii) monoatomic penetration of the hydrogen atoms through the subsurface layer, and (iv) monoatomic diffusion into the bulk of the material where hydrogen atoms occupy interstitial sites [16, 37, 38]. From the reported phase diagrams of the Ti-H [39], Zr-H [40], and V-H system [41], H terminal solubility at atmospheric pressure –solubility of H without formation of hydride phases [37]– is determined as  $<1$  at %,  $\sim 0$  at %, and  $<5$  at %, respectively, at room temperature, above which concentrations hydride phase formation is thermodynamically favored, introducing the additional steps to the sorption process of (v) hydride phase nucleation and growth. It must be noted that the terminal solubility values referenced should only be taken as a guide for alloy material systems with polycrystalline, nanocrystalline, or amorphous microstructure, such as the TiZrV NEG coating.

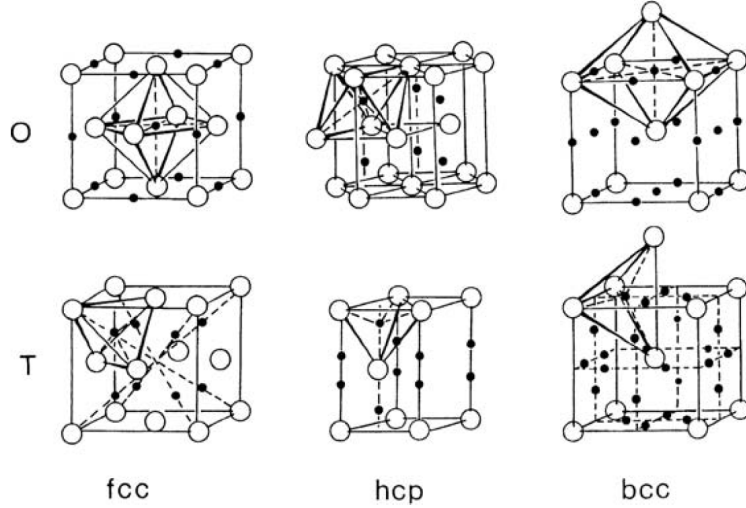


**Figure 2.7:** Octahedral (O) and tetrahedral (T) interstitial sites (solid dots) in face-centered cubic (fcc), hexagonal close-packed (hcp), and body-centered cubic (bcc) crystal lattices [37]

Hydrogen in crystalline, fcc, hcp, and bcc metals typically occupies tetrahedral and octahedral interstitial sites which are shown in fig. 2.7 [37]. In hcp metals, such as in the stable phases of Ti and Zr at standard temperature and pressure, hydrogen in solid solution is noted to primarily occupy tetrahedral sites, similarly to bcc metals, such as V [37]. In V, hydrogen can occupy tetrahedral sites, in which case typically an unordered structure forms at standard temperature, while when hydrogen occupies octahedral sites in V, it does so in a number of ordered combinations, resulting in multiple, ordered, stoichiometric vanadium-hydrides ( $V_2H$ ,  $V_3H_2$ ,  $VH$ ) [37]. In contrast to crystalline materials, amorphous metals and alloys are characterized by only short range order in their structure, which often reflects that of the stable

crystalline phase [37]. Amorphous early transition metal alloys have been previously observed to be structurally composed of “packed distorted tetrahedra”, in which hydrogen atoms occupy four coordination-number sites; distorted tetrahedral sites [37]. In amorphous alloys, it is generally observed that hydrogen sorption sites are found to have a continuous energy distribution owing to the large number of combination of geometric configurations of hydrogen sorption sites with multiple and varying potential configuration numbers [37].

The kinetics of the hydrogen sorption process is determined by the rate limiting step, commonly the  $H_2$  dissociation rate at the surface of the getter or the diffusion of monoatomic hydrogen into the bulk of the getter [38]. The molar diffusion flux  $J$  (mol/m<sup>2</sup>/s), as modeled by Fick’s 1<sup>st</sup> law in the steady-state case is obtained as

$$J = -D\nabla x \quad (12)$$

where  $D$  denotes the diffusion coefficient or diffusivity (m<sup>2</sup>/s),  $\nabla x$  the concentration gradient (mol/m<sup>3</sup>), and where the temperature dependence of the diffusion coefficient can be modeled as

$$D(T) = D_0 \exp\left(\frac{-E_A}{RT}\right) \quad (13)$$

where  $D_0$  denotes the maximal diffusivity (m<sup>2</sup>/s), and  $-E_A$  the activation energy (J/mol) [37, 42].

To provide an overview of the diffusivity of hydrogen in Ti and Zr, the tetrahedral and octahedral site sizes in crystalline Ti and Zr phases along with their respective H (with nominal atomic radius of 0.046 nm [43]) diffusivity values are tabulated in Table 2.4 [43], which highlight the differences of hydrogen diffusivity in the different allotropes of the metals. It must be noted that when hydride formation initiates, diffusivities regarding the hydride phases have to be considered as well, which are generally lower than in pure metals [44].

	Ti		Zr	
	$\alpha$	$\beta$	$\alpha$	$\beta$
$r_{th.}$ (nm)	0.033	0.044	-	-
$r_{oh.}$ (nm)	0.061	-	-	-
H $E_D$ (kJ/mol)	21.9	27.8	45.3	192
H $D_0$ (m <sup>2</sup> /s)	$1.8 \times 10^{-6}$	$2 \times 10^{-7}$	$7.7 \times 10^{-7}$	6.14
H $\sqrt{D\tau}$ at 20 °C (μm/h)	2	90	35	-

**Table 2.4:** Tetrahedral ( $r_{th.}$ ) and octahedral ( $r_{oh.}$ ) site radius of  $\alpha$  and  $\beta$  phases of Ti and Zr, together with their respective diffusion activation energy ( $E_A$ ),  $D_0$  maximal diffusion coefficient, and  $\sqrt{D\tau}$  diffusion transport distance for hydrogen [43]

### 2.3.2 Hydride Formation

Transition metals such as Ti, Zr, and V typically form metallic hydrides with hydrogen in varying ranges of nonstoichiometric compositions, where the hydrogen occupies interstitial sites, and the material system can be thought of as an alloy [37]. As a result of hydrogen uptake, the crystal structure of the material might accommodate itself via phase transformations, which means that multiple metal-hydrogen phases can exist at different hydrogen contents [37]. The equilibrium phases in a hydrogen-metal system does not only depend on the composition and the temperature, but also the  $H_2$  partial pressure, highlighted by pressure-composition diagrams [38, 45, 46]. The hydrides of Ti, Zr, and V at standard temperature and pressure are observed to form fcc crystal structure as tabulated in table 2.5. The dihydrides of Ti and Zr take up  $CaF_2$  fcc structure in which hydrogen is noted to occupy tetrahedral sites, similarly to the solid solution [37].

	Crystal structure	$\Delta H$ (eV per atom)	$\Delta S/k$	$T$ ( $^{\circ}C$ )
Ti	hcp	-	-	-
Zr	hcp	-	-	-
V	bcc	-	-	-
$TiH_{2\pm\beta}$	fcc	-0.68	-6	<300
$ZrH_{2-\beta}$	fcc	-0.98	-9	400–550
$VH_{1-\alpha}$	fcc	-	-	-
$VH_{2-\alpha}$	fcc	-0.21	-9	50–120

**Table 2.5:** Crystal structure of Ti, Zr, and V in their stable phases at standard temperature and pressure together with the observed structure of their hydrides, with the formation enthalpy ( $\Delta H$ ) and formation entropy ( $\Delta S/k$ ) of the stoichiometric hydride phases included. The temperature ranges pertaining to the thermodynamic data are included as well [37]

In the study of Efron et al., titanium hydride formation kinetics and mechanism was studied in the range of 100–250  $^{\circ}C$  and  $\sim 40$ – $\sim 600$  hPa on a Ti sample with  $>100 \mu m$  grain size to find continuous formation of a homogeneous hydride layer on the surface of Ti, eventually leading to cracking on the surface attributed to strain accumulation as a result of hydride formation. The authors also demonstrate that the topochemistry of hydride growth depends on exposure pressure and temperature, and does not always result in a homogeneous hydride front propagation [44]. Similarly, in the review of both Bloch and Mintz [47], and Modi and Aguey-Zinsou [38], three topochemically different hydride formation, and consequent crack formation mechanisms are summarized as shown in fig. 2.8 that have been observed for different hydride forming metal systems under different temperature and pressure condition.

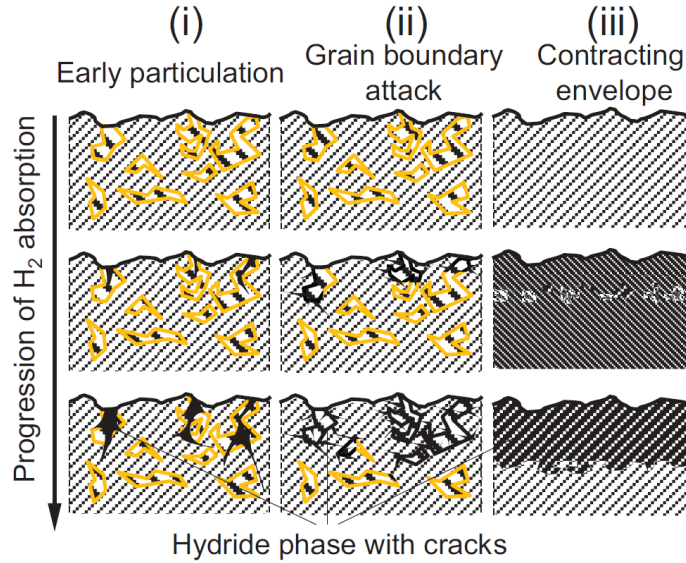


**Figure 2.8:** Mechanisms and pathways proposed and observed for hydride formation of metals or metallic systems [38]

### 2.3.3 Hydrogen Induced Embrittlement

Hydrogen embrittlement refers to loss of ductility in metals and alloys as a result of hydrogen absorption, and covers a wide range of phenomena, with not always clear consensus in literature on the underlying mechanisms behind hydrogen embrittlement [48]. In steels, hydrogen embrittlement is commonly associated with stress-corrosion cracking, hydrogen induced cracking, and hydride cracking, through hydrogen induced decohesion, hydrogen enhanced localised plasticity, hydrogen induced phase transformation, hydrogen enhanced strain induced vacancy formation, and adsorption induced decohesion mechanisms, providing both microscopic and macroscopic mechanisms for observed ductility loss in steels due to the presence of hydrogen [49].

Hydrogen embrittlement in Ti, Zr, and V, and their alloys have only been studied since recent decades. For Ti and Zr systems, multiple effects related to H<sub>2</sub> sorption have been observed and are proposed to contribute to an eventual failure of gettering materials [43]: fracture toughness reduction, fatigue crack propagation rate increase, and cold dwell fatigue. Besides the facilitation of local crack formation as a result of hydrogen migration to regions in tensile stress in the material in solid solution [38], hydrogen embrittlement in hydride forming getter materials are mainly associated with brittle hydride phase formation in the matrix which is in fact facilitated at crack tips [16, 38]. As hydride phases have generally lower density than the matrix, and are also more brittle, the formation of hydride phases introduces sources of mechanical stress, as well as mechanical weak points in the material [37, 50], which, in extreme cases have been observed to result in powdery peel-off of NEG materials

after excessive  $\text{H}_2$  sorption through crack propagation through either through the hydride phase or along the hydride-matrix grain boundary [16, 38].

In experiments of Malinowski [51], St 707 getter was passivated with CO, as well as  $\text{CO}_2$  and air, and  $^2\text{H}_2$  pumping speed was measured as a function of high pressure  $^2\text{H}_2$  exposure at 0.0133–1.332 hPa to study if surface gettered gases can completely passivate the getter to be protected from  $^2\text{H}_2$  sorption at such high pressures, and consequent embrittlement. It was observed, that while passivation reduced the  $^2\text{H}_2$  pumping speed to 0.001 of the nominal value of the getter, only 3 min of high pressure  $^2\text{H}_2$  exposure leads to an increase of the  $^2\text{H}_2$  pumping speed, eventually leading to an aggressive flaking process in which the getter came off of its substrate shooting off at velocities of around 1 m/s [51]. These results indicate that it seems virtually impossible to create a complete surface barrier for  $\text{H}_2$  sorption, as well as that hydride formation causes significant volume expansion and consequent stresses in a getter.

The embrittlement limit for NEG pumps refers to the quantity of sorbed hydrogen at which hydride formation takes place leading to the mechanical disintegration of the getter material in the form of flaking, peel-off, or powdering. The embrittlement limit for NEG pumps is typically obtained empirically and is reportedly in the range of a few tens of  $\text{hPa dm}^3 \text{g}^{-1}$ ,  $\sim 26 \text{ hPa dm}^3 \text{g}^{-1}$  for St 707 and St 101 getters [6, 52]. Detailed data available was not found in literature at the time of writing on the  $\text{H}_2$  embrittlement of the TiZrV NEG coating, identified as the state-of-the-art NEG coating used in modern particle accelerators, such as the LHC [12]. Furthermore, the hydrogen embrittlement of the TiZrV NEG coating has recently gained technical relevance due to the System for Measuring Overlap with Gas 2 (SMOG2) upgrade at the Large Hadron Collider beauty (LHCb) experiment [23, 24], allowing for  $\text{H}_2$  injections into the beam vacuum near NEG coated vacuum equipment. Since the embrittlement of the coating, potentially resulting in flaking or peel-off of the coating in the machine would seriously disrupt its safe operation and could be catastrophic, the goal of this work is defined as studying the effect of  $\text{H}_2$  loading on the functionality and the mechanical integrity of the TiZrV getter coating, with the potential of observing embrittlement, previously not noted in literature.

## Chapter 3

# Materials and Methods

As defined in chapter 1, the main goal of this work is to contribute to the characterization of H<sub>2</sub> saturation of the TiZrV non-evaporable getter (NEG) coating with the prospect of observing H<sub>2</sub> induced embrittlement of the coating. To achieve this, H<sub>2</sub> saturation experiments were conducted on TiZrV coated pipes and the coating was characterized in terms of functionality and materials properties.

The preparation of the reference, uncoated test pipe and the two TiZrV coated test pipes used in the saturation experiments are detailed in section 3.1. As the H<sub>2</sub> sorption and saturation processes of Ti, Zr, and V are pressure dependent, two H<sub>2</sub> saturation conditions were defined. Section 3.2 presents the details of the high pressure (HP) experiments in which H<sub>2</sub> was injected instantaneously at a nominal pressure of 1 hPa to study the gettering of the TiZrV coating in the viscous flow regime. In the second, low pressure (LP) experimental condition, H<sub>2</sub> was injected at a nominal pressure  $5 \times 10^{-7}$  hPa continuously over a longer period of time, as detailed in section 3.3, with the goal of simulating the conditions the TiZrV coated beam pipes face in the Large Hadron Collider beauty (LHCb) machine during H<sub>2</sub> injection for the fixed target experiments. Section 3.5 provides details on the materials characterization methods that were deployed to identify and explain trends observed in the saturation experiments. In section 3.6, simulation techniques are described which were used to aid the interpretation of the results obtained through the vacuum experiments and materials characterization. In section 3.7 an overview is provided of the materials characterization sample matrix. All experiments, including the sample deposition, vacuum experiments, and materials characterization were carried out in the laboratory facilities of the European Organization for Nuclear Research (CERN), unless specified otherwise.

### 3.1 Sample Preparation

Three 2 m long and 3.5 cm internal diameter 304L stainless steel pipes with 2 mm wall thickness were prepared to serve as test pipes in the saturation experiments. 304L stainless steel DN 40 flanges were orbital welded to the two ends of the test pipes after which they were subjected to a wet chemical cleaning procedure for degreasing

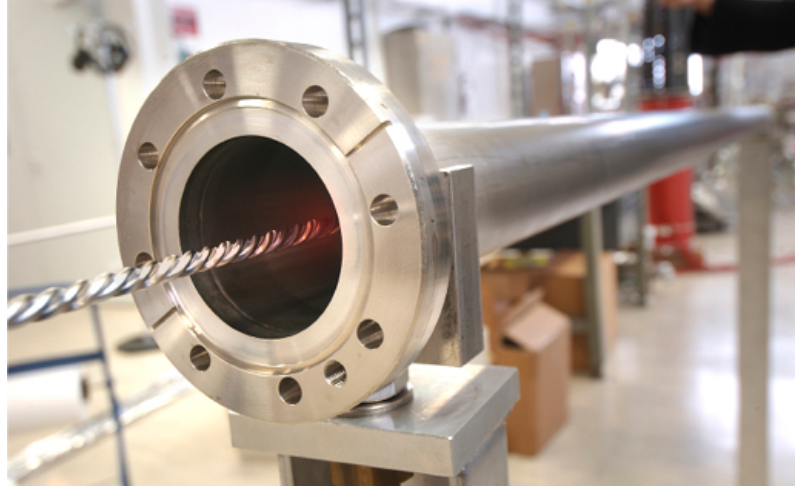


**Figure 3.1:** Intertwisted Ti, Zr, and V wires serving as the cathode for the TiZrV direct current (DC) magnetron sputtering shown as being inserted into the test pipe [53]

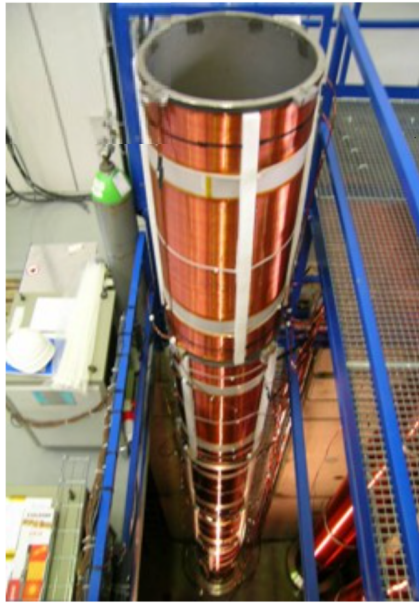


**Figure 3.2:** Top perspective view of the solenoid used in the TiZrV DC magnetron sputtering deposition process [54]



**Figure 3.3:** Witness samples placed inside the test pipes at their entrance before the start of the experiments

as described in [55] followed by vacuum firing [18] at  $650^{\circ}\text{C}$  for 24 h which served the purpose of removing the H content from the stainless steel before the NEG deposition. One pipe was left uncoated to be used as reference for the calibration of the vacuum experiment test benches, and two were coated with TiZrV getter layers.

The deposition of the coating in the targeted thickness of 1  $\mu\text{m}$  [2] was carried out by DC magnetron sputtering from 1 mm diameter elemental intertwtisted cathode wires (fig. 3.1) under Kr atmosphere in a solenoid (fig. 3.2) specifically designed for TiZrV deposition on beam pipes for the Large Hadron Collider (LHC) as detailed in [2]. The pipes were inserted into the solenoid as part of a vertically suspended pipe assembly which was kept at 100 °C during deposition. The two coated pipes are labeled as NEG1 and NEG2; NEG1 was used for the LP, and NEG2 was used for the HP experiments. The deposition parameters of the two coating processes are detailed in table 3.1. The test pipes were kept under N<sub>2</sub> atmosphere both before and after the deposition process, and a 48 h bake-out at 150 °C preceded the deposition.

	Power (W)	Voltage (V)	Current (mA)	Pressure (hPa)
<b>NEG1</b>	150	450	330	$1.2 \times 10^{-2}$
<b>NEG2</b>	130	380	330	$5.2 \times 10^{-2}$

**Table 3.1:** Deposition parameters of TiZrV coating of the two 304L stainless steel pipes serving as the test pipes for the low pressure (NEG1) and the high pressure (NEG2) H<sub>2</sub> saturation experiments

To create TiZrV samples in dimensions that can be used for materials characterization, dedicated TiZrV coated witness samples were deposited under identical conditions as the coating of the test pipes. In the supporting pipes adjacent to the test pipe in the pipe assembly, 0.5 mm thick and 150 mm wide 304L stainless steel rings were inserted near the pipe entrance, formed by creating two long cuts at the ends of the thin substrate plates and by which they were mechanically interlocked. Eight of the witness samples were placed inside the test pipes before the start of the experiment (see fig. 3.3) at the entrance of the pipes mounted to the test bench, and the rest of the witness samples were used for characterization of the as-deposited layer, as well as for the reference activation cycle.

## 3.2 High Pressure Experiment

The high pressure experimental condition was designed to study the H<sub>2</sub> sorption and potential embrittlement of the TiZrV coating when subjected to a nominally immediate surge of H<sub>2</sub> gas in the viscous flow regime where the whole length of the test pipe performs pumping.

The experiments were carried out in an all-metal vacuum experiment test bench (see fig. 3.4), referred to as “Test bench 1” which was designed for high and ultra-high vacuum experiments. The test bench has a total volume of 25.45 dm<sup>3</sup> with the test pipe mounted. The schematic of the test bench is shown in fig. 3.5. It is equipped with a pumping group consisting of a Pfeiffer TMH 071 P turbomolecular drag pump which is backed by an Edwards RV12 rotary vane pump. The pumping group is connected to the measurement dome by a VAT 541 all-metal angle valve and its effective pumping speed for H<sub>2</sub> at room temperature (293.15 K) at the entrance

to the dome is  $39.8 \text{ dm}^3/\text{s}$ . The valve between the turbomolecular pump (TMP) and the backing pump allows connection to a secondary pump for leak detection with a mobile leak detector. The test bench can be considered a Fischer-Mommsen dome; it is separated into two volumes (dome and cross) by a 1 cm diameter aperture which has a conductance of  $34.7 \text{ dm}^3/\text{s}$  for  $\text{H}_2$  and  $9.3 \text{ dm}^3/\text{s}$  for  $\text{N}_2$  and  $\text{CO}$  at room temperature. The volume to the pumping group (dome) is connected to the injection line through a manually operated Agilent 951-5106 variable leak valve, with an interposed VAT 541 DN 16-63 mm all-metal angle valve used for venting. The injection line provides connection to  $\text{H}_2$ ,  $\text{N}_2$  and  $\text{CO}$  gas bottles and is pumped by its own pumping group after an angle valve in an identical configuration to that of the test bench. The gas bottles were obtained from Carbagas in  $1 \text{ dm}^3$  bottles with 20 MPa filling pressure and with a purity of 99.9997 % ( $\text{H}_2$ ), 99.9997 % ( $\text{N}_2$ ), and 99.997 % ( $\text{CO}$ ).

The pressure in the test bench between  $1 \times 10^3$ – $5 \times 10^{-9}$  hPa is monitored with a Pfeiffer PKR 261, metal-sealed, DN 25 ISO-KF compact full-range gauge (FRG) mounted in the dome volume. The FRG operates as a Pirani gauge between  $1 \times 10^3$ – $1 \times 10^{-2}$  hPa and as a cold cathode gauge between  $1 \times 10^{-2}$ – $5 \times 10^{-9}$  hPa. For the high pressure injections, a Pfeiffer CMR 374 DN 16 ISO-KF active capacitance gauge (ACG) was specifically installed by a T connection to the cross of the test bench operating between  $1 \times 10^{-4}$ –1.1 hPa to monitor the pressure during the high pressure injections. The test bench is also equipped with three calibrated custom-made Bayard-Alpert type emitting cathode gauges (ECGs) which are used to monitor the pressures in high vacuum (but maximum below  $5 \times 10^{-5}$  hPa) and are mounted at the dome (ECG-1), at the cross (ECG-2), and at the end of the test pipe (ECG-3). Since the cold cathode gauge in the FRG and the ECGs operate by gas ionization, their pressure reading is rather related to the temperature independent number density ( $\rho_n$ , see eq. (1)) of the gas and are read as room temperature  $\text{N}_2$  equivalent pressures [56]. When applicable, the pressures were converted into  $\text{H}_2$  equivalent pressures by calibration constants tabulated in table A.3.

The composition of the vacuum during the experiments was monitored by residual gas analysis measurements carried out by a Hiden RGA-HAL 3F quadrupole mass spectrometer (referred to as the residual gas analyzer (RGA)) mounted at the cross after the T connection of the ACG. Scans with steps of  $0.05 \text{ m/z}$  were taken using the secondary electron multiplier detector at 1100 V, and Multiple Ion Detection mode was operated during the transmission method measurements to follow the partial pressures of  $m/z$  2, 12, 14, 15, 16, 17, 18, 28, 32, 40, and 44 to monitor cleanliness and potential contamination during injection.

The HP experiments were carried out in cycles that can be simplified as consecutive steps of activation, injection, reactivation, and venting. Within the cycles, the effect of  $\text{H}_2$  injection on the sticking coefficient of the NEG coating is studied, as well as the regenerability of the sticking coefficient after the injection by a reactivation. Between the cycles, the effect of aging is studied, which is related to the formation of an additional layer of native oxide during air exposure after venting at every cycle. Four witness samples were placed inside the test pipe at the end which is mounted to the test bench before the start of the cycles. A HP cycle lasts approximately two

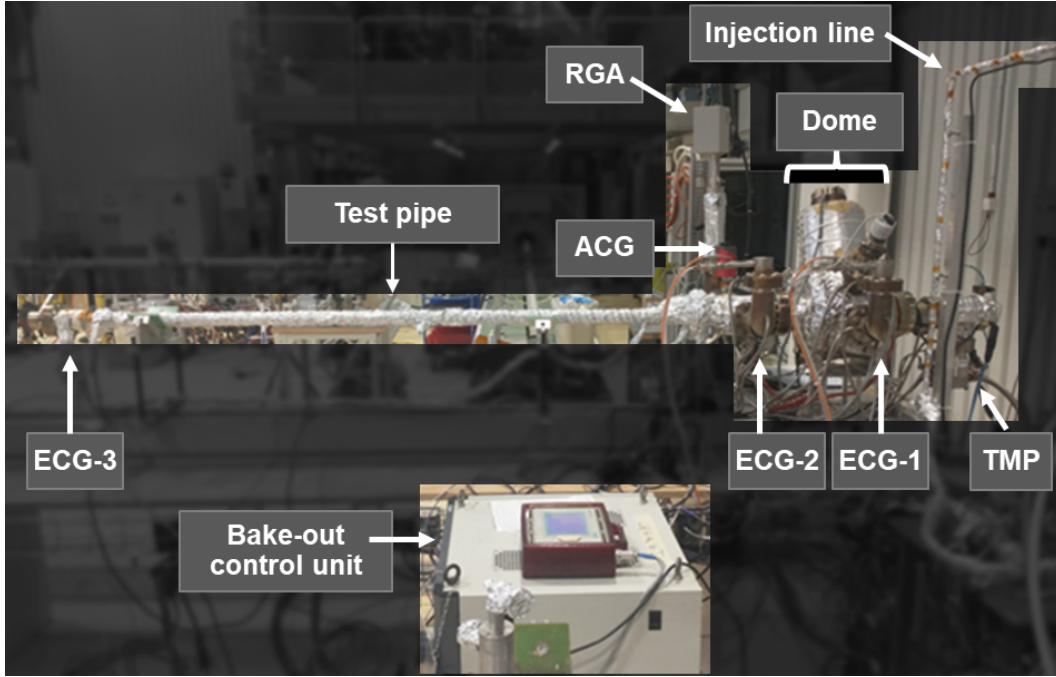


**Figure 3.4:** Test bench 1 used for the high pressure experiment with heating equipment and Al foil insulation installed

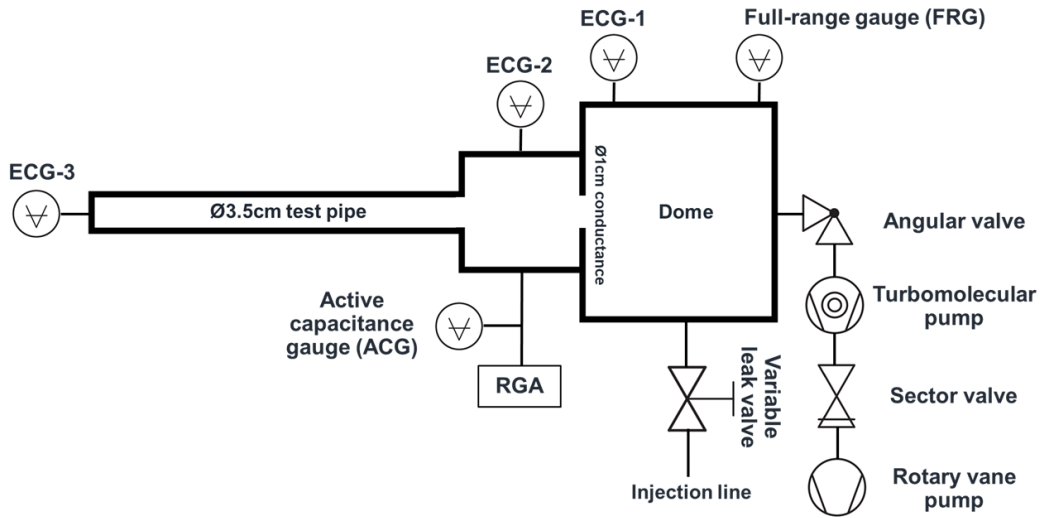


**Figure 3.5:** Schematic of the test bench in fig. 3.4 used for the high pressure experiment

weeks (see fig. 3.6) and its steps are as follows:

#### 1. Installation

The test pipe is mounted to the test bench, heating bands are installed on the test pipe and then covered in commercial Al foil to provide insulation

### 3. MATERIALS AND METHODS

---

during the activation. The pumping group of the test dome is started and the FRG is turned on. The leak tightness of the connections are tested by a Phoenix L300i mobile helium leak detector when the pressure is below  $1 \times 10^{-5}$  hPa.

#### 2. Bake-out and activation

As the leak tightness of the system is confirmed, the bake-out and activation procedure is started according to the temperature profile in fig. A.1, which follows the standard procedure practiced also in the LHC [12].

Firstly, a bake-out is performed during which the wall of the test pipe is kept at  $120^\circ\text{C}$  for 24 h while the rest of the test bench undergoes a bake-out, in order to accelerate –primarily  $\text{H}_2\text{O}$ – desorption from its surfaces. Afterwards, the rest of the test bench is cooled to the degassing temperature, the ECGs and the RGA are progressively degassed and then turned off.

Then, the TiZrV coated test pipe is heated with  $50^\circ\text{C}/\text{h}$  heating rate to the  $230^\circ\text{C}$  activation temperature where it is kept for 24 h. At the end of the activation (except for the 1<sup>st</sup> cycle where the pressure was sufficiently low), the temperature of the test pipe is decreased to  $150^\circ\text{C}$  for the pressure to be sufficiently low for the degassing, and then the ECGs and the RGA are degassed and turned on, and then the cooling of the system to room temperature is initiated. The ultimate pressure after activation is registered as the pressure reading on the ECG-3 gauge 24 h after the system being cooled down to room temperature.

#### 3. Sticking coefficient measurement

The sticking coefficient for  $\text{H}_2$  of the TiZrV coating is estimated by the transmission method. The principle of the transmission method is registering the pressure ratio of the pressure at the entrance (ECG-2) and at the end (ECG-3) of the TiZrV coated pipe during increasing steps of constant flow of the test gas, which is  $\text{H}_2$  gas here. The sticking coefficient then is estimated from the ratio  $\frac{p_{\text{ECG-2}}}{p_{\text{ECG-3}}}$  through molecular flow test particle Monte Carlo simulations which establish the relationship between the sticking coefficient and the transmission ratio  $\left(\frac{p_{\text{ECG-2}}}{p_{\text{ECG-3}}}\right)$ . The transmission method and the simulations for estimating the sticking coefficient are further detailed in appendix A.2.3 and section 3.6.3, respectively.

#### 4. High pressure injection

The ECGs and the RGA are turned off and the test bench is put into static vacuum by isolating it from its pumping group by closing the angle valve.  $\text{H}_2$  is injected into the test bench; the variable leak valve is opened in  $<1$  min until 1 hPa is reached after which the variable leak valve controlling the injection flow is closed (see fig. A.3). The pressure during the injection is monitored by the FRG and the ACG, and the FRG is turned off as soon as the variable leak valve is fully closed. Based on the experience of the 1<sup>st</sup> cycle, the pressure in the system was measured with ECG-2 5 min after the closing of the variable leak valve, and then in half hour intervals

up to 2 h when the pressure was determined to be stable in all cycles. Afterwards, the angle valve is opened and the test bench is pumped by the pumping group and the RGA and the ECGs are turned back on. 24 h after opening the angle valve, the ultimate pressure after injection is recorded.

**5. Sticking coefficient measurement**

The sticking coefficient for  $H_2$  of the TiZrV coating is estimated by the transmission method as described previously and is referred to as the sticking coefficient after high pressure injection.

**6. High pressure injection**

The high pressure injection step is repeated in the same way as described previously.

**7. Sticking coefficient measurement**

The transmission method was performed as described previously. In all cycles at this stage, the pressure at the end of the test pipe exceeded the pressure at the entrance of the test pipe, indicating that the TiZrV coating has no pumping effect at this stage and therefore the sticking coefficient is not reported after the second high pressure  $H_2$  injection.

**8. Reactivation**

The ECGs and the RGA are turned off, and the test bench except for the test pipe is heated to its respective degassing temperature (see fig. A.1). When the pressure reaches stability, the test pipe walls are heated to 230 °C with a ramp rate of 100 °C/min for a 24 h activation, at the end of which its temperature is lowered to 150 °C and the ECGs and the RGA are progressively degassed and turned on. The test bench is then cooled down to room temperature and 24 h after being at room temperature the pressure reading on the ECG-3 gauge is recorded as the reactivation ultimate pressure.

**9. Sticking coefficient measurement**

The sticking coefficient for  $H_2$  of the TiZrV coating is estimated by the transmission method referred to as the reactivation sticking factor.

**10. Venting, dismounting, witness sample retrieval and visual inspection**

The gauges are turned off, the test bench is isolated by closing the angle valve and the pumping group is turned off. The test bench is vented with ambient air through its venting valve, and then the test pipe is dismounted and opened to ambient air. The surface of the coating after every cycle was then visually inspected from the two ends of the test pipe. At the end of the 3<sup>rd</sup> and the 6<sup>th</sup> cycle the test pipe was also inspected by performing endoscopy over the whole length of the pipe. After each cycle, half of a witness sample was retrieved and cut into approximately 1 cm × 1.5 cm pieces, which were then characterized by the characterization methods as tabulated in section 3.7. The witness samples are labeled as “HP-□” with the number at “□” referring to the number of cycles it has been subjected to; HP-0 refers to as-deposited samples not subjected to any cycle, and HP-0A refers to witness samples subjected to only the reference activation described in section 3.4. The venting time between cycles was <24 h in

most cases, and at least 4 h.

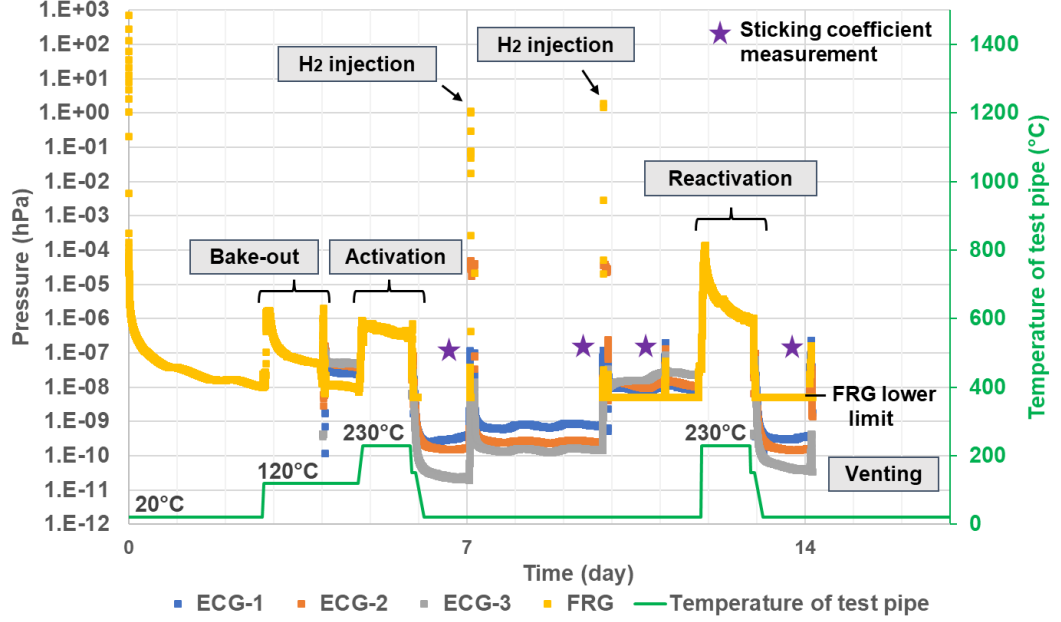


**Figure 3.6:** Pressure profile of one single high pressure experimental cycle with the different stages labeled: bake-out and activation, high pressure injections, reactivation, venting, and the transmission method measurements in-between at the indicated stages, with the temperature profile of the test pipe also included

**Calibration** Before the start of the 1<sup>st</sup> cycle, the test bench was calibrated by performing the first 3 steps of the HP cycle with the uncoated test pipe: installation, bake-out and activation, and transmission measurement. The pressure readings during this transmission measurement was used for all the experiments with the coated test pipes to correct the pressure gauges to the reading of ECG-2; the correction factors are tabulated in table A.4.

**Injection Line** The injection line was baked-out at 150 °C for 24 h and was in dynamic vacuum when not used for transmission or injection. As the injection line is connected to the test bench of the low pressures experiment as well where experiments with not only H<sub>2</sub> were performed, before using the injection line, it was rinsed 3 times by filling it up with H<sub>2</sub> to 1500 hPa and pumping down to below  $1 \times 10^{-6}$  hPa, after which it was filled up again to 1500 hPa with the gas bottle left open to the injection line during injection and transmission measurements to ensure the cleanliness of the injection.

### 3.3 Low Pressure Experiment

In order to simulate the sorption, saturation and potential embrittlement behavior of the TiZrV coating during the planned H<sub>2</sub> injections during fixed target experiments at the LHCb experiment, the LP experimental condition was devised. The low pressure H<sub>2</sub> injection experiment was performed by injecting H<sub>2</sub> continuously at a nominal pressure of  $5 \times 10^{-7}$  hPa over four months in the test bench (“Test bench 2”) to which the NEG1 TiZrV coated test pipe was mounted. Test bench 2 is identical to Test bench 1 used for the HP experiments except for the T connection and the mounted ACG gauge which is not present in the LP test bench; Test bench 2 has an overall volume of 25.06 dm<sup>3</sup> with the test pipe mounted. Test bench 1 and Test bench 2 also share the same injection line.

The goal of this campaign was to characterize the evolution of the H<sub>2</sub> sticking coefficient of the TiZrV coating during continuous injection of H<sub>2</sub> at  $5 \times 10^{-7}$  hPa, as well as the effect of the sorbed H<sub>2</sub> content in the TiZrV coating on its sticking coefficients for N<sub>2</sub> and CO which has not been reported in literature before.

The calibration constants for the high vacuum gauges of the test bench are included in table A.3 for conversion into H<sub>2</sub> and CO equivalent pressures. The LP experiment was also preceded by a calibration using the uncoated test pipe similarly as described in section 3.2 and the correction factors obtained are reported in table A.4.

Before the start of the experiment, four witness samples from the NEG1 deposition were inserted into the TiZrV coated test pipe near its entrance mounted to the test bench. The experimental procedure of the LP condition is as follows:

1. **Installation**

The test pipe is mounted to the test bench, heating bands are installed on the test pipe and then covered in commercial Al foil to provide insulation in the next step. The pumping group of the test dome is started and the FRG is turned on. The leak tightness of the connections is tested when the pressure is below  $1 \times 10^{-5}$  hPa by leak detection through the mobile leak detector.

2. **Bake-out and activation**

Bake-out followed by the activation is performed according to the temperature profile as presented in fig. A.1. The ultimate pressure in the test bench 24 h after cooling down to room temperature is reported as the pressure measured on ECG-3 at the end of the test pipe.

3. **Sticking coefficient measurement for N<sub>2</sub> and CO**

The sticking coefficients for N<sub>2</sub> and CO is measured before the start of the H<sub>2</sub> injection by the transmission method as described previously, with the only difference that in these measurements it is done only in one step lasting approximately 10–20 s.

4. **Continuous low pressure H<sub>2</sub> injection with intermittent N<sub>2</sub> and CO sticking coefficient measurements**

With the ECGs on, the variable leak valve is opened up to  $5 \times 10^{-7}$  hPa N<sub>2</sub> equivalent pressure as read on ECG-2. At regular intervals, the variable

leak valve is closed for the pressure to be regenerated, when N<sub>2</sub> and CO sticking coefficients are measured by the transmission method in a similar way as measured before the start of the H<sub>2</sub> injection, after which the H<sub>2</sub> injection is restarted.

#### 5. Reactivation

Reactivation is performed similarly as in the HP experimental condition.

#### 6. Sticking coefficient measurement

The sticking coefficient for H<sub>2</sub>, as well as for N<sub>2</sub> and CO of the TiZrV coating is estimated by the transmission method referred to as the reactivation sticking factors.

#### 7. Venting, dismounting, witness sample retrieval and visual inspection

The gauges are turned off, the test bench is isolated by closing the angle valve and the pumping group is turned off. The test bench is vented with ambient air through its venting valve and the test pipe is dismounted. The coating surface is inspected by endoscopy and witness sample are retrieved for materials characterization.

The sticking coefficient evolution during the continuous H<sub>2</sub> injection is obtained from the transmission ratio  $\frac{p_{ECG-2}}{p_{ECG-3}}$ , from which the pumping speed of the NEG coating is also calculated (eq. (9)). Then, through eq. (8), the flow rate of sorbed H<sub>2</sub> into the coating is obtained, and the absorbed H quantity in the TiZrV coating is estimated through the area under the  $Q(t)$  curve.

Before the start of the experiment, similarly as in Test bench 1, the ionizing pressure gauges of Test bench 2 were also calibrated using the uncoated test pipe, and the obtained correction factors can be found in table A.4. Since the injection line was used to provide H<sub>2</sub>, but also N<sub>2</sub>, and CO to Test bench 2, before each transmission method measurement, or the H<sub>2</sub> injection, the injection line was rinsed 3 times with the respective gas to ensure its cleanliness, in the same way as described in section 3.2.

### 3.4 Reference Activation

In order to study the effect of activation separately from the H<sub>2</sub> injections, HP and LP as-deposited witness samples were prepared and placed inside the test pipe subjected to the LP experiments and were activated in the reference activation cycle in the following steps:

#### 1. Installation

The test pipe is mounted to the test bench as described previously with the witness samples placed near the entrance of the test pipe.

#### 2. Bake-out and activation

Bake-out and activation is performed according to the temperature profile as presented in fig. A.1.

#### 3. Reactivation

Reactivation is performed identically as in the HP experimental condition.

#### 4. Venting, dismounting, witness sample retrieval and visual inspection

After turning off the gauges and the pumping group, the test bench is vented with air through its venting valve, and the test pipe is dismantled, and the witness samples (HP-0A and LP0A) are retrieved.

### 3.5 Materials Characterization Techniques

Various materials characterization techniques were deployed to characterize the chemical composition and other important properties of the TiZrV NEG coating. This section lists the techniques and the practical details of each method, and the chapter is concluded with an overview of the witness sample characterization matrix in section 3.7 detailing which samples were subjected to which measurements.

**X-ray Photoelectron Spectroscopy** The surface composition and chemical state of surface species of the witness samples was studied by X-ray photoelectron spectroscopy (XPS). The XPS measurements were performed in a SPECS system with Phoibos 150 hemispherical electron analyzer equipped with 9 channeltrons using monochromated Al K-alpha radiation ( $h\nu = 1486.7$  eV). Survey spectra were recorded with 50 eV constant pass energy and 30 eV constant pass energy was used for detailed spectra. The area of analysis is approximately  $0.8 \text{ mm}^2$  and the element dependent detection limit is estimated at 0.1 at % on average. The samples were measured in their as-received condition, as well as during in-situ activations at  $160^\circ\text{C}$ ,  $200^\circ\text{C}$ , and  $250^\circ\text{C}$  temperatures with a 1 h activation duration each. The samples were heated through the sample holder with a ramp rate of  $5^\circ\text{C}/\text{min}$ , and were tested with XPS at the activation temperature. The binding energy spectra was analyzed with the help of data available from the National Institute of Standards and Technology (NIST) X-ray Photoelectron Spectroscopy Database [57], as well as previous studies on the TiZrV NEG coating [4, 33].

**Secondary Electron Yield Measurement** Besides the pumping capability of the TiZrV getter coating quantified by its sticking coefficient, another important parameter for its function as a coating in the particle accelerator is  $\delta$ , the secondary electron yield (SEY) of the surface. The SEY is defined as

$$\delta = \frac{I_{SE}}{I_{PE}} \quad (1)$$

as the ratio of emitted secondary electron current ( $I_{SE}$ ) to the impinging primary electron current ( $I_{PE}$ ) the investigated surface is subjected to [33].

There are multiple potential origins of primary electrons in particle accelerators; electrons leaving the beam vacuum surfaces produced by the photoelectric effect induced by the synchrotron radiation that is emitted by the circulating beam, as well as the by-product of the ionization of the residual gas in the vacuum due to its interaction with the beam [58]. The released, free electrons in the beam vacuum interact with the oscillating electromagnetic field and are periodically accelerated towards the beam vacuum surfaces, where they can be backscattered, induce a

pressure rise in the beam vacuum by stimulating desorption (referred to as electron stimulated desorption), as well as produce secondary electrons. If the rate of secondary electron generation substantially exceeds that of the primary electrons, the process can become self-accelerating, leading to the phenomenon referred to as electron multipacting, or the electron cloud effect [58]. Electron multipacting can reduce beam lifetime and induce beam instabilities, therefore, minimizing electron multipacting is an important aspect of designing the vacuum surfaces in a particle accelerator. One way for its mitigation is to ensure the low SEY of the surfaces in the beam vacuum; a maximum SEY value of 1.35 is cited for the getter surface in the LHC [33].

The SEY of the witness samples were measured in the same set-up as the XPS machine. SEY was measured in as-received condition, as well as after the in-situ activation, after being cooled down to room temperature, referred to as the activated condition. The samples were irradiated with an ELG-2/EGPS-1022 Kimball Physics electron gun from a normal incidence, and the SEY spectra were recorded at primary electron energies ranging between 40–1800 eV. In the measurement procedure, the current is measured from the sample through the sample holder during irradiation with the primary electrons. During applying firstly a positive sample bias (45 V) the sum of the primary electron and the secondary electron current is collected ( $I_{SE} + I_{PE}$ ), after which a negative sample bias (−45 V) is applied during which only the primary electron current ( $I_{PE}$ ) is collected;  $I_{SE}$  is obtained from the difference of the two. The SEY values are reported as the average of SEY values from three different locations from each sample.

**X-ray Fluorescence Spectroscopy** The composition and the thickness of the TiZrV coating was analyzed by X-ray fluorescence spectroscopy (XRF) with a Fischerscope X-ray XDAL machine, and the reported values are averaged over five measurement points with 1 mm diameter spot size per each sample.

**Focused Ion Beam and Scanning Electron Microscopy Imaging** Focused ion beam (FIB) and scanning electron microscopy (SEM) imaging together with energy dispersive X-ray spectroscopy (EDX) point measurements of the cross-section of the coating in a Zeiss XB540 FIB/SEM system were used to cross-validate the coating thickness and composition measurements with XRF. The samples used for cross-section imaging were coated with Pt. SEM imaging of the top surface of the coating was also used to characterize the surface topology of the TiZrV coating at various magnifications.

**X-ray Diffraction** X-ray diffraction (XRD) measurements were carried out to study the crystallinity of the coating with a Bruker D8 Discover machine using Cu K-alpha radiation, equipped with an Eiger 2R 500K multi-mode (0D/ 1D/ 2D) Hybrid Photon Counting detector with 500000 pixels and 75  $\mu\text{m}$  pixel size. Initially, grazing incidence XRD measurements were taken on the witness samples, however, due to sample unevenness and the reflections from the substrate, the decision was

made to use TiZrV powder instead to be able to detect the reflections from the coating material. The TiZrV coating was mechanically removed from the substrate as powder and for the XRD measurement it was placed in a polymethyl methacrylate sample holder. XRD patterns were registered between 30–130°  $2\theta$  with a step of 0.1° and 3 s acquisition time per step. The XRD patterns were analyzed by MAUD software [59] and compared with previous studies on the XRD analysis of the TiZrV coating [4, 60].

**Thermal Desorption Spectroscopy** Thermal desorption spectroscopy (TDS) is a technique used to study the quantities and kinetics of desorption of gaseous species from solid samples during a heating process under vacuum [61]. The TDS system used for the characterization is an all-metal vacuum system consisting of a load lock and a measurement chamber that are pumped separately with pumping groups with 160 dm<sup>3</sup>/s effective pumping speed. The sample is introduced via the load lock ( $1 \times 10^{-7}$  hPa) onto the sample holder in the baked measurement chamber ( $\sim 1 \times 10^{-9}$  hPa) where it is held down by the four feet of the entrance to the RGA. Samples were heated at a constant heating rate of 5 °C/min up to 1000 °C and the partial pressure evolution of selected species were followed by the RGA. The TDS spectra are reported as a function of the measured temperature of the sample holder and after subtracting the background measured during a blank run.

**Optical Profilometry** In order to investigate the surface and quantify the surface roughness of the samples, optical profilometry was carried out at magnifications of 5x and 20x on a Veeco NT9100 Wyko optical profilometer. The measurements on the samples used in the reference activation were taken at approximately the same location on the sample before and after the reference activation.

**Endoscopy** In order to assess the quality, as well as identify any potential damage or alteration of the coating on the test pipes themselves as a result of the experiments, contactless endoscopy was performed with a GE XL Go+ VideoProbe portable video camera moved by a slide rail along the full length of the test pipes.

## 3.6 Simulation Methods

### 3.6.1 Phase Diagram Calculations

In order to determine the thermodynamically stable phases in the Ti-Zr-V system, ternary phase diagram calculations were performed in Thermo-Calc 2022a Software using the TCTI2: Ti-Alloys database version 2.2 [62].

### 3.6.2 Secondary Electron Yield Probe Depth Estimation

In order to complement the SEY measurements with electron penetration depth estimations, Monte Carlo electron trajectory simulations were carried out with

CASINO software version 2.5.1.0 [63]. Simulations were done on a multilayer structure of  $\text{Ti}_{31}\text{Zr}_{18}\text{V}_{52}$  1000 nm on top of a 304L stainless steel substrate with simulated composition of  $\text{Fe}_{68.97}\text{Ni}_8\text{Si}_1\text{Mn}_2\text{Cr}_{20}\text{C}_{0.03}$  at incident electron energies of 100–2000 eV in a step of 100 eV, with 200000 electrons used for the simulation. The penetration depth was taken as the maximum penetration depth of the incident electrons in the  $z$  direction.

#### 3.6.3 Vacuum Simulations

Test particle Monte Carlo simulations were performed in Molflow+ software version 2.8.6 [64–66] which simulate static pressure distributions in ultrahigh vacuum systems that are characterized by the molecular flow regime. Test bench 2 was reproduced and used for simulations as shown in fig. 3.7 to establish a relationship between the transmission ratio  $\frac{p_{ECG-2}}{p_{ECG-3}}$ , an output of the simulation, and the sticking coefficient of the TiZrV coated pipe walls, with different values of which different simulations were run until convergence. The obtained transfer curve is presented in fig. 3.8. Additionally, a transfer curve shown in fig. 3.9 was also obtained to establish the relationship between the sticking coefficient and the capture probability ( $CP$ ), calculated as  $CP = C_{1 \text{ cm diameter conductance}} \cdot \left( \frac{p_{ECG-2}}{p_{ECG-3}} - 1 \right) \cdot \frac{1}{C_{\text{test pipe entrance}}}$  [67].

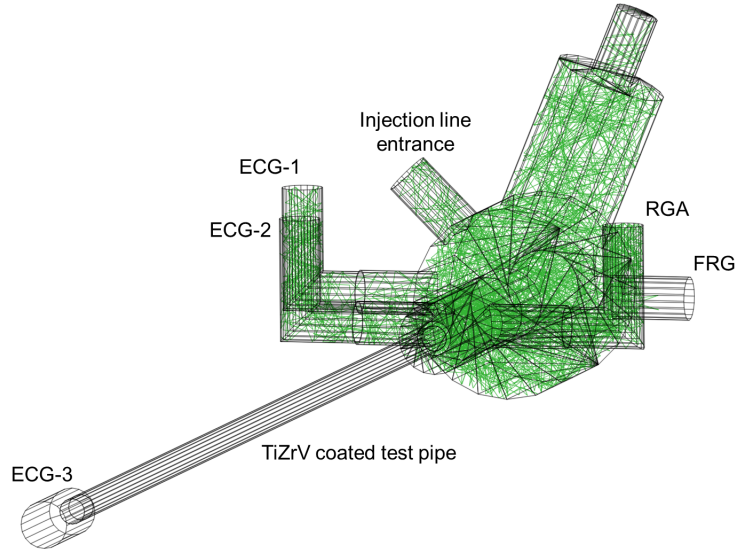


**Figure 3.7:** Geometry of the test bench used for the low pressure experiments as recreated in Molflow+ with green lines tracking the path of simulated gas particles

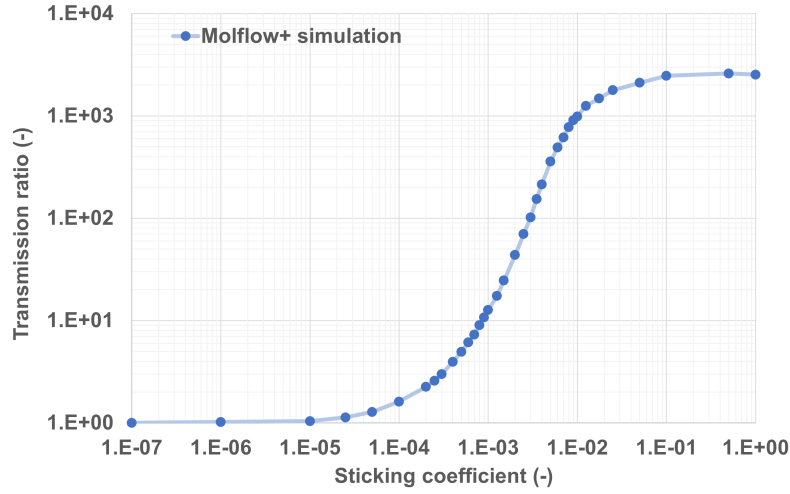


**Figure 3.8:** Transfer curve for the transmission ratio and the sticking coefficient obtained by Molflow+ simulations on the Test bench 2 geometry

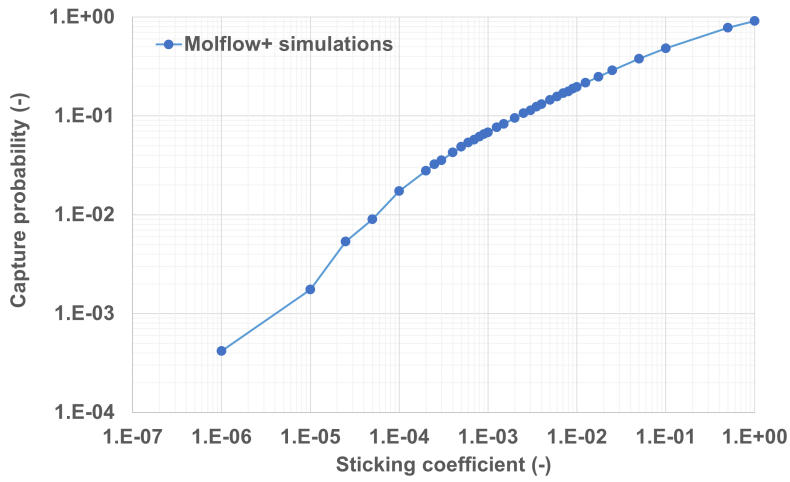


**Figure 3.9:** Transfer curve for the capture probability and the sticking coefficient obtained by Molflow+ simulations on the Test bench 2 geometry

### 3.7 Overview of Sample Characterization Matrix

The TiZrV NEG coating was characterized by characterizing witness samples at different stages of the experimental campaigns. To conclude this chapter, an overview of the different type of samples and the characterization methods carried out on them is provided in table 3.2 for both the HP and the LP experiments.

As presented in section 3.5, the TiZrV coating was characterized by various bulk, surface, and through-thickness measurements. The bulk composition and layer thickness was characterized by XRF and cross-validated by cross-section FIB imaging. The coating was characterized also for its surface composition both in

### 3. MATERIALS AND METHODS

---

as-received condition and after in-situ activations (XPS), as well as for secondary electron yield (SEY) to study the process and effectiveness of activation in the samples. Additionally, the surface topology and surface roughness was also analyzed by SEM and optical profilometry. The desorption of gaseous species from the samples was studied by TDS.

From the HP experiments, as-deposited (HP-0), activated reference samples (HP-0A), and witness samples subjected to various number of cycles were characterized. From the LP experiments, similarly, as-deposited (LP-0), activated reference samples (LP-0A), and witness samples subjected to the low pressure injection campaign (LP-1) have been characterized. In all cases, the coating thickness and composition was confirmed individually for all witness samples. Additionally, the bare witness sample substrate has been characterized as well.

sample	XRF	FIB SEM	Top SEM	Profilometry	XPS	SEY	XRD	TDS
substrate	-	-	✓	✓	-	-	-	✓
HP-0	✓	✓	✓	✓	✓	✓	✓	✓
HP-0A	✓	-	✓	✓	-	✓	-	-
HP-1	✓	-	✓	-	✓	✓	-	✓
HP-2	✓	-	✓	-	✓	✓	-	✓
HP-3	✓	-	✓	-	✓	✓	-	✓
HP-4	✓	-	✓	-	✓	✓	-	✓
HP-5	✓	-	✓	-	✓	✓	-	✓
HP-6	✓	-	✓	-	✓	✓	-	✓
LP-0	✓	✓	✓	✓	✓	✓	-	-
LP-0A	✓	-	✓	✓	✓	✓	-	-
LP-1	✓	-	✓	-	✓	✓	-	-

**Table 3.2:** Witness sample characterization matrix for the high pressure (HP) and the low pressure (LP) experiments, with “-0” referring to as-deposited samples, “-0A” referring to activated reference samples, else witness samples subjected to the ascribed number of cycles



## Chapter 4

# Results and Discussion

In this chapter the results are presented along with interpretation firstly of the characterization of the as-deposited as well as the reference activated samples in section 4.1, followed by the results from the high pressure (HP) experiment in section 4.2, after which the results from the low pressure (LP) experiments are discussed in section 4.3. The results together with final remarks, highlighting the achievements of this work and proposing suggestions for future studies are summarized in chapter 5.

### 4.1 As-deposited and Reference Activated Sample Characterization

The average thickness and composition of the as-deposited coatings are tabulated in table 4.1 as measured by X-ray fluorescence spectroscopy (XRF). These values were obtained by measuring a minimum of three witness samples that were placed both above and below the test pipe in the adjacent supporting pipes during deposition, for both deposition runs (amounting to a minimum of 12 as-deposited witness samples measured with XRF). The standard deviation of the coating thickness is related to the deposition specifications; the local distance between the cathode wire and the substrate surface, as well as the local pressure along the test pipe during deposition by magnetron sputtering are key factors determining the deposited film thickness [68, 69]. Accordingly, the variations are attributed to the shape of the witness samples deviating from being perfectly round from their front view, deviations in the axial centering of the vertically suspended cathode wire, and possible pressure fluctuations or a pressure gradient along the pipe assembly during the magnetron sputtering deposition process.

Four as-deposited witness samples –witness samples placed both above and below the test pipe during deposition, from the two deposition runs each– were subjected to focused ion beam (FIB) imaging in their cross-section (see fig. 4.1) to cross-validate the results of the XRF measurements. Although the thickness of these samples were observed to be at the far end of the measured thickness distribution, the measured thickness values were found to be in 10 % agreement, while the composition

#### 4. RESULTS AND DISCUSSION

measurement with XRF and energy dispersive X-ray spectroscopy (EDX) in the FIB set-up was found to be in  $<6\%$  agreement. This difference is related to the fact that the FIB measurement yields highly localized information, while the XRF measurement probes a much larger area of the coating, resulting in more representative results.

	Thickness ( $\mu\text{m}$ )	Composition (at %)		
		Ti	Zr	V
<b>NEG1</b>	$1.4 \pm 0.4$	33.2	19.0	47.8
<b>NEG2</b>	$1.0 \pm 0.4$	29.0	16.4	54.6

**Table 4.1:** TiZrV coating thickness and composition as determined from witness samples for the two test pipes by XRF (with NEG1 used in the low pressure, and NEG2 used in the high pressure experiment)

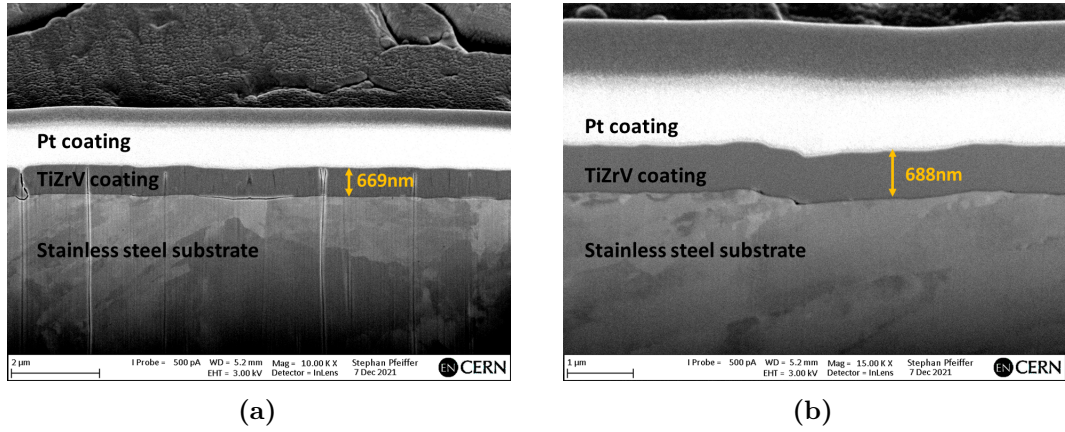


**Figure 4.1:** FIB imaging of the cross-section of the as-deposited TiZrV coating used in the high pressure (a) and low pressure (b) experiment

The top surface of the coating was also characterized by scanning electron microscopy (SEM). As shown in fig. 4.2, the deposited TiZrV layer displays larger ( $>10\mu\text{m}$ ) and smaller ( $\sim 0.5\mu\text{m}$  and  $<40\mu\text{m}$ ) surface features (see fig. 4.2b, and also fig. 4.5c), which are observed also on the bare stainless steel substrate (fig. 4.2a). This is a consequence of the line-of-sight deposition during the magnetron sputtering deposition process; the sputtered atoms follow and accentuate the surface roughness of the substrate. As a result, along the boundaries of the  $>10\mu\text{m}$  surface features, the TiZrV coating is observed to form grooves, which, based on other FIB micrographs such as the one shown in fig. A.4, might potentially extend through the whole thickness of the TiZrV coating. Such high aspect ratio surface features, as well as increased surface roughness of the getter coating in general has been reported to increase its sticking coefficient by creating geometrical traps for the gas particles to be sorbed with a higher probability by promoting an increased number of particle-wall collisions [2]. Higher surface roughness of the TiZrV coating can be achieved for

instance by applying higher substrate temperatures during the magnetron sputtering deposition process, such as 250 °C, as demonstrated by Chiggiato and Pinto [2]. However, a rougher TiZrV coating with higher surface area can lead to accelerated aging by the formation of a higher amount of native oxide during each venting. This trade off results in an optimal surface roughness of the getter coating which was found when it is deposited at 100 °C substrate temperature [2], also used as the substrate temperature during the depositions used in this work.

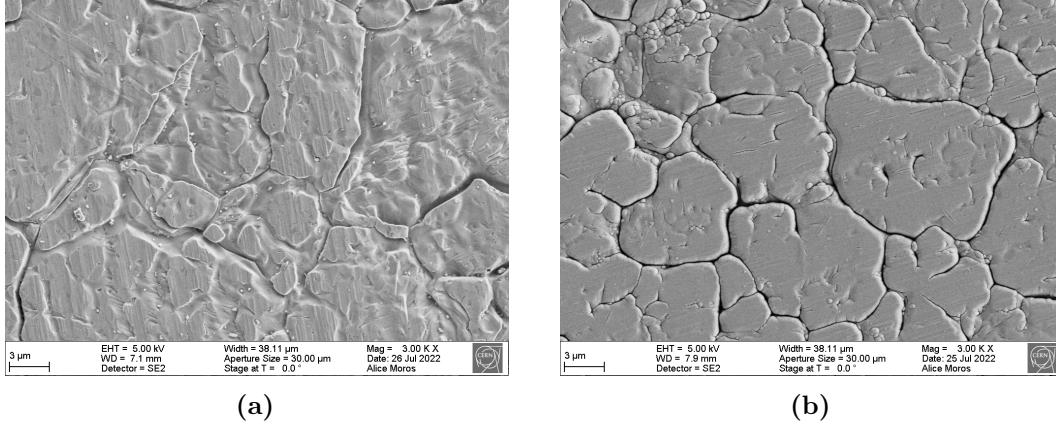


**Figure 4.2:** Top surface of the bare stainless steel substrate (a) and the as-deposited HP-0 sample (b) as imaged by SEM

At the composition of the NEG-1 coating, the equilibrium phase composition of the TiZrV alloy at standard temperature and pressure is 11.68 mol% body-centered cubic (bcc) phase ( $\text{Ti}_{0.005}\text{Zr}_{\sim 0}\text{V}_{0.995}$ ), 58.26 mol% Laves phase ( $\text{Ti}_{0.00009}\text{Zr}_{0.33327}\text{V}_{0.66664}$ ), and a 30.6 mol% hexagonal close-packed (hcp) phase ( $\text{Ti}_{0.9746}\text{Zr}_{0.02534}\text{V}_{5 \times 10^{-7}}$ ) (see fig. A.5), with the same phases being stable also at 100 °C (see fig. A.6). The presence of these immiscible phases in equilibrium combined with the limited diffusion kinetics during the sputtering deposition process is thought to be key in achieving an amorphous coating [4]. As already shown in fig. 4.1, grains could not be identified in the as-deposited TiZrV coating in its cross-section by FIB imaging. The X-ray diffraction (XRD) pattern of the TiZrV coating in fig. 4.3 shows a single and wide peak around 39.2° 2 $\theta$  which indicates that the material is amorphous, in accordance with previous reporting on the coating [4, 60]. The peak position at 39.2° 2 $\theta$  correlates with the estimated peak position of 39.6° 2 $\theta$  for a  $\text{Ti}_{0.3}\text{Zr}_{0.19}\text{V}_{0.51}$  coating [4]. As due to time, machine operation, and sample availability constraints, other samples could not be measured with XRD as part of this work, in fig. 4.4, results from the study of Pinto [60] is shared for comparison, where  $\text{Ti}_{0.28}\text{Zr}_{0.28}\text{V}_{0.44}$  coatings were measured with XRD in as-deposited condition, after 10 repeated cycles of activation and venting, and after a 240 h activation after the deposition but before venting, at different temperatures, to find a single amorphous peak in the as-deposited coating as well, and show that the material, as measured with XRD, was previously observed not to change during repeated activation-venting cycles up to 10 cycles at 230 °C activation temperature.

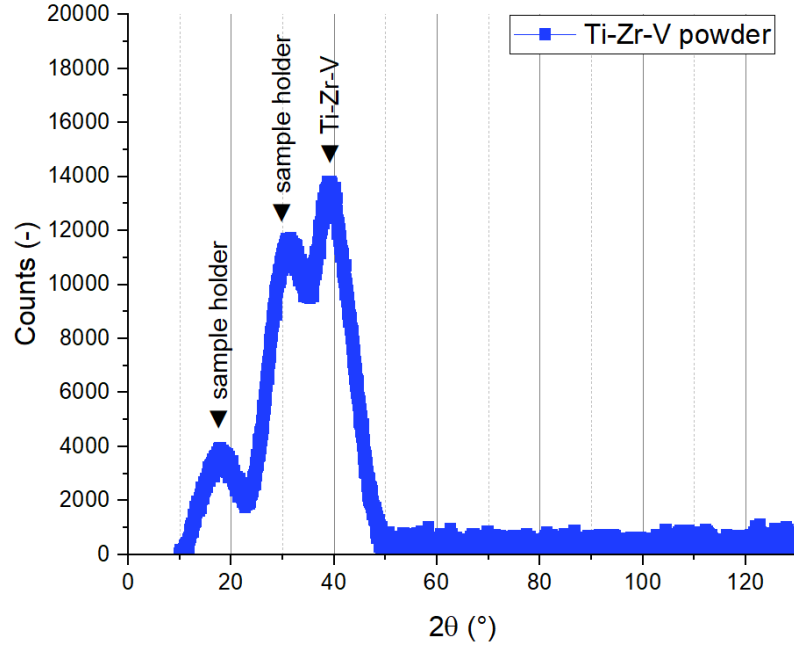


**Figure 4.3:** XRD pattern of the powdered TiZrV coating from an as-deposited HP-0 sample

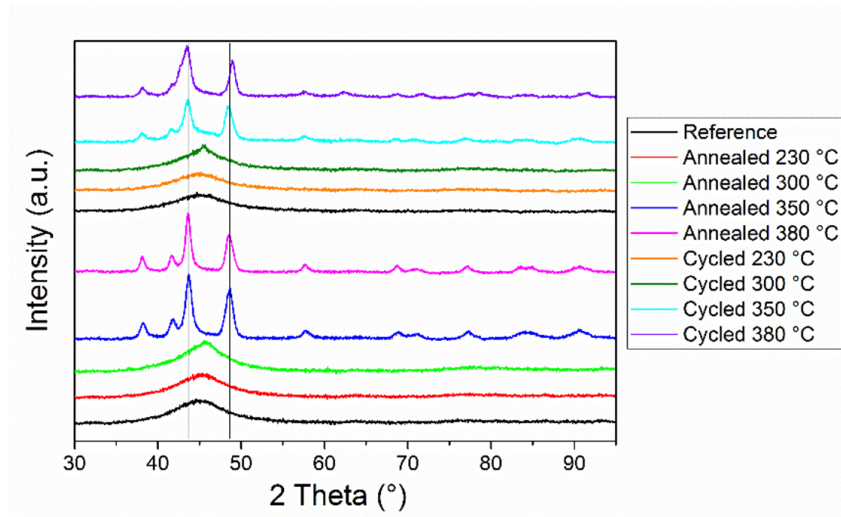


**Figure 4.4:** XRD patterns of  $\text{Ti}_{0.28}\text{Zr}_{0.28}\text{V}_{0.44}$  coatings after deposition (reference), after being subjected to 10 repeated venting-activation cycles at different temperatures (“cycled”), and after a 240 h anneal before venting and after deposition at different temperatures (“annealed”) [60]

#### 4.1.1 Reference Activation

The results from as-deposited HP and LP samples undergoing the reference activation cycle to study the effect of activation without  $H_2$  injection are presented here. Firstly, the effect of activation on the surface topology of the samples are shown. The surface topology of the samples was compared before and after the reference activation at various magnifications by SEM imaging, and micrographs at high magnifications are shown in fig. 4.5. Based on the micrographs, no substantial change is observed in surface topology and morphology for neither of the samples as a result of the reference activation. In table 4.2,  $R_q$  root mean square surface roughness values are shown of the bare substrate, the as-deposited TiZrV coatings, and the coatings after the reference activation, which were measured at two magnifications with optical profilometry, however, due to machine operation time constraints, only at one specific location per sample, which was indicated with a scratch. The surface roughness measurements show that the roughness of the as-deposited coatings of both HP-0 and LP-0 samples originate from the initial roughness of the stainless steel substrate. Furthermore, the surface roughness of both the HP and LP samples present a 25–29 % increase after activation. This could indicate that the activation results in the roughening of the surface, however, this was not observed by the qualitative assessment of the surface from SEM micrographs. It is concluded that in order to gain better confidence in the effect of activation on the surface roughness of the TiZrV coating, further measurements must be taken at several locations of the samples, and on a set of reference samples subjected to an increasing number of activations, which were not available in this study.

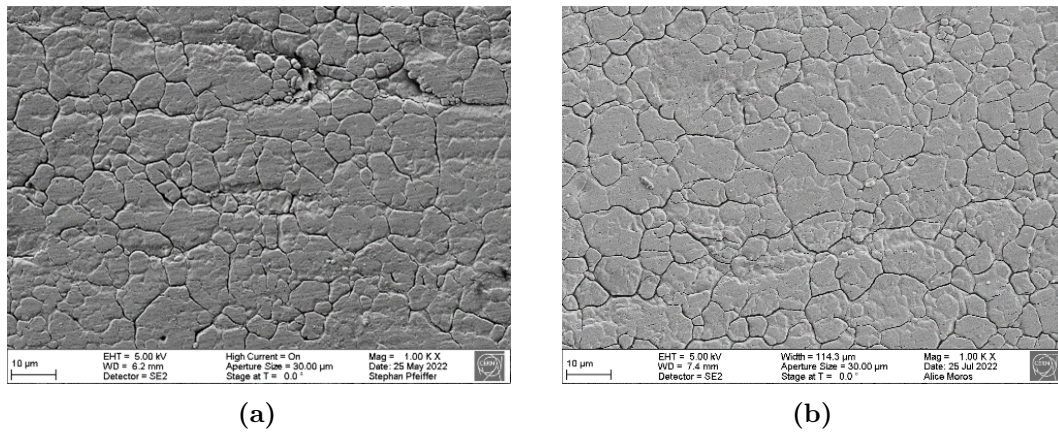


**Figure 4.5:** Top SEM images of the HP sample before (a) and after (b), and the LP sample before (c) and after (d) the reference activation

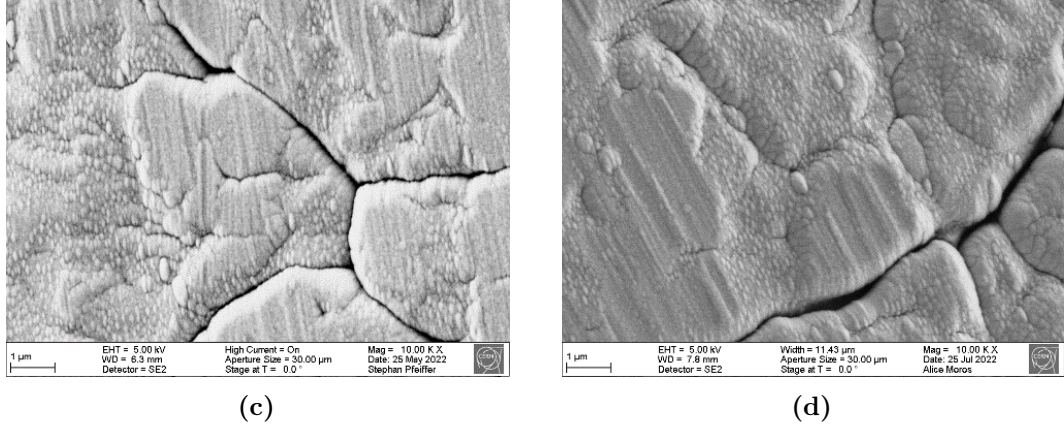


**Figure 4.5:** Top SEM images of the HP sample before (a) and after (b), and the LP sample before (c) and after (d) the reference activation (cont.)

	substrate	HP-0	HP-0A	LP-0	LP-0A
$R_q$ at 5 x	0.10 μm	0.10 μm	0.19 μm	0.10 μm	0.1 μm
$R_q$ at 20 x	0.17 μm	0.14 μm	0.18 μm	0.12 μm	0.15 μm

**Table 4.2:** Root mean square ( $R_q$ ) surface roughness of the substrate, the as-deposited (-0), and the reference activated (-0A) samples as measured by optical profilometry at two magnifications

## 4.2 High Pressure Experiment

The results of the high pressure experiment are shown in the following subsections. The high pressure experiment consisted of 6 consecutive cycles carried out on the NEG2 test pipe into which eight witness samples were also inserted before the start of the 1<sup>st</sup> cycle. A single high pressure cycle consisted of the sequence of mounting the test pipe to the test bench, bake-out and activation, sticking coefficient measurement, H<sub>2</sub> injection at the nominal pressure of 1 hPa, another sticking coefficient measurement, a second H<sub>2</sub> injection, reactivation, and another sticking coefficient measurement, after which the test pipe was vented to ambient air and dismounted from the test bench, the coating was visually inspected, and half of a witness sample was retrieved for materials characterization. The test pipe then was remounted to the test bench for the start of a new cycle. The composition of the vacuum was monitored with the residual gas analyzer (RGA) throughout the cycles when the pressures were sufficiently low for the operation of the secondary electron multiplier detector; the mass-to-charge spectra measured 24 h after reaching room temperature after the activations in each cycle are shown in fig. A.7, showing that the dominant gas in the vacuum after the bake-out and the activation is H<sub>2</sub> in accordance with the goal of the heating processes [18].

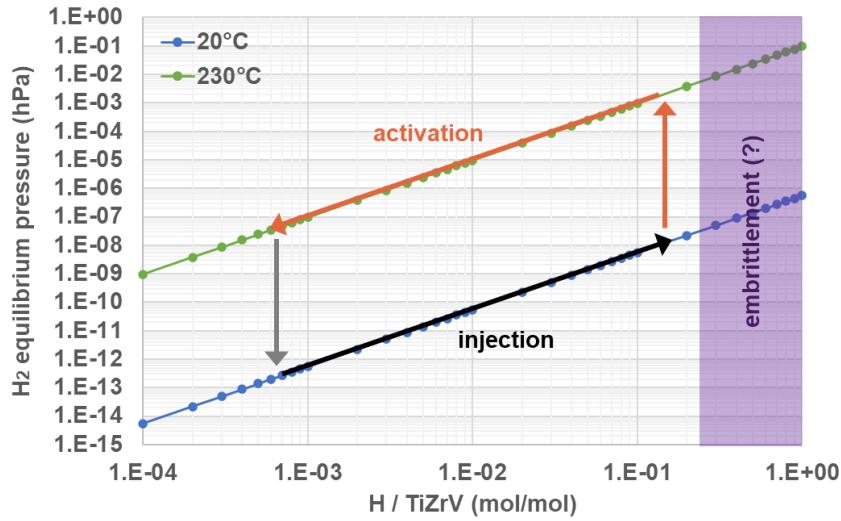


**Figure 4.6:** Calculated  $H_2$  equilibrium pressure as a function of  $H / TiZrV$  hydrogen fraction in the  $TiZrV$  coating at  $20^\circ C$  and  $230^\circ C$  [2], with potential hydrogen fraction region of embrittlement indicated with a rectangle. The hydrogen sorption process at room temperature (in black) and the hydrogen release process during (re)activation (in orange) are schematically indicated with arrows

To provide a theoretical reference for the thermodynamics of the hydrogen sorption and release processes during the high pressure cycles, the  $H_2$  equilibrium pressure ( $p_{H_2}$ ) is plotted in fig. 4.6 at the injection temperature ( $20^\circ C$ ) and at the (re)activation temperature ( $230^\circ C$ ) as a function of sorbed hydrogen quantity based on the measurements of Chiggiato and Pinto [2] where the Sievert's law for the  $H_2$  equilibrium pressure of the  $TiZrV$  film was evaluated as  $\ln p_{H_2} = 2 \ln x_H + 14.2 - \frac{8468}{T}$ , with  $x_H$  referring to  $H / TiZrV$  atomic hydrogen fraction in the coating. The  $H_2$  equilibrium pressure (also referred to as  $H_2$  dissociation pressure) associated with the concentration of hydrogen in the  $TiZrV$  coating in relation to the  $H_2$  partial pressure in the gas phase in contact with the coating determines the condition for the pumping of  $H_2$  by the coating; as long as the  $H_2$  equilibrium pressure is lower than the  $H_2$  partial pressure in the gas phase, there is a thermodynamic driving force for hydrogen sorption and the hydrogen concentration in the coating will increase until its associated  $H_2$  equilibrium pressure becomes equal with the  $H_2$  partial pressure in the gas phase, at which point the driving force for further hydrogen sorption becomes 0 [13]. Inversely, as exploited during (re)activation, in case of a lower  $H_2$  partial pressure in the gas phase in contact with the  $TiZrV$  coating than the  $H_2$  equilibrium pressure associated with the hydrogen concentration in the coating, there is a driving force for hydrogen to be released from the coating and its concentration to decrease, aided by the auxiliary pump continuously removing  $H_2$  from the gas phase during (re)activation. At higher hydrogen concentrations, hydrides are expected to form in the coating resulting in the embrittlement of the coating, indicated in fig. 4.6

with a rectangular area; for the schematic, a rectangle was chosen, however, the terminal solubility of hydrogen is expected to vary with temperature [39–41]. It has to be noted that typical evaluations of Sievert’s law are carried out at higher temperatures and by using small sorbed hydrogen quantities [70], meaning that the presented, extrapolated values might not be accurate for the TiZrV coating, especially since amorphous alloys are known to present deviations from Sievert’s law [37]. Regardless, fig. 4.6 provides a framework for the hydrogen sorption and release at the two characteristic temperatures of the cycles describing the principles behind hydrogen injection and the (re)activations.

### 4.2.1 Vacuum Results

The evolution of the sticking coefficient of the TiZrV coated test pipe over the HP experimental cycles is shown in fig. 4.7. The initial sticking coefficient was measured to be  $4 \times 10^{-3}$  after the activation in the 1<sup>st</sup> cycle. After the first 1 hPa H<sub>2</sub> injection, the value of the sticking coefficient is observed to decrease by an order of magnitude. This indicates that the sorbed H<sub>2</sub> has a strong impact on the sticking coefficient of the coating at the injected quantity. There are multiple mechanisms that can potentially explain the effect of the H<sub>2</sub> sorption on the H<sub>2</sub> sticking coefficient of the coating; as hydrogen takes up interstitial sites in the bulk of the material, the reduction of the number of available sites reduces the driving force for H<sub>2</sub> sorption [2]. The reduction of bulk sorption sites can also result in the decrease of the hydrogen diffusion rate in the coating [2, 44], which can impact the sticking of the surface by reducing the number of apparent available H<sub>2</sub> dissociation sites on the surface due to the lower rate of diffusion of the dissociated H atoms into the coating as a result of hydrogen absorption. It also cannot be excluded that the sorbed hydrogen quantity introduces modifications to the surface that reduce the sorption rate of the coating. In the 1<sup>st</sup> cycle, after the reactivation, the sticking coefficient is partially regained as H<sub>2</sub> is released from the coating during reactivation (see fig. 4.12 later). This trend can be observed in the rest of the cycles as well, emphasizing the relationship between sorbed H<sub>2</sub> quantity and the sticking coefficient. Furthermore, the sticking coefficient after the 2<sup>nd</sup> cycle activation is measured to be statistically equal to the sticking coefficient measured at the end of the 1<sup>st</sup> cycle (“reactivation”), indicating that the native oxide formed during the venting and dissolved during the 2<sup>nd</sup> cycle activation did not impact the H<sub>2</sub> sticking coefficient of the coating. Another important observation to be made is that after the 1<sup>st</sup> cycle, the maximum sticking coefficient attainable is limited to  $\sim 1 \times 10^{-3}$ . This is proposed to be related to the limitation of H<sub>2</sub> removal imposed by the evacuation rate of the auxiliary pump, as described more in detail when the pressure evolution curves are discussed. An additional factor that can also contribute to the limiting of the H release during the (re)activations, and consequently also the maximum sticking coefficient observed to be achievable after the 1<sup>st</sup> cycle, is the chemical composition of the surface. As presented later when the X-ray photoelectron spectroscopy (XPS) results are discussed in section 4.2.3, the ability of the TiZrV coating to dissolve C from its surface was observed to be marginal even in the case of the as-deposited sample, and as the venting to ambient

air between the cycles introduces not only O but also C to the surface (primarily from CO<sub>2</sub>, as well as hydrocarbons), this also could be a contributing factor to the observed limitation of the maximum sticking coefficient after the 1<sup>st</sup> cycle.

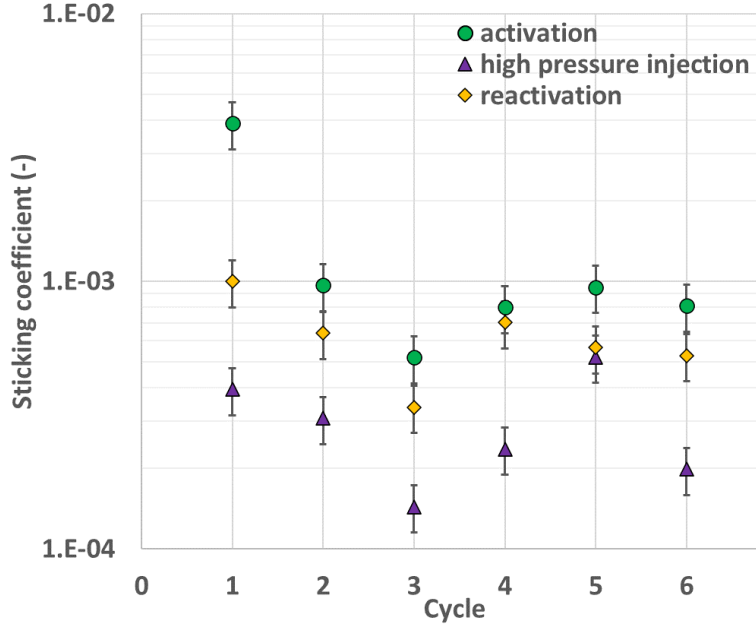


**Figure 4.7:** Sticking coefficient evolution over the high pressure experimental cycles showing measured sticking coefficient values after the activation (“activation”), after the first high pressure H<sub>2</sub> injection (“high pressure injection”), and after the reactivation (“reactivation”) in each cycle

The evolution of the ultimate pressure throughout the high pressure cycles is shown in fig. 4.8. The ultimate pressure in the system is generally expected to correlate with the sticking factor of the getter coating, since a higher sticking factor is related to a higher pumping speed of the getter, resulting in a lower ultimate pressure value. Indeed, in all cycles a clear distinction can be made between the ultimate pressure after the (re)activations, and after the first 1 hPa H<sub>2</sub> injections, the latter being higher also in accordance with the sticking coefficient results. The highest ultimate pressure is observed in the 1<sup>st</sup> cycle after the first 1 hPa H<sub>2</sub> injection; this might indicate that the hydrogen content in the TiZrV coating was the highest at that measurement point, however, especially in view of this point not coinciding with the lowest measured sticking coefficient in fig. 4.7, it can also indicate a change in the rate of hydrogen release from the coating after the 1<sup>st</sup> cycle, which can be related to the air venting condition first applied after the 1<sup>st</sup> cycle.

To further analyze the trends in the high pressure experimental cycles, the pump down curves of the TiZrV coating in static vacuum right after the termination of the H<sub>2</sub> injection are shown in fig. 4.9. The pump down curves show a clear trend in every cycle between the first and the second 1 hPa H<sub>2</sub> injection; in all cycles, it takes more time for the TiZrV coating during the second injection to pump the injected H<sub>2</sub>

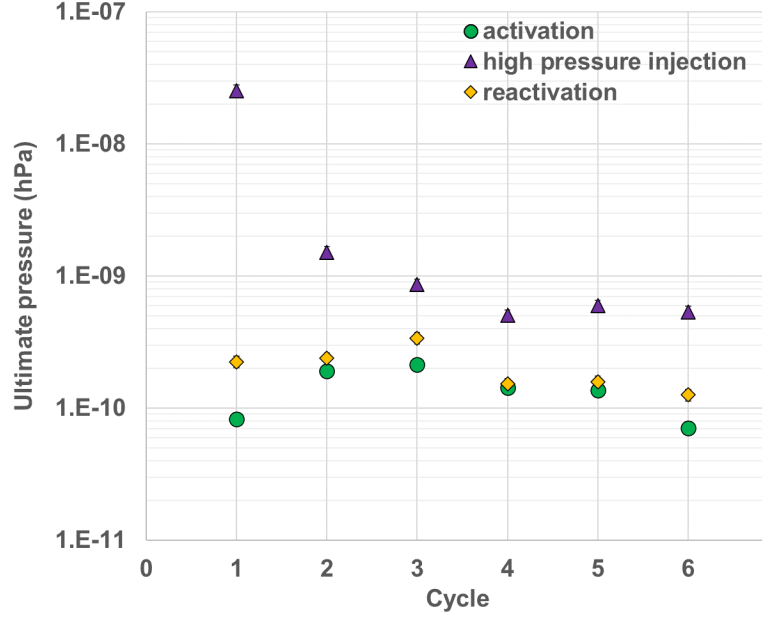
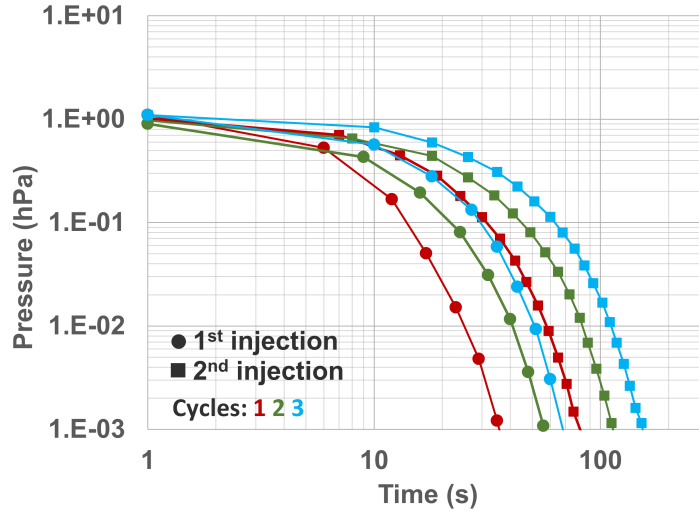


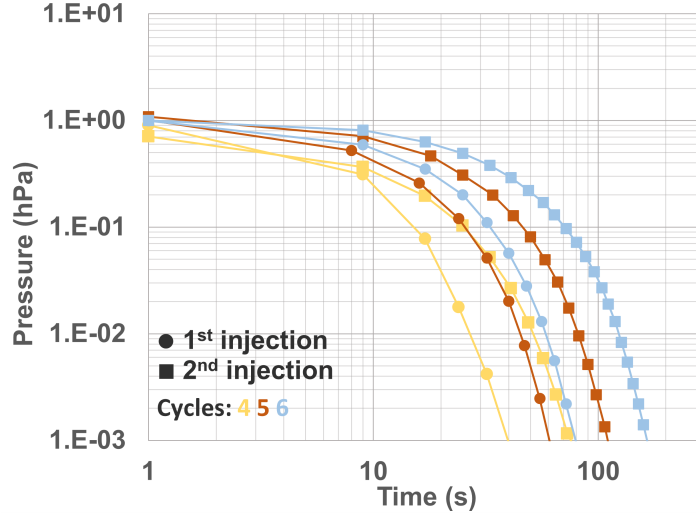
**Figure 4.8:** The ultimate pressure evolution over the high pressure experimental cycles showing the ultimate pressure after the activation (“activation”), after the first high pressure  $H_2$  injection (“high pressure injection”), and after the reactivation (“reactivation”) in each cycle

until a pressure below  $1 \times 10^{-3}$  hPa is reached, than during the first injection. The pressure in static vacuum was also measured with the ECG-2 gauge and was observed to reach a plateau around  $1 \times 10^{-4}$  hPa in all cases after 2 h of pumping, with no clear trend between the cycles. Given the purity of the  $H_2$  gas source (99.9997%), in  $1 \text{ hPa dm}^3$  injected, at least  $3 \times 10^{-6} \text{ hPa dm}^3$  is impurity, however that is only 3 % of the gas that remained in the system after 2 h of pumping. This is probably due to the TiZrV pumping speed becoming increasingly low at that point of the experiment. Regardless, the pressures measured 2 h after the injection in static vacuum confirm that 99.99 % of the injected  $H_2$  was absorbed by the coating.

The pump down curves are observed to follow an exponential decay shape and contain information about the sorption rate of the coating which is defined by the rate limiting step in the sorption process. However, the shape of the pump down curves is impacted by multiple factors during this experiment: gas flow regime transition, progressive pumping speed decrease of the coating during pumping, as well as the dynamic response of the active capacitance gauge (ACG) pressure gauge. Although without an exact physical model for the sorption process, further conclusions are difficult to draw from these curves, overall, the  $H_2$  sorption rate is observed to correlate with the absorbed hydrogen quantity; in every cycle, the sorption rate is lower during the second injection than during the first one. This trend indicates that the  $H_2$  sorption during the first injection reduces the  $H_2$  sorption rate during the second injection.



(a)



(b)

**Figure 4.9:** Pressure evolution in static vacuum after the 1 hPa  $H_2$  injections in cycle 1-3 (a) and 4-6 (b)

The pressure evolution curves during the activation heating processes of the high pressure cycles are shown in fig. 4.10 where the 10 h mark corresponds to reaching the  $230^\circ\text{C}$  activation temperature. Additionally, fig. 4.11 shows the ramp up part of the activations for further analysis. During the activation of the 1<sup>st</sup> cycle, the pressure is observed to increase in the system as the TiZrV coated test pipe is heated from  $120^\circ\text{C}$  up to around  $180\text{--}200^\circ\text{C}$ , after which point the pressure starts to decrease and reaches a pressure plateau with a significantly lower slope than initially after the  $180\text{--}200^\circ\text{C}$  pressure bump. The initial increase in pressure at the start of the

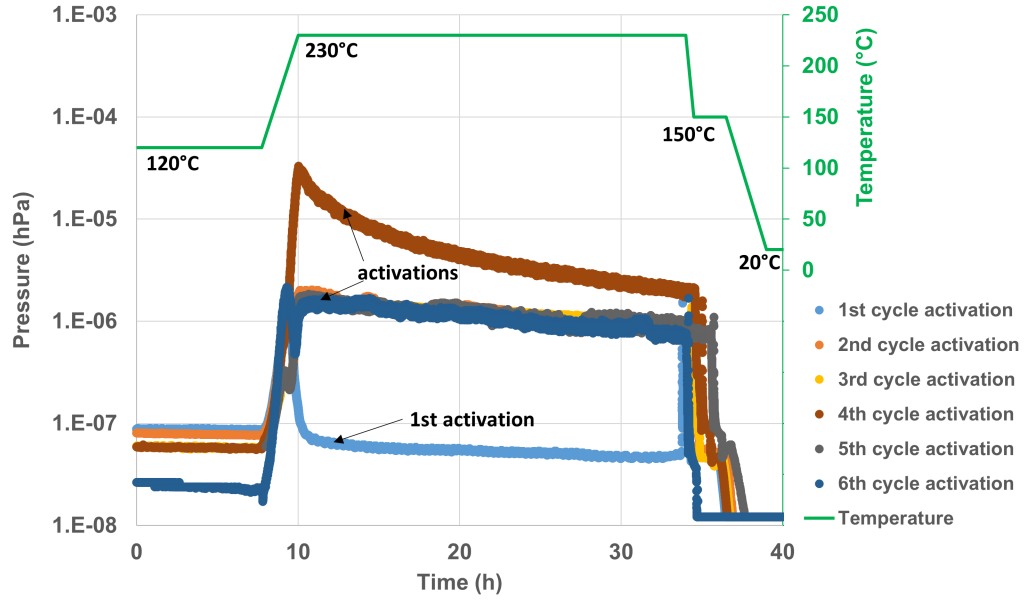


**Figure 4.10:** Pressure evolution during the high pressure experiment activations. The curves are arranged so that the 10 h mark notes the time of reaching the 230 °C activation temperature, and for reference, the temperature profile of the test pipe during activation is included as well

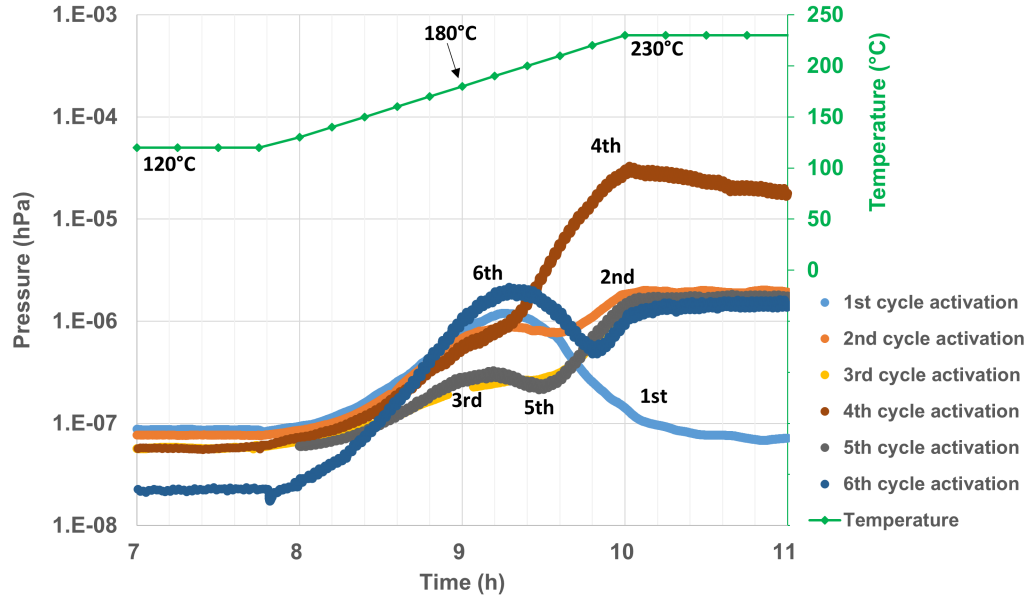


**Figure 4.11:** Pressure evolution during the high pressure experiment activations with focus on the ramp up. The curves are arranged so that the 10 h mark notes the time of reaching the 230 °C activation temperature and for reference, the temperature profile of the test pipe during activation is included as well

activation can be attributed to the further outgassing of adsorbed species (hydrocarbons and water molecules) from the top of the native oxide layer of the TiZrV coating. Depending on the venting and ambient conditions, the native oxide can be composed of several monolayers typically up to a thickness of 2 nm, and the adsorbed organic contamination on top of it can grow up to the same thickness, with an additional water adsorption on top extending it with further monolayers of water [33]. The pressure maximum at 180–200 °C marks the beginning of oxide dissolution [33]. As the native oxide dissolves, the surface of the TiZrV coating becomes metallic and available for sorption, resulting in a rapid pressure decrease in the system. The pressure on the plateau part of the activation pressure profile, an equilibrium between the outgassing rate from the TiZrV coating, and the sorption rate of the TiZrV coating, as well as the gas flow towards the auxiliary pump, is indicative of the residual hydrogen content in the TiZrV coating. Therefore, it can be concluded that there is more residual hydrogen in the coating after the activations in cycles 2–6 –and consequently, at all experimental points after the first high pressure hydrogen injection– than after the activation in the 1<sup>st</sup> cycle, which took place before any H<sub>2</sub> injection.

In the case of the activations in the other cycles, especially visible in fig. 4.11, the pressure maximum at 180–200 °C (at ~9.25 h in the plot) is only local, and after a temporary decrease in pressure, the pressure increases back to a higher value. This is interpreted to be related to the hydrogen release from the coating; after the start of the native oxide dissolution the kinetic limitation of hydrogen release is significantly reduced, and as the temperature is continuously increased, the driving force for hydrogen release is increased as well [2, 4]. The pressure in the cycles after the 1<sup>st</sup> cycle is at least an order of magnitude higher in all cases at the end of the activation, which indicates a higher residual hydrogen content remaining in the TiZrV coating after these activations. This indicates the limitations imposed by the pumping rate of the auxiliary pump; a significantly longer amount of time would be needed than 24 h at 230 °C in order to reach the plateau pressure observed in the 1<sup>st</sup> activation. From the activations, the activation pressure profile of the 4<sup>th</sup> cycle is a clear outlier, indicating much higher hydrogen release than in the other cases. Given the fact that this also correlates with a higher sticking coefficient in cycle 4 than cycle 3, this can be potentially attributed to an error in the activation temperature control set-up.

In order to be able to numerically compare the maximum pressures achieved at the activation temperature, as well as the “plateau pressures” referring to the pressure at the end of the 24 h activation, these values are tabulated in table 4.3. With the exception of the 4<sup>th</sup> cycle, an overall decreasing trend can be observed in the maximum pressures at 230 °C with increasing number of cycles, indicating decreasing hydrogen content in the TiZrV coating, or a progressively lower hydrogen release rate.

The pressure evolution during the reactivations together with that of the 1<sup>st</sup> cycle activation is shown in fig. 4.12. Here, the previously described behavior of the coating up to reaching the activation temperature is even more pronounced; as the TiZrV coated test pipe is heated, the pressure continuously increases until the 230 °C activation temperature is reached, after which it decreases, as hydrogen is

#### 4. RESULTS AND DISCUSSION

released from the coating and is pumped away by the auxiliary pump. Table 4.3 includes the maximum pressure and the plateau pressure values for the reactivation pressure profiles as well. The trend in the maximum pressures mimics that of the activations, and the plateau pressures arrive to an average value of  $2.45 \times 10^{-6}$  hPa. The maximum pressure during the activations is always lower than the plateau pressures at the end of the reactivation in the previous cycle, which underlines that the activations are the continuation of the reactivation in the previous cycle in terms of hydrogen release.

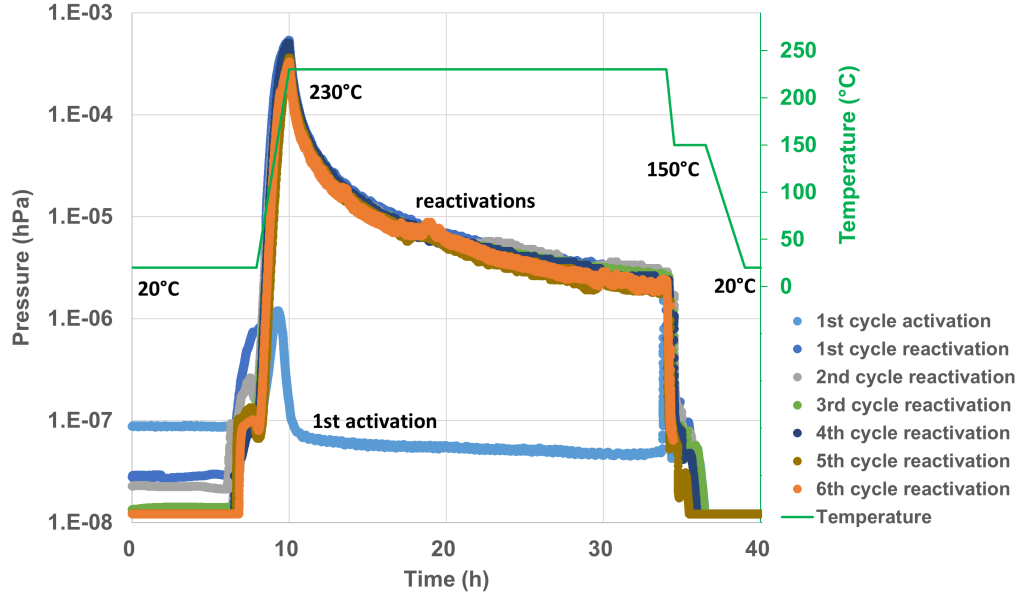
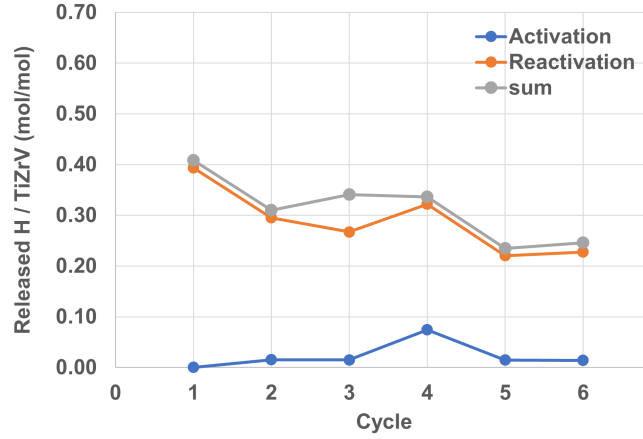


**Figure 4.12:** Pressure evolution during the high pressure experiment reactivations, with the 1<sup>st</sup> activation pressure profile as well for reference. The curves are arranged so that the 10 h mark notes the time of reaching the 230 °C activation temperature, and for reference, the temperature profile of the test pipe during reactivation is included as well

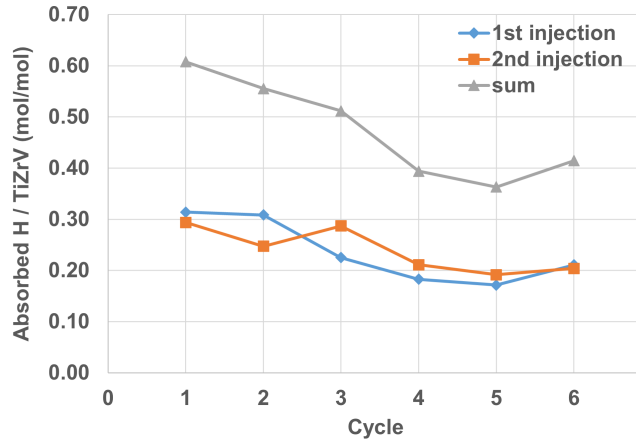
	Activation		Reactivation	
	$p_{\max}$ (hPa)	$p_{\text{plateau}}$ (hPa)	$p_{\max}$ (hPa)	$p_{\text{plateau}}$ (hPa)
<b>1<sup>st</sup> cycle</b>	$1.5 \times 10^{-6}$	$4.7 \times 10^{-8}$	$5.4 \times 10^{-4}$	$2.7 \times 10^{-6}$
<b>2<sup>nd</sup> cycle</b>	$2.0 \times 10^{-6}$	$8.8 \times 10^{-7}$	$4.1 \times 10^{-4}$	$2.8 \times 10^{-6}$
<b>3<sup>rd</sup> cycle</b>	$1.6 \times 10^{-6}$	$1.0 \times 10^{-6}$	$3.7 \times 10^{-4}$	$2.8 \times 10^{-6}$
<b>4<sup>th</sup> cycle</b>	$3.3 \times 10^{-5}$	$2.0 \times 10^{-6}$	$5.0 \times 10^{-4}$	$2.3 \times 10^{-6}$
<b>5<sup>th</sup> cycle</b>	$1.7 \times 10^{-6}$	$7.7 \times 10^{-7}$	$3.6 \times 10^{-4}$	$2.0 \times 10^{-6}$
<b>6<sup>th</sup> cycle</b>	$1.5 \times 10^{-6}$	$7.5 \times 10^{-7}$	$3.3 \times 10^{-4}$	$2.1 \times 10^{-6}$

**Table 4.3:** Pressure maxima ( $p_{\max}$ ) and plateau pressures ( $p_{\text{plateau}}$ ) of the activations and reactivations in the high pressure experiments

**Mass Balance** The absorbed and the released hydrogen quantities are here estimated to provide a mass balance for the cycles. The quantities are presented as H/TiZrV (mol/mol) fractions. The quantity of absorbing TiZrV was estimated through  $n = \frac{m}{M} = \frac{\rho \cdot V}{M}$ , where the density ( $\rho$ ) of the coating as well as its average molar mass ( $M$ ) was calculated from the rule of mixtures based on the average composition of the coating measured with XRF (yielding  $\rho_{\text{coating}} = 5.66 \text{ g/cm}^3$  and  $M_{\text{coating}} = 57.57 \text{ g/mol}$ ), and the coating volume was calculated using the internal surface area of the test pipe ( $2200 \text{ cm}^2$ ) and the average coating thickness measured by XRF on the witness samples, yielding  $0.02161 \text{ mol TiZrV}$  in the test pipe.



(a)



(b)

**Figure 4.13:** Mass balance of the experimental cycles as calculated from the (re)activation pressure (a) and the injection curves (b)

From the pressure profiles during the activations and the reactivations, by assuming that the total pressure is dominated by the  $\text{H}_2$  partial pressure, through eq. (8), the pressure curves were converted into outgassing rate curves ( $Q(t)$ ), the area under

which yields the total released  $H_2$  quantity (the double of which yields the released  $H$  quantity). The calculated released hydrogen quantities per high pressure injection cycle are shown in fig. 4.13a. A “sum” curve is also shown, which, at every cycle, is the sum of the calculated released hydrogen quantity during the reactivation in that cycle and the activation in the following cycle.

The minimum estimate of the absorbed hydrogen quantity was calculated as a first approximation via the ideal gas law in eq. (3) by substituting the maximum pressures during injection measured with the full-range gauge (FRG), the total volume of the test bench with the test pipe attached ( $25.45 \text{ dm}^3$ ), and  $293.15 \text{ K}$  for the temperature. The minimum estimation of the absorbed hydrogen quantity is then obtained as  $0.16 \text{ H/TiZrV (mol/mol)}$  per cycle. However, this is an underestimation of the injected hydrogen quantity, since the TiZrV coating sorbs  $H_2$  also during the ramp up of the pressure up to  $1 \text{ hPa}$  injection pressure, and also because the injections were not perfectly instantaneous given the manual operation of the injection. Using pumping speed values for the TiZrV coating calculated through  $S = \frac{V}{t} \cdot \ln \frac{p_0}{p_1}$  from the curves in fig. 4.9 to account for the sorbed hydrogen during the ramp up as well during injection, the injected hydrogen quantities were estimated as shown in fig. 4.13b.

A clear result from the mass balance calculations is that the TiZrV coating shows capacity to repeatedly absorb and release more than  $0.2 \text{ H/TiZrV (mol/mol)}$  hydrogen content, which is higher than the embrittlement limit –referring to an amount of sorbed hydrogen above which hydride formation is observed in the getter material, leading to its mechanical disintegration [20]– reported for other non-evaporable getters ( $\sim 26 \text{ hPa dm}^3/\text{g}$ , or  $\sim 0.15 \text{ H/NEG (mol/mol)}$  for St 707 and St 101 non-evaporable getters (NEGs)).

#### 4.2.2 Visual Inspection and Endoscopy

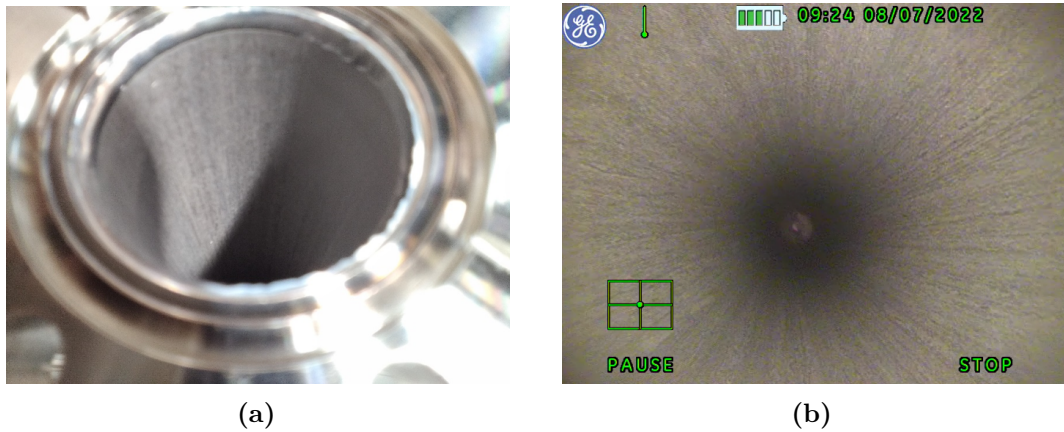


**Figure 4.14:** Perspective view of the TiZrV coating during the visual inspection (a) and the endoscopy (b) after the 6<sup>th</sup> high pressure cycle

After every cycle, the test pipe was visually inspected to look for macroscopically observable signs of embrittlement, peel off, powdering, or any alteration on the surface of the TiZrV coating. After the 3<sup>rd</sup> and the 6<sup>th</sup> cycle, an endoscopy was also performed along the full length of the test pipe, during which the coating was carefully inspected (see fig. 4.14). During these inspections, no sign of embrittlement was found on the coated test pipe, indicating that the six cycles of repeated H<sub>2</sub> sorption did not result in an alteration in the coating that would have led to its embrittlement under the imposed thermomechanical stress conditions, as well as due to the stress and strain accompanying the suggested volume expansion due to hydrogen absorption.

### 4.2.3 Materials Characterization

#### Surface Imaging

The witness sample surfaces were investigated by scanning electron microscopy at various magnifications, and selected micrographs are shown in fig. 4.15. Based on the micrographs, no apparent alteration on the top surface of the TiZrV coating could be identified as a function of the high pressure H<sub>2</sub> injections at high magnifications in terms of morphology. However, the witness samples did display peel-off and delamination from the substrate that was macroscopically visible and also visible on micrographs; at lower magnification, a representative example is shown in fig. 4.16, and in fact, similar delamination is also seen in both fig. 4.15a and fig. 4.15f. Similar flaking / peel-off was also observed on as-deposited samples that were bent and cut extensively. The witness sample handling, retrieval, reinsertion, and cutting, including the preparation of the witness samples for the SEM imaging, introduced mechanical stress by deforming the witness sample (bending and unbending), which can explain the coating delamination / peel-off. However, exactly for this reason, from these results, it cannot be concluded whether the coating has become mechanically

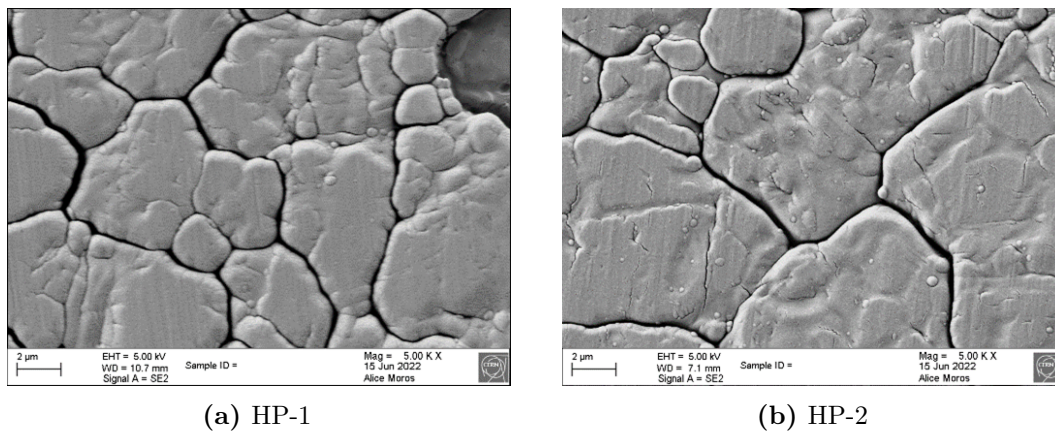
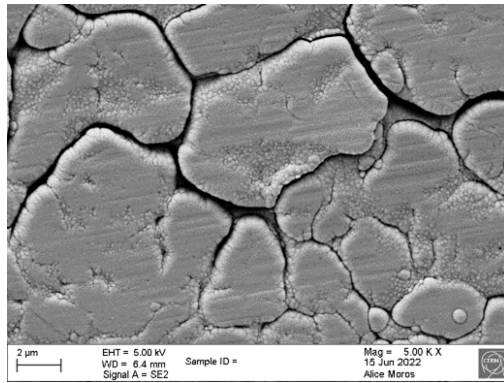
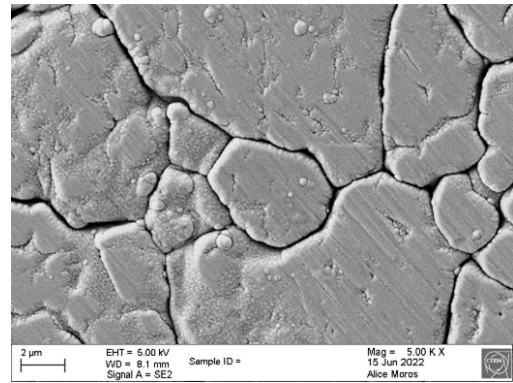


**Figure 4.15:** Top SEM images of the witness samples from the high pressure experiments

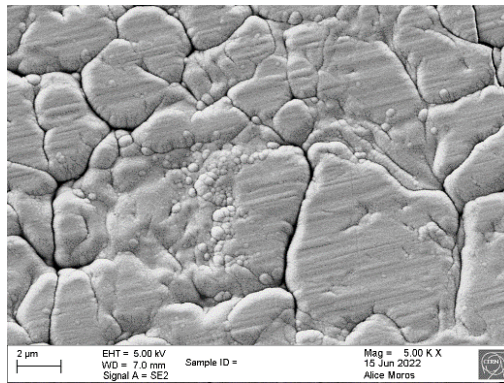
#### 4. RESULTS AND DISCUSSION



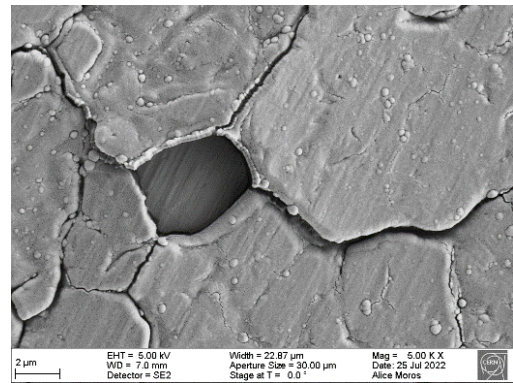
(c) HP-3



(d) HP-4



(e) HP-5



(f) HP-6

**Figure 4.15:** Top SEM images of the witness samples from the high pressure experiments (cont.)

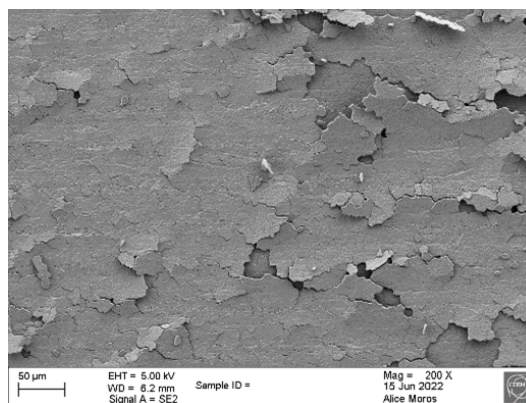


**Figure 4.16:** SEM image of the top surface of the HP-3 sample, showing representative peel-off of the witness samples as a result of witness sample handling (bending and unbending)

more brittle as a result of the  $H_2$  injections. To determine that, nanomechanical testing, for instance, carrying out scratch tests to determine coating adhesion at different experimental conditions [71] would be needed on identical samples not subjected to sample handling related mechanical stress, which were not produced as part of this study.

### X-ray Photoelectron Spectroscopy

XPS was deployed to study the top surface (3–5 nm) composition of the witness samples in their as-received condition, as well as after in-situ activation carried out in the XPS set-up. The as-received condition refers to measuring the witness samples after retrieving them at the end of an experimental cycle (or after deposition in the case of the as-deposited sample), and measuring them at room temperature in the XPS set-up, implying that in the as-received state, due to exposure to ambient air, the surface of the samples is covered by a native oxide and an adsorbed layer on top, consisting of hydrocarbons and water molecules [33]. The in-situ activation was carried out to study the effectiveness of activation by studying the change in the surface composition of the TiZrV coating as a result of the in-situ activation. The in-situ activation was carried out in three consecutive steps at three increasing temperatures (160 °C, 200 °C, and 250 °C) where the sample was kept for 1 h each, and XPS measurements were taken at the end of each temperature step. When results refer to in-situ activated sample condition without further specifying, the XPS measurement taken at the end of the last temperature step (250 °C) is being referred to. The base pressure during the measurements was  $2 \times 10^{-10}$  hPa at room temperature which increased up to a maximum of  $4 \times 10^{-9}$  hPa during the in-situ activations. The complete surface composition data calculated from the respective peak areas from the XPS spectra can be found in table A.5 and the reference spectral lines used for the analysis of the spectra are tabulated in table A.6.

The comparison of the relative surface composition of the samples in their as-received state and after the in-situ activation informs about the effectiveness of the activation, firstly shown through the evolution of the surface O and C content of the samples. The evolution throughout the in-situ activation of the measured O 1s peak areas normalized to the O 1s peak area measured in the as-received state of each sample is shown in fig. 4.17. The surface O content of the as-deposited HP-0 sample decreases by 71.2 % overall as a result of the in-situ activation (see also in table 4.4). This is in accordance with the expectation that above 180 °C, O dissolution and diffusion into the bulk of the coating is promoted [33], and also confirms the interpretation of the pressure evolution results during the activations in section 4.2.1, specifically shown in fig. 4.11. In fig. 4.17, the decrease of surface O content is also seen to be smaller for samples that were subjected to an increasing number of cycles, with the HP-6 sample having only 11.2 % surface O content decrease after the in-situ activation. At the activation temperature of 230 °C with 24 h duration used in the experiments of this work, due to kinetic limitations, O has been shown not to dissolve homogeneously into the layer, but to rather accumulate near the surface of the coating, creating a gradient that progressively reduces the efficiency of

activation by lowering the O diffusion rate near the surface as a result of repeated venting-activation cycles [60]. This is generally referred to as aging and is a known phenomenon of getters subjected to repeated venting-activation cycles. The extent of aging depends on several conditions, including the activation time and temperature and the atmosphere the coating is vented with [36]. The effect of aging can be exacerbated by the sorption of other elements that occupy sites the O occupies as well in the alloy, such as H, which, as seen from the vacuum results, is not fully removed from the coating between the cycles. These results showing the reduction of surface O content decrease during the in-situ activation are a combination of the effect of inhomogeneous O dissolution at the used activation time and temperature, and the residual H content in the coating, progressively decreasing the O dissolution rate into the layer under the same activation conditions.

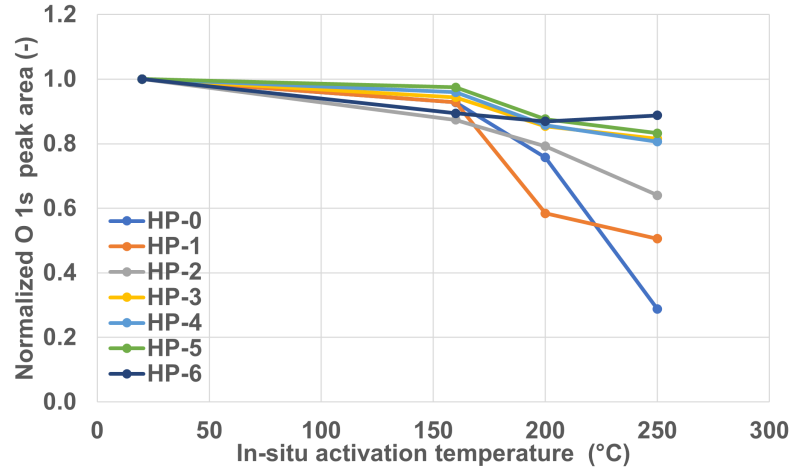


**Figure 4.17:** Evolution of the normalized O 1s peak area throughout the in-situ activations as measured with XPS

Further elaboration on aging by thermodynamic and kinetic considerations is provided here. The oxygen solubility limit in single crystal Ti and Zr at the temperature of activation is cited to be around 30 at%, and 3 at% for V [4] as also included in table A.1, and these values are potentially even higher in the nanocrystalline, or amorphous alloy. Furthermore, provided by the comparison of the heat of oxide formation and the heat of oxygen dissolution in pure metals by Prodromides in table A.2 [4], given the entropic term being negative at all temperatures, it can be concluded, that in pure Ti and Zr, oxygen dissolution is thermodynamically favored at all temperatures compared to oxide formation, up to the solubility limit of oxygen, and takes place when the kinetic limitations are lowered for oxygen diffusion as a result of the increased temperature during activation. The lack of oxygen dissolution and diffusion from the surface into the bulk of the coating is therefore attributed to the kinetic limitation of the diffusion of oxygen during activation. Previous XPS depth-profile measurements on the TiZrV coating have shown the formation of the oxygen gradient near the coating surface as a result

of repeated venting-activation cycles [60], and since the residual hydrogen content during activation is low compared to stoichiometric metal-hydrides (as the venting is preceded by the reactivation in the cycles), it is assumed that the same phenomenon occurs similarly in the samples presented in this work as well. XPS depth-profile measurements were assigned for witness samples from this work as well, however, at the time of writing, these results could not be analyzed and included in this work.

The chemical state of oxygen in all measurements in as-received condition was identified as O(-II), potentially primarily in a mixture metal-oxides based on the dominant O 1s peak position ( $\sim 530$  eV as shown in fig. A.8) which overlaps with the reference peaks in table A.6 of oxygen in  $\text{TiO}_2$ ,  $\text{ZrO}_2$ , and  $\text{V}_2\text{O}_5$ . However, further analysis was not performed on the O 1s spectra due to potentially low confidence interpretation owing to the fact that binding energies of many chemical states of oxygen overlap in the narrow region of 530–531 eV [57].

Figure 4.18 shows the evolution of the normalized C 1s peak area on the witness sample surfaces as a function of the in-situ activation temperature. From this figure, as well as from the C 1s peak area decrease values in table 4.4, it is seen that the surface C content does not decrease to the same extent as O as a result of the in-situ activations. Although the diffusion length at the in-situ activation temperatures is reported to be higher for C than for O in the single crystal elements of the constituents of the coating [4] (see also in fig. A.9), it is generally observed that the surface C content of TiZrV does not dissolve into the layer at  $230^\circ\text{C}$  as readily as O, but rather forms carbides with the alloying metals and remains on the surface of the sample [2, 33], potentially owing to both adventitious C contamination during the XPS measurement, and the lower solubility in the alloy of C than O, based on the solubility values in pure metals shown in table A.1. On this note, it has to be remarked that precise quantification of the C content on the surface is much more difficult than for O in XPS measurements, especially at low concentrations [33].

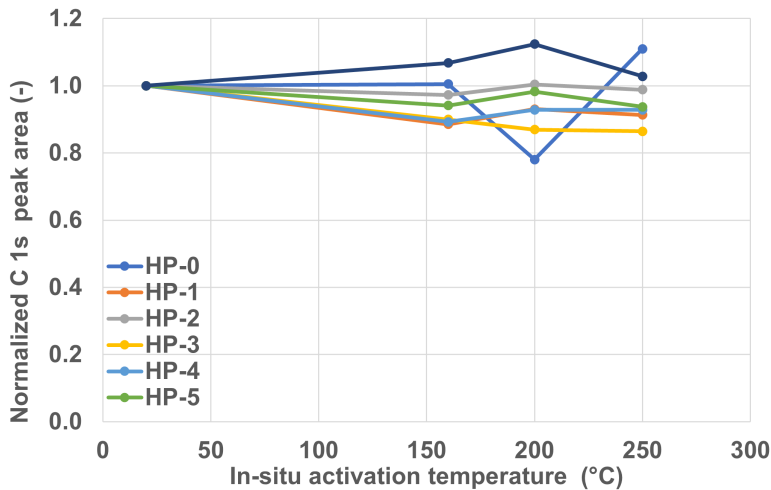


**Figure 4.18:** Evolution of the normalized C 1s peak area throughout the in-situ activations as measured with XPS

#### 4. RESULTS AND DISCUSSION

To analyze the chemical state of C on the sample surface, the C 1s peak of the witness samples is shown in fig. 4.19. In as-received condition, the main peak is observed around 284.5 eV with additional peaks at 288.5–288.3 eV and 282.3 eV. The  $\sim 284.5$  eV peak is identified as C(0) as in C–C bonds in hydrocarbons (see reference spectral lines in table A.6), while the peak at the higher binding energy (C in higher oxidation state) is identified as C in oxygenated form (as compared with for instance the O–C=O bond with 288.5 eV reference spectral line). The  $\sim 282.3$  eV peak is identified as C(-II) and relates to the reference spectral lines of C in carbides formed with Ti, Zr and V. Figure 4.19 shows that the C content on the sample surfaces in as-received condition consists primarily of adventitious carbon; hydrocarbons and oxygenated carbon-containing molecules adsorbed to the coating on top of the native oxide layer.

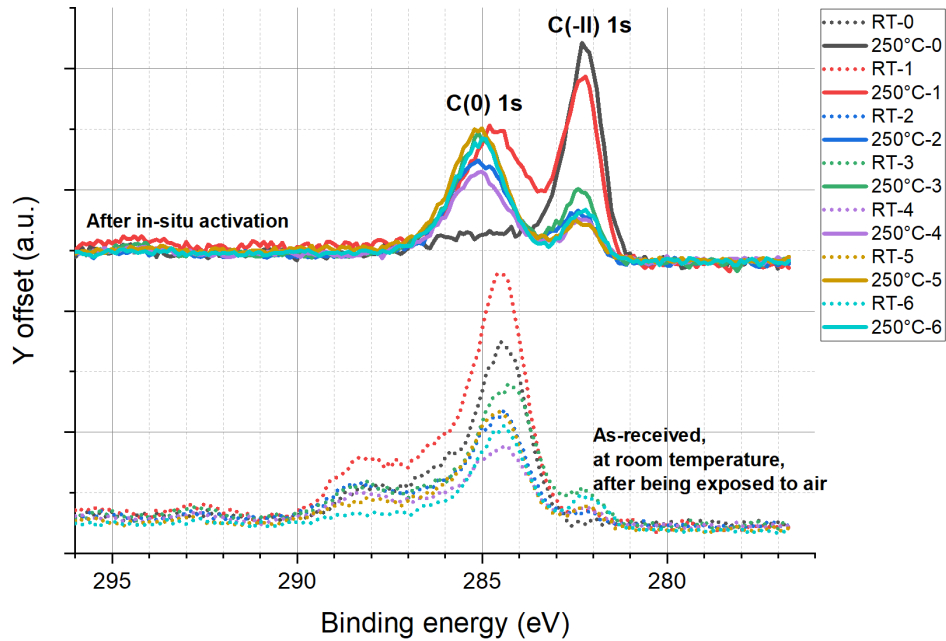


**Figure 4.19:** XPS spectra of the C 1s peaks of the witness samples in as-received condition and after the in-situ activation

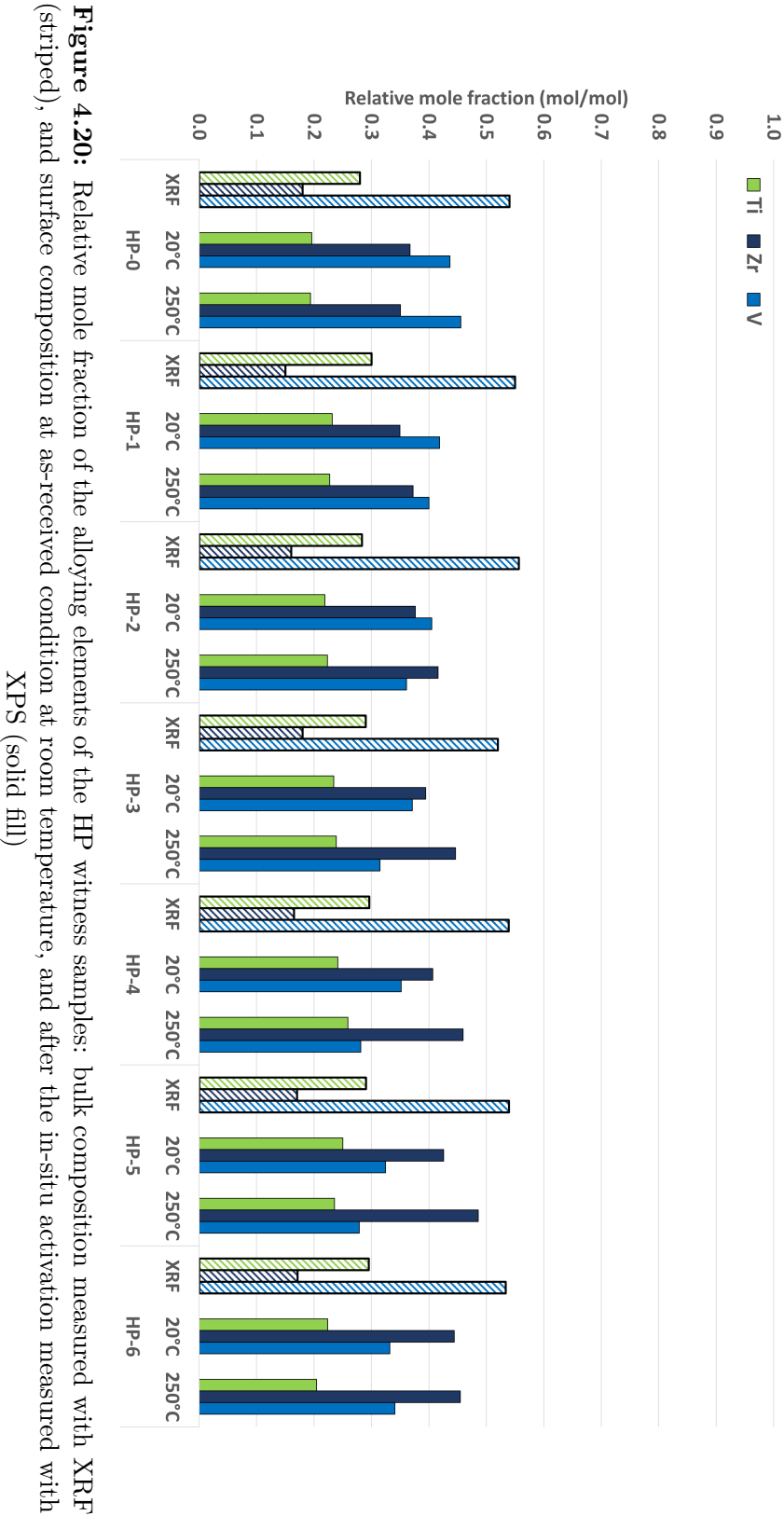
After the in-situ activation in the as-deposited HP-0, the C 1s XPS spectrum is dominated by the peak at  $\sim 282.3$  eV, which is identified as C(-II) in carbide, with the closest to the 282.2 eV reference spectral line of C 1s in VC. This shows that in the as-deposited sample, the adventitious carbon on the surface is to a large extent converted into carbide. The carbon-to-carbide conversion however shows a decreasing trend throughout the samples subjected to an increasing number of high pressure  $H_2$  injection cycles, visible from the inversion of the C(0) and C(-II) peak heights in fig. 4.19, as well as in the extracted carbide-to-total carbon content ratios on the sample surfaces after the in-situ activations as tabulated also in table 4.4, decreasing from 70.6 % in HP-0 to 17.4 % in HP-6. This is possibly correlated with

the observed reduction in O decrease from the surface throughout the cycles; as O remains on the surface, it potentially inhibits the carbon-to-carbide conversion as it preferentially binds to the alloying elements. The carbothermal reduction of the oxides is thermodynamically not substantiated at the in-situ activation temperature [72].

	$\Delta_{\text{O } 1s \text{ area}}$	$\Delta_{\text{C } 1s \text{ area}}$	$\Delta_{\text{Carbide} / \text{Total C}}$
<b>HP-0</b>	0.712	0.201	0.706
<b>HP-1</b>	0.494	0.258	0.424
<b>HP-2</b>	0.360	0.186	0.224
<b>HP-3</b>	0.184	0.225	0.261
<b>HP-4</b>	0.194	0.149	0.221
<b>HP-5</b>	0.168	0.144	0.174
<b>HP-6</b>	0.112	-0.041	0.174

**Table 4.4:** Relative surface oxygen content decrease as a result of activation ( $\Delta_{\text{O } 1s \text{ area}}$ ) calculated as the ratio of the O 1s peak area measured in as-received condition minus the O 1s peak area measured after the in-situ activation, divided by the O 1s peak area measured in as-received condition; relative surface carbon content decrease as a result of activation ( $\Delta_{\text{C } 1s \text{ area}}$ ) calculated as the ratio of the C 1s peak area measured in as-received condition minus the C 1s peak area measured after the in-situ activation, divided by the C 1s peak area measured in as-received condition; and carbon-to-carbide conversion ratio ( $\Delta_{\text{Carbide} / \text{Total C}}$ ) calculated as the carbide (C(-II) 1s) peak area divided by the total C 1s peak area after the in-situ activation

**Metal Content** Figure 4.20 shows the relative composition of the alloying elements in mole fraction as measured in the whole thickness of the coating with XRF, and on the sample surface (3–5 nm) as obtained with XPS in as-received condition (after air-exposure, at 20 °C), and at the end of the in-situ activation (after 1 h of being at the final 250 °C in-situ activation temperature). This comparison shows clearly that in all samples, including the as-deposited sample (HP-0), the Zr content on the surface is higher than in the bulk of the coating overall, at the expense of both Ti and V, but primarily V. This is attributed to the surface segregation of Zr in the alloy and has been reported on in literature previously [33]. The surface segregation of Zr is observed to become more pronounced as progressing in the cycles; activations (and reactivations) promote Zr diffusion to the surface clearly seen from the increasing Zr content as progressing in the cycles. This is attributed to Zr having the highest affinity to O from the alloying elements of the coating, highlighted later in the analysis of the XPS spectra of the metals as well.



The chemical state of the alloying elements analyzed by studying their respective XPS spectra are presented as follows. In the samples in as-received condition, the Ti content on the sample surface is almost exclusively present in oxidized state clearly seen from the position of the Ti 2p core levels of the two dominant (Ti 2p<sub>3/2</sub> and Ti 2p<sub>1/2</sub>) peaks of the spectra in fig. 4.21 identified as Ti(IV) corresponding to the reference spectral line of 458.8 eV for Ti 2p<sub>3/2</sub> in TiO<sub>2</sub>. A contribution just above the background level around 455 eV indicates that a negligible fraction of Ti is in a lower oxidation state, potentially metallic. From the results of the in-situ activations, a clear division presents between the samples. The Ti content of the surface of the as-deposited and HP-1 samples proves effectively reducible with the in-situ activation; the Ti 2p core levels shift towards lower binding energies indicating reduction of Ti(IV) to Ti(0) (with a reference peak of 454.1 eV for Ti 2p<sub>3/2</sub> in metallic Ti), with no indication of residual oxidized Ti content. Samples subjected to more than 1 HP cycles however present a mixture of peaks without a single and well-defined peak in either identified oxidation state after the in-situ activation, which indicates that in samples after the 1<sup>st</sup> high pressure H<sub>2</sub> injection cycle, Ti remains oxidized in a mixture of oxides and sub-oxides. The incomplete Ti reduction during the in-situ activation of samples after cycle 1 observed here naturally corresponds to the reduced O decrease from the surface of the samples as well.

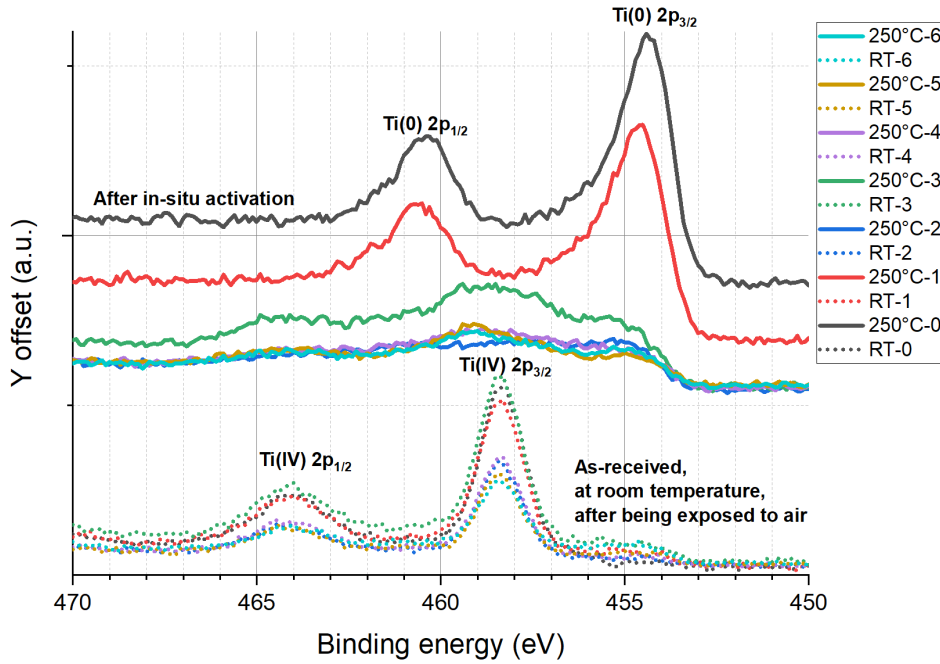


**Figure 4.21:** XPS spectra of the Ti 2p peaks of the witness samples in as-received condition and after the in-situ activation

Similarly, the surface Zr content of the samples in as-received condition is found predominantly in the oxidized state of Zr(IV) as shown in fig. 4.22 (with reference peak 182.2 eV for Zr 3d<sub>5/2</sub> in ZrO<sub>2</sub>), with a shoulder around 179 eV indicating the

presence of a small amount of Zr(0) as well (with reference peak of 178.9 eV for Zr 3d<sub>5/2</sub> in metallic Zr). After the in-situ activation, in the as-deposited HP-0 sample, the Zr content shows significant reduction; while the largely asymmetric shoulder of the Zr 3d<sub>3/2</sub> peak towards higher energies indicate that some surface Zr remains oxidized, from the position of the two dominant peaks (with reference peak of 179 eV for Zr 3d<sub>5/2</sub> in metallic Zr), it is determined that most Zr is effectively reduced during the activation of the HP-0 sample. However, in the samples subjected to the HP cycles, the surface Zr content after the in-situ activations remains primarily oxidized seen from the considerably small peak around 179 eV indicating reduction, while the spectra are dominated by the oxidized peaks (reference peak 182.2 eV for Zr 3d<sub>5/2</sub> in ZrO<sub>2</sub>), which are even shifted towards higher energies compared to prior to the in-situ activations. Out of the alloying constituents of the TiZrV layer, Zr has the highest affinity to oxygen [4], and therefore is expected to be reduced last when the complete reduction of the surface metals is limited.

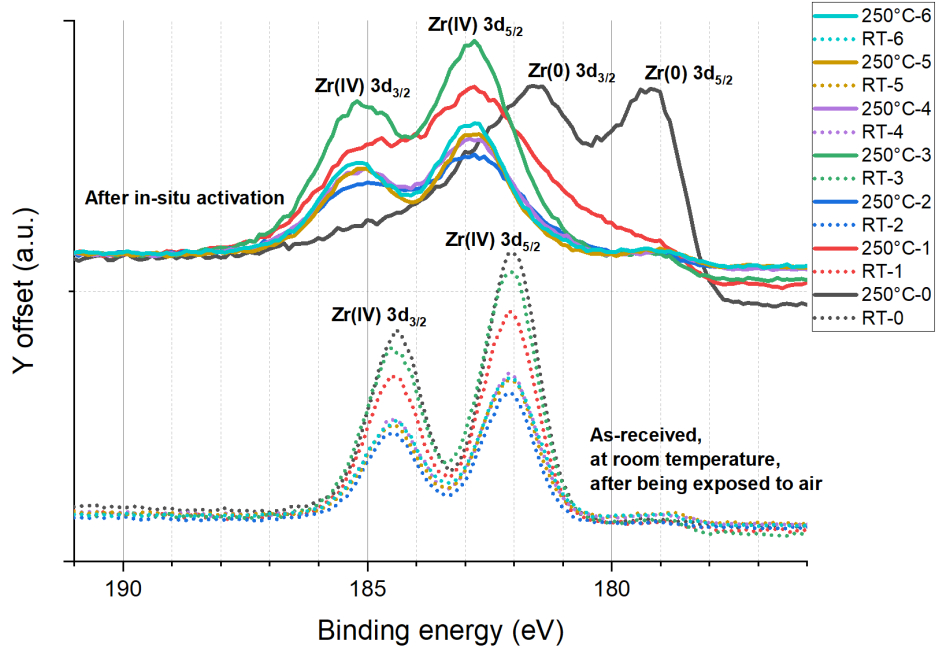


**Figure 4.22:** XPS spectra of the Zr 3d peaks of the witness samples in as-received condition and after the in-situ activation

The surface V content, similarly to the two other metals in the alloy, is identified to be primarily in oxidized state on the witness sample surface in as-received condition from the V 2p spectra in fig. 4.23. As V forms various oxides in multiple oxidation states in not strictly stoichiometric compositions with a large reported variation in V 2p spectral lines [73], an accurate determination of the oxidation state of V is limited here. The main V 2p<sub>3/2</sub> peak at 517 eV can be identified as V in oxidized state and was labeled as V(V) after comparison with the reference spectral lines (513 eV for V 2p<sub>3/2</sub> in VO, 515.7 eV for V 2p<sub>3/2</sub> in V<sub>2</sub>O<sub>3</sub>, 516.3 eV for V 2p<sub>3/2</sub> in VO<sub>2</sub>, and 517.4 eV

for V  $2p_{3/2}$  in  $V_2O_5$ ), however, the V content on the sample surface is most possibly in a combination of multiple oxidation states. The shoulder at 513 eV indicates that some V in the as-received condition is also in either V(0) or V(II) state, or a mix of them, where the V(II) can be V in VO.

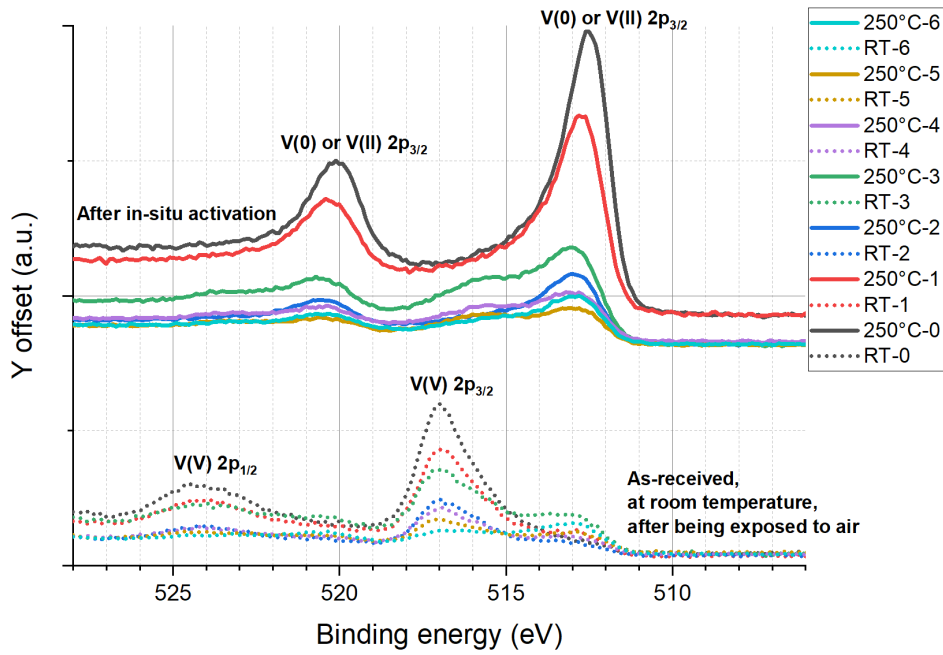


**Figure 4.23:** XPS spectra of the V 2p peaks of the witness samples in as-received condition and after the in-situ activation

As a result of the in-situ activation, the surface V content of the samples shows a clear indication of reduction to lower oxidation states as seen in the core level shift towards lower binding energies in fig. 4.23. In the as-deposited HP-0, as well as the HP-1 sample, the V  $2p_{3/2}$  peak around 512.5–512.8 eV dominates the spectrum indicating that V is in V(0) or V(II) oxidation state, or a mix of them (with reference spectral lines of 512.2 eV for V  $2p_{3/2}$  in metallic V and 513 eV for V  $2p_{3/2}$  in VO), which is a sign of significant reduction as a result of the in-situ activation. The extent of reduction shows a progressive decrease throughout the cycles; after HP-1, the V 2p spectra, similarly as seen in the case of Ti, show a mix of oxidation states without a clear oxidized or reduced peak, with the HP-6 sample having the least pronounced peaks, indicating progressively decreasing extent of reduction of surface V of the samples. Furthermore, as previously identified, as a result of the in-situ activation, the surface carbon content is converted into carbide with the assigned C(-II) carbide peak found closest to the reference spectral line of C 1s in VC. Upon further analysis, the V  $2p_{3/2}$  peak is also observed to shift towards 513 eV throughout the cycles (comparing it to the 513 eV reference spectral line of V  $2p_{3/2}$  in VC [74]), and therefore, the vanadium content after the in-situ activation is identified as being a mixture of V(0), V(II), and V(IV) oxidation states corresponding to V in metallic

state, in VO, and in VC, respectively.

Overall, the XPS results show that in the as-deposited sample, the surface oxygen content is effectively decreased by the in-situ activation, while the surface metal content is found to be reduced to metallic state, and the surface carbon content is converted to carbide identified as VC, indicating good activability of the as-deposited coating. Furthermore, a clear trend is observed in the decrease of the efficiency of the activation as witness samples were subjected to an increasing number of high pressure H<sub>2</sub> injection cycles, seen from the decreasing extent of oxygen removal, metal reduction, and carbon-to-carbide conversion on the sample surfaces during the in-situ activation. Venting-activation cycles have been previously observed to lead to the formation of an oxygen gradient near the surface of the TiZrV coating, progressively reducing the oxygen dissolution rate during activations [60]. However, aging experiments previously were conducted with samples not subjected to H<sub>2</sub> injections. It is proposed, that the oxygen dissolution takes place similarly in the samples of this work as well, as well as the oxygen gradient formation over the venting-activation cycles, and the decrease of the oxygen dissolution rate is potentially accelerated in the samples of this work by the residual H<sub>2</sub> content in the samples that remains in the coating after the reactivations. The residual hydrogen content and the formation of an oxygen-enriched layer near the coating surface potentially mutually exacerbate the effect of aging and the rate of hydrogen removal from the coating during (re)activations, seen from the decrease of the efficiency of the in-situ activation already throughout 6 cycles. For further analysis, to confirm the presence and the extent of the formation of an oxygen gradient near the surface of the coating in the samples presented in this work as well, XPS depth-profile measurements were carried out, the results of which however, due to time limitations, are not included in this work.

### Secondary Electron Yield

Secondary electron yield (SEY) was measured in the same set-up as the XPS machine of witness samples both in as-received condition, and after the in-situ activation in the XPS set-up, after being cooled down to room temperature. The SEY curves of the witness samples after the in-situ activation as a function of the kinetic energy of the primary electrons are shown in fig. 4.24, with the SEY curve of HP-0 sample in as-received condition (before the in-situ activation) included as well. In order to provide a quantitative overview, the maximum values of the curves are displayed in table 4.5. The initial SEY of the as-deposited HP-0 sample in as-received condition is 1.79, which, as a result of the in-situ activation, decreases to a value of 1.11. The maximum SEY values are observed to increase as the samples were subjected to more high pressure cycles. This correlates with the observation that the oxygen removal became also increasingly ineffective for the witness samples as progressing in the cycles, since the empirical relationship between higher oxide content on the getter surface and higher SEY has been established previously in literature [75]. The maximum depth probed by the SEY measurement was established as 50 nm by Monte Carlo electron trajectory simulations as shown in fig. A.10, showing that the

measurement probes the top surface of the material. While the surface roughness values of the measured samples indicated that the activations the cycled samples were subjected to might increase the surface roughness of the samples, which can affect the SEY of the surface, this could not be substantiated by SEM imaging, indicating the need for further surface roughness measurements to confirm these results.

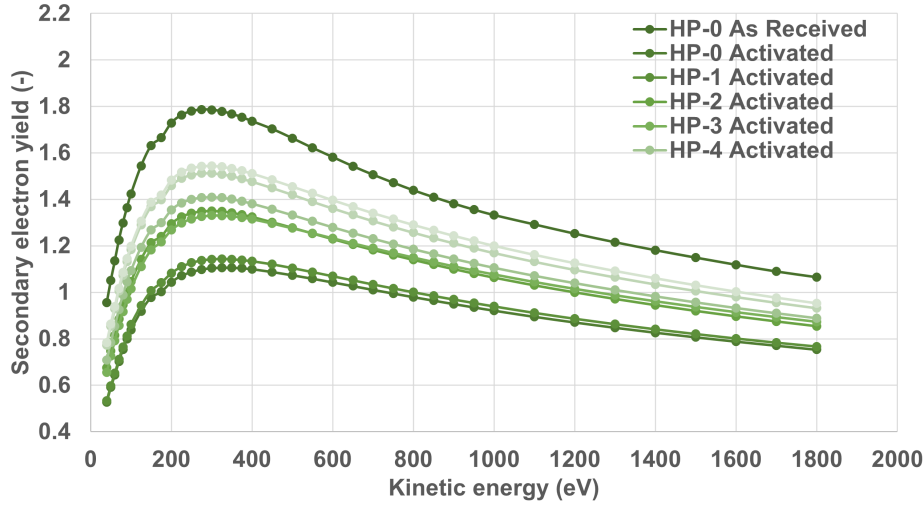


**Figure 4.24:** SEY of the witness samples from the high pressure experiment after the in-situ activation, with the SEY curve of the as-deposited sample in as-received condition included

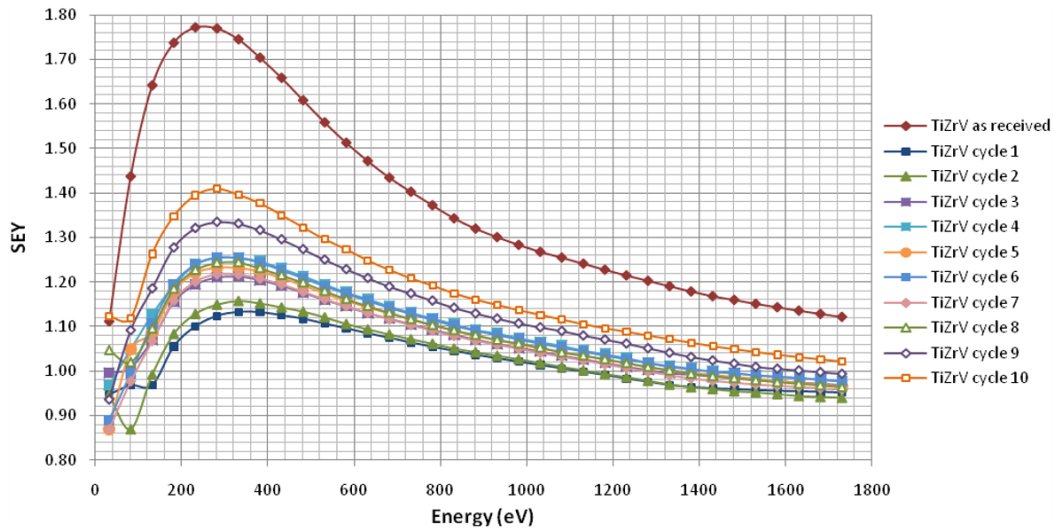


**Figure 4.25:** Reference SEY measurements of the TiZrV coating in its as-received state, and after up to 10 venting cycles [76]

The SEY of a surface is a complex property that is influenced by both its chemical composition and the surface topology [77–80], and depends also on the energy and

the incidence angle of the primary electron current [81]. It has been shown that the atomic number of the surface species and the work function of the surface alone are typically insufficient predictors of the SEY of surfaces in practice; another key factor is the dielectric properties of the surface phases [33, 77, 82]. This is underlined by the observation that metals covered in their native oxide have higher SEY than the parent metal if the native oxide is insulating (which is the case, for instance, for Al), and lower, if the native oxide is semiconducting (observed for Cu and Nb) [33]. In measurements of Baglin et al. [77], it has also been highlighted that adsorbed layers from ambient air significantly increase the SEY of technical surfaces. As both  $\text{TiO}_2$  and  $\text{ZrO}_2$  are insulating, the decrease of SEY as a result of the in-situ activation is attributed to both the desorption of the adsorbed layer on top of the native oxide layer from the getter surface, and the decrease of oxygen content and therefore the decrease of insulating metal-oxide content on the getter surface. As the witness samples subjected to increasing numbers of high pressure  $\text{H}_2$  injection cycles showed a progressively higher content of O remaining on their surface, this is in accordance with the increasing trend of SEY after the in-situ activation as progressing in the cycles.

The SEY curves are compared here with the results from the study in [76], in fig. 4.25. In that study,  $1\text{ }\mu\text{m}$  thick Ti-Zr-V coating was subjected to 10 SEY measurements with in-situ activations ( $250\text{ }^\circ\text{C}$  for 2 h), between which the sample was vented to air to allow native oxide formation, to find that the SEY value of 1.35 cited as the threshold for the application of the coating in the Large Hadron Collider (LHC) [33, 75] is only exceeded after 8 cycles of venting and activation. This indicates that the SEY increase in fig. 4.24 might not be simply due to the repeated venting and activation, but the  $\text{H}_2$  injections might play a role as well in accelerating the aging of the coating. However, in order to be conclusive, reference activated samples are needed to be measured that undergo the same high pressure cycles as the witness samples, but without  $\text{H}_2$  injections. Regardless, from the results in fig. 4.24 it is clear that the reduced efficiency of activation of the TiZrV coating as progressing in the cycles affects the SEY values of the coating as measured after the in-situ activations as well.

	<b>SEY<sub>max</sub></b>	
	As-received	After in-situ activation
<b>HP-0</b>	1.79	1.11
<b>HP-1</b>	1.73	1.14
<b>HP-2</b>	1.73	1.35
<b>HP-3</b>	1.76	1.33
<b>HP-4</b>	1.80	1.41
<b>HP-5</b>	1.88	1.51
<b>HP-6</b>	1.89	1.54

**Table 4.5:** Maximum SEY values of the witness samples from the high pressure experiment

### Thermal Desorption Spectroscopy

Thermal desorption spectroscopy (TDS) was performed on the witness samples as well as the bare substrate to study to H release from the coating. During the TDS measurement, the sample was heated under vacuum ( $\sim 1 \times 10^{-9}$  hPa) from room temperature up to 1000 °C through the sample holder, and the gases released from the sample were monitored by following the evolution of partial pressures of selected gases by the residual gas analyzer above the sample. The curves in counts of 2 m/z corresponding to H<sub>2</sub> per unit mass of the TiZrV coating are shown as a function of heating temperature in fig. 4.26. It is observed that the TDS spectrum consists of a singular peak around 350–400 °C. It has to be noted that the peak position might be affected by the unevenness of the witness samples, affecting the spread of the peak positions. From studies on the thermal desorption behavior of TiH<sub>2</sub> [83], ZrH<sub>2</sub> [84], and VH<sub>2</sub> [85], it has been shown that TDS peaks can be effectively correlated with phase transformations in the hydride material. The singular peak observed in the TDS measurements might be related to the thermodynamics of H release, or it might indicate an amorphous-to-crystalline phase transformation in the TiZrV coating. In order to confidently interpret these spectra, complementary measurements, such as differential scanning calorimetry, as well as XRD of samples from interrupted TDS measurements needed to be taken. The TDS spectrum of the witness sample HP-3 shows a higher H content released than in the case of the other samples, which indicates that the previously given interpretation does not fully account for the anomalously high pressures during the 4<sup>th</sup> cycle activation, and there might have been an increased amount of H sorption after the 3<sup>rd</sup> cycle reactivation during the transmission method measurement.

As observed, the onset of H<sub>2</sub> release from the samples is observed at  $\sim 250$  °C in the TDS measurement, while during the (re)activations the hydrogen release is observed at much lower temperatures, including the target temperature of 230 °C. The explanation for this is two-fold; firstly, the heating rate is much higher in the TDS measurement (5 °C/min, or 300 °C/h) than during activation (50 °C/h) or reactivation (100 °C/h), and higher heating rates are known to shift desorption peaks to higher temperatures; in fact, this is exploited in the technique of measuring desorption activation energies by TDS [86]. Another consideration is that in the TDS set-up, the TiZrV surface area is substantially smaller compared to the pumping speed of the auxiliary pump of the TDS system (1 cm<sup>2</sup> and 160 dm<sup>3</sup>/s) compared to the experimental test bench (2200 cm<sup>2</sup> and  $\sim 40$  dm<sup>3</sup>/s), which results in a lowered sensitivity for smaller desorption peaks. These two factors lead to hydrogen release not being observed at 230 °C in the TDS measurement.

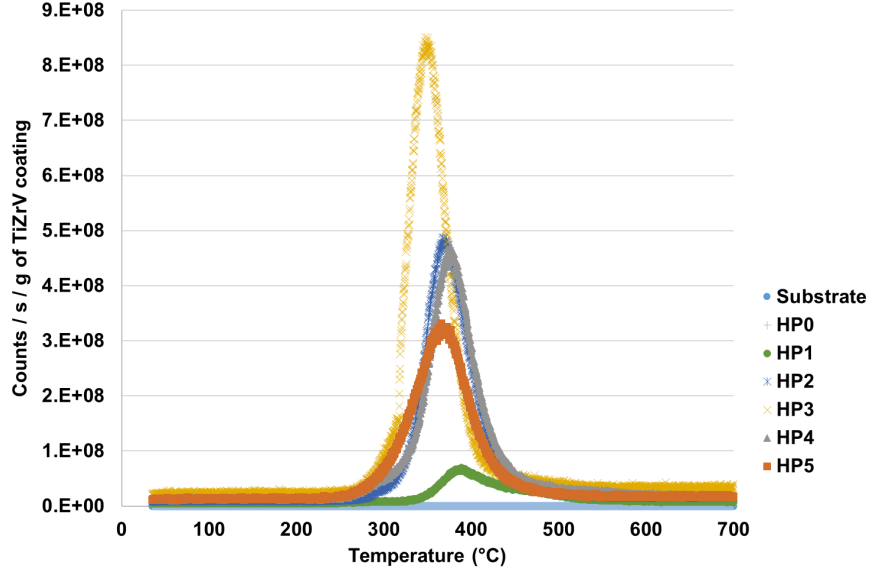


**Figure 4.26:** TDS spectra of  $H_2$  (2 m/z) as a function of temperature normalized to unit mass of the TiZrV coating

### 4.3 Low Pressure Experiment

The low pressure experiment was carried out to study the  $H_2$  sorption and saturation process of the TiZrV coating at the nominal injection pressure of  $5 \times 10^{-7}$  hPa in order to simulate its saturation behavior under similar conditions as during the  $H_2$  gas injections in the Large Hadron Collider beauty (LHCb) machine during fixed target experiments [22]. The low pressure experiment consisted of a single cycle; after the mounting of the TiZrV coated test pipe to the test bench with the witness samples placed inside, the test bench was baked out, followed by the activation heating process of the test pipe, and the measurement of the initial sticking coefficients of  $H_2$ ,  $N_2$ , and CO. The  $H_2$  injection part of the experiment was then initiated:  $H_2$  was continuously injected at  $5 \times 10^{-7}$  hPa as measured with the ECG-2 pressure gauge, and the  $H_2$  injection was carried out over  $\sim 83$  days out of the  $\sim 109$  days of the injection part of the experiment. During the injection part of the experiment, the injection was terminated in regular intervals to allow for pressure regeneration and the intermittent measurement of the  $N_2$  and CO sticking coefficients. After observing significant decrease of the  $H_2$  sticking coefficient of the TiZrV coating to assume saturation, a further set of  $H_2$ ,  $N_2$ , and CO sticking coefficient measurements were carried out and the test pipe was then reactivated similarly as in the high pressure experiment. Following the reactivation, the regained  $H_2$ ,  $N_2$ , and CO sticking coefficients were measured again, and the test pipe was vented to ambient air, dismantled, subjected to visual inspection by endoscopy, and witness samples were subjected to materials characterization. For the hydrogen quantity calculations, the TiZrV coating quantity on the inside the test pipe was estimated similarly as in

section 4.2.1 to be 0.03020 mol.

#### 4.3.1 Vacuum Results

Firstly, the evolution of the sticking coefficient of the test gases ( $\text{H}_2$ ,  $\text{N}_2$ , and  $\text{CO}$ ) are analyzed over the low pressure experiment. Table 4.6 tabulates the sticking coefficient values measured after the activation, after the low pressure injection, and after the reactivation. The initial sticking coefficient for  $\text{H}_2$  was measured as  $6.1 \times 10^{-3}$  which is seen to decrease by an order of magnitude as a result of the low pressure  $\text{H}_2$  injection ( $5.5 \times 10^{-4}$ ). After the reactivation, the  $\text{H}_2$  sticking coefficient was measured as  $3.0 \times 10^{-4}$  indicating partial regainability by the reactivation. In accordance, the ultimate pressures at the end of the test pipe were measured as  $9.00 \times 10^{-12}$  hPa after the activation,  $1.62 \times 10^{-10}$  hPa after the low pressure  $\text{H}_2$  injection, and  $8.50 \times 10^{-12}$  hPa after the reactivation. The trend observed by the sticking coefficient measurements follows the trend observed in the high pressure experiment as well; the sticking coefficient is found to decrease after excessive  $\text{H}_2$  sorption, and it is partially regained after hydrogen is released from the coating during the reactivation. The initial sticking coefficient for  $\text{N}_2$  is in the range of that of  $\text{H}_2$ , while for  $\text{CO}$  it is an order of magnitude higher, in accordance with previous findings, as shown in fig. 2.5 [2]. The sticking coefficients for both  $\text{N}_2$  and  $\text{CO}$  was measured to decrease by a factor of  $\sim 20$  after the low pressure  $\text{H}_2$  injection, and both show a greater regainability by the reactivation than  $\text{H}_2$ .

	Sticking coefficient (-)		
	Before injection	After injection	After reactivation
<b><math>\text{H}_2</math></b>	$6.1 \times 10^{-3}$	$5.5 \times 10^{-4}$	$3.0 \times 10^{-3}$
<b><math>\text{N}_2</math></b>	$6.9 \times 10^{-3}$	$1.3 \times 10^{-3}$	$6.7 \times 10^{-3}$
<b><math>\text{CO}</math></b>	$1.6 \times 10^{-2}$	$2.7 \times 10^{-3}$	$1.1 \times 10^{-2}$

**Table 4.6:** Overview of the sticking coefficients measured before the low pressure injection, after the low pressure injection, and after reactivation over the course of the low pressure experiment

The evolution during the continuous low pressure injection as a function of sorbed hydrogen fraction is shown in further detail in fig. 4.27. The sticking coefficient was calculated during the continuous injection based on the transmission ratio from the pressures measured with the ECG-2 and ECG-3 gauges in an identical way to the transmission method measurement, and in time steps of 60 s. The sorbed hydrogen fraction in  $\text{H} / \text{TiZrV}$  at every measurement point during injection was calculated as described in the following. The pressure measured by the ECG-2 gauge at every measurement point was converted to  $Q(t)$  sorption rate through eq. (8) by substituting the calculated pumping speed of the  $\text{TiZrV}$  coating. Then, the sorbed hydrogen quantity at every measurement point is calculated by the area under the obtained  $Q(t)$  curve, the cumulative curve of which yields the hydrogen fraction

values at every measurement point. The pumping speed of the TiZrV coating for  $H_2$  ( $S_{TiZrV}$ ) was calculated from the sticking coefficient through  $S_{TiZrV} = CP \cdot C_{test\ pipe}$ , where  $CP$  denotes the capture probability of the test pipe and  $C_{test\ pipe}$  is the conductance of the entrance of the test pipe calculated via eq. (10); the maximum pumping speed of the test pipe. The capture probability was calculated from the sticking coefficient through the transfer curve shown in fig. 3.9.

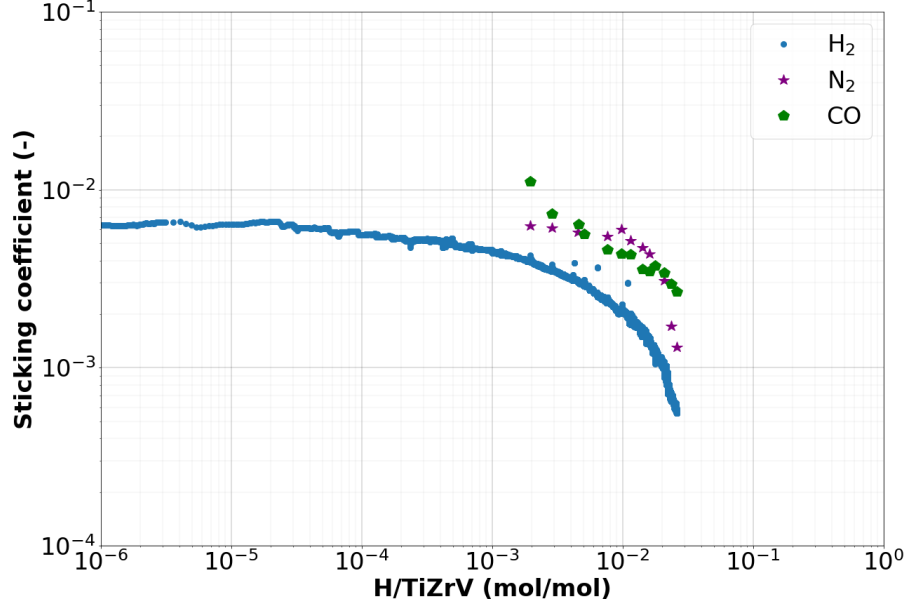


**Figure 4.27:** Evolution of the sticking coefficient for  $H_2$ ,  $N_2$  and  $CO$  during the low pressure injection experiment

Figure 4.27 shows that the sticking coefficient for  $H_2$  decreases after excessive sorption of  $H_2$ , and the rate of the decrease of the sticking coefficient is observed to increase as the sorbed hydrogen quantity increases,. This shows that even in high vacuum conditions, at high enough hydrogen quantities, the sorbed hydrogen does affect the  $H_2$  sticking coefficient of the coating. The maximum sorbed hydrogen quantity observed in this experiment is  $0.026\text{ H/TiZrV (mol/mol)}$ , lower than in the high pressure experiment ( $\sim 0.4\text{ H/TiZrV (mol/mol)}$ ), which highlights the relationship between the equilibrium solubility of hydrogen and the injection pressure.

The evolution of  $N_2$  and  $CO$  sticking coefficients is seen to be characterized also by a decreasing trend throughout the low pressure  $H_2$  injection. This can be attributed to the effect of the  $H_2$  sorption; the sorbed  $N_2$  and  $CO$  quantities were calculated from the pressure profiles during their respective transmission method measurements in a similar way as the calculation of sorbed hydrogen quantity described previously to find that overall, the total sorbed  $N_2$  quantity was  $2.68 \times 10^{12}\text{ molecules/cm}^2$ , and the total sorbed  $CO$  quantity was  $1.53 \times 10^{12}\text{ molecules/cm}^2$  throughout the transmission measurements during the low pressure injection experiment, which, after a comparison with fig. 2.6 and fig. 2.5, indicate that the decreasing trend of

their sticking coefficient is due to  $H_2$  sorption, and not surface saturation by  $N_2$  or  $CO$ . The experiments of this work do not reveal the exact mechanism behind this phenomenon which needs further investigation, however, this result points in the direction that excessive hydrogen sorption potentially affects the surface of the TiZrV coating as well, reducing available sorption sites for not only  $H_2$ , but also for  $N_2$  and  $CO$ .

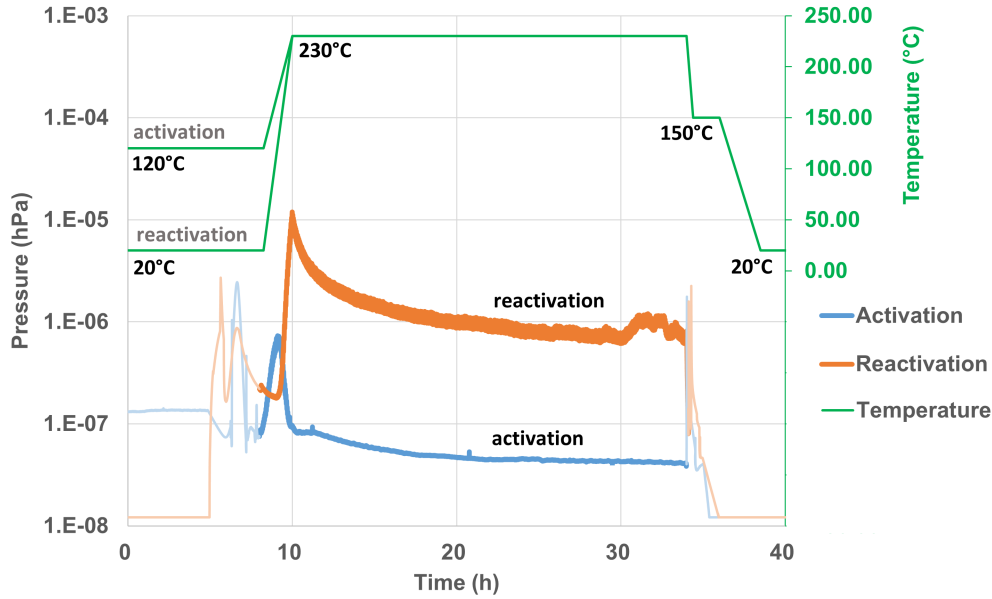


**Figure 4.28:** Pressure evolution during the activation and the reactivation during the low pressure experiment. The curves are arranged so that the 10 h mark notes the time of reaching the 230 °C activation temperature, and for reference, the temperature profile of the test pipe is included as well. For better readability of the plot, the pressures before the starting of the heating of the test pipe and the pressures after the 24 h activation are displayed in a lighter hue as they contain pressure rises not related to gas release from the coating, but to the degassing procedure of the pressure gauges and the RGA

The pressure evolution during the activation and the reactivation in the low pressure experiment is shown in fig. 4.28. The activation pressure profile is similar to that of an unsaturated TiZrV coating, such as the activation pressure profile of the 1<sup>st</sup> high pressure experimental cycle shown previously in fig. 4.10; the activation pressure profile in fig. 4.28 also confirms the onset of the native oxide dissolution at 180–200 °C and the plateau pressure at the end of the activation ( $3.94 \times 10^{-8}$  hPa) indicates low residual hydrogen content in the coating. In comparison, the reactivation pressure profile having taken place after the low pressure injection indicates significant hydrogen release from the coating with a maximum pressure of  $1.20 \times 10^{-5}$  hPa, and also a higher residual hydrogen content in the coating at the end of the reactivation (with a plateau pressure of  $7.01 \times 10^{-7}$  hPa), again highlighting that the complete removal of the injected hydrogen from the coating is inhibited by the reactivation conditions

(temperature and duration) and the pumping speed of the auxiliary pump. The released hydrogen quantities were calculated as 0.0002 H/TiZrV (mol/mol) during the activation, and 0.0155 H/TiZrV (mol/mol) during the reactivation.

### 4.3.2 Endoscopy

The coating was inspected by endoscopy along the full length of the test pipe after the low pressure experiment (fig. 4.29) and no damage on the coating surface, and no visual signs of flaking, powdering, or peel-off was observed.



**Figure 4.29:** Perspective view of the TiZrV coating during the endoscopy after the low pressure experiment

### 4.3.3 Materials Characterization

#### Surface Imaging

The surfaces of the as-deposited LP-0 sample as well as the surface of the LP-1 witness sample subjected to the low pressure experiment were investigated by SEM and representative micrographs are shown in fig. 4.30. Similarly to the observations in the high pressure experiment, no alterations to the top surface morphology could be identified as a result of the low pressure experiment at high magnifications, while some flaking and delamination of the coating was observed even at macroscopical scales in both samples, especially near the sample edges, highlighting again the difficulty of determining H<sub>2</sub> injection related embrittlement from samples subjected to strain due to sample handling, motivating further nanomechanical testing on flat witness samples.

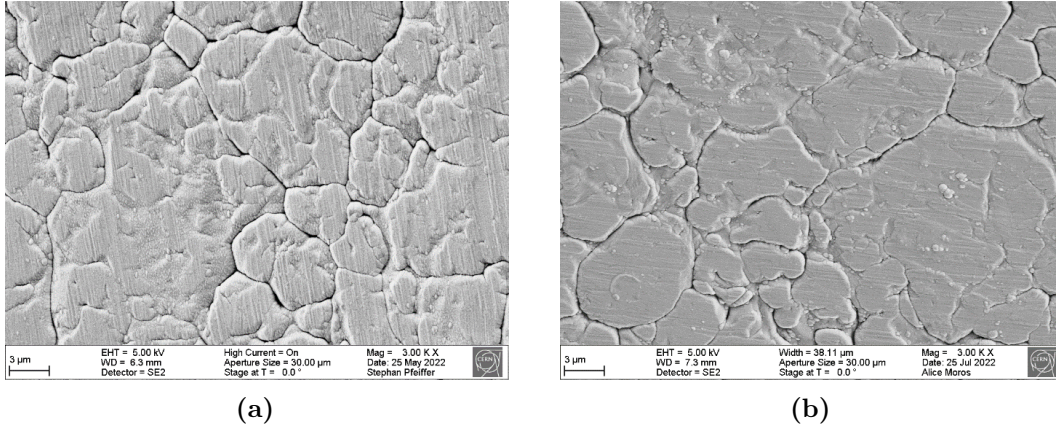


**Figure 4.30:** SEM images of the as-deposited LP-0 sample (a) and the LP-1 witness sample after the low pressure experiment (b)

### X-ray Photoelectron Spectroscopy

The relative surface composition of the surfaces of the witness samples from the low pressure experiment were also measured with XPS in an identical procedure as described for the HP witness samples. The full surface composition data as measured with XPS is tabulated in table A.7 and the analysis of the results are presented in the following paragraphs. Besides the as-deposited LP-0 witness sample and the witness sample subjected to the low pressure experiment (LP-1), the reference activated sample, LP-0A was also characterized with XPS measurements.

Firstly, the evolution of the surface oxygen and surface carbon content is shown through the evolution of the normalized O 1s and C 1s peak area throughout the in-situ activation in fig. 4.31, and fig. 4.32, respectively. Table 4.7 tabulates the relative surface oxygen content decrease, the relative surface carbon content decrease, and the carbon-to-carbide conversion ratio as well calculated from the peak areas. While for the as-deposited sample, the surface oxygen content is observed to be effectively reducible by the in-situ activation (overall 82.1 % decrease), the surface oxygen content decrease is observed to be more inhibited for both the reference activated, and the cycled sample presenting a  $\sim 65\%$  relative surface oxygen content decrease. This alone could indicate that the extra step of venting and activation in the case of the LP-0A and LP-1 samples already reduces the rate of oxygen dissolution into the coating compared to the as-deposited LP-0 sample, without the additional effect the  $H_2$  injection introduces. It has to be noted that these samples had relatively high Na and K surface contamination, as shown in table A.7, as well as that the exposure to no  $H_2$  of the reference activated sample was not completely warranted during the reference activation, since the reference activation was carried out in the LP test pipe after the low pressure experimental cycle, releasing some of its residual hydrogen content during the reference activation. Therefore, to confidently draw conclusions on the source of the deteriorated oxygen decrease of the LP-0A and LP-1 samples, it is necessary to repeat these measurements with samples without

alkali surface contamination, and with a reference activated sample activated in a test pipe with a fresh, as-deposited TiZrV coating.

From the analysis of the content and chemical state of carbon on the sample surfaces, it is observed that the carbon removal from the surface presents virtually ineffective during the in-situ activation (fig. 4.32), and while the as-deposited sample presents a 74.6 % carbon-to-carbide conversion ratio (see table 4.7 and fig. 4.33), this conversion ratio is lower for the reference activated and the cycled witness samples. This could indicate, similarly to the case of the high pressure witness samples, that the increased amount of oxygen remaining on the surface of the LP-0A and LP-1 samples after the in-situ activation might affect the rate of the conversion of the surface carbon content to carbides.

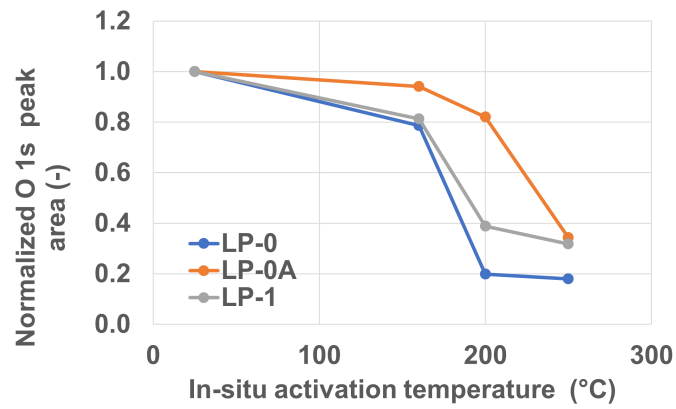


**Figure 4.31:** Evolution of the normalized O 1s peak area throughout the in-situ activation as measured with XPS on the witness samples from the low pressure experiment

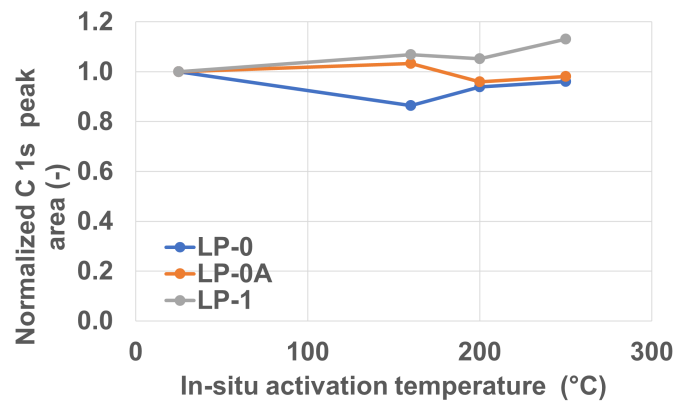


**Figure 4.32:** Evolution of the normalized C 1s peak area throughout the in-situ activation as measured with XPS on the witness samples from the low pressure experiment

	$\Delta_{\text{O } 1s \text{ area}}$	$\Delta_{\text{C } 1s \text{ area}}$	$\Delta_{\text{Carbide / Total C}}$
<b>LP-0</b>	0.821	0.039	0.746
<b>LP-0A</b>	0.658	0.019	0.586
<b>LP-1</b>	0.682	-0.131	0.424

**Table 4.7:** Relative surface oxygen content decrease as a result of activation ( $\Delta_{\text{O } 1s \text{ area}}$ ), relative surface carbon content decrease as a result of activation ( $\Delta_{\text{C } 1s \text{ area}}$ ), and carbon-to-carbide conversion ratio ( $\Delta_{\text{Carbide / Total C}}$ ) of the witness samples from the low pressure experiment, calculated as described in table 4.4

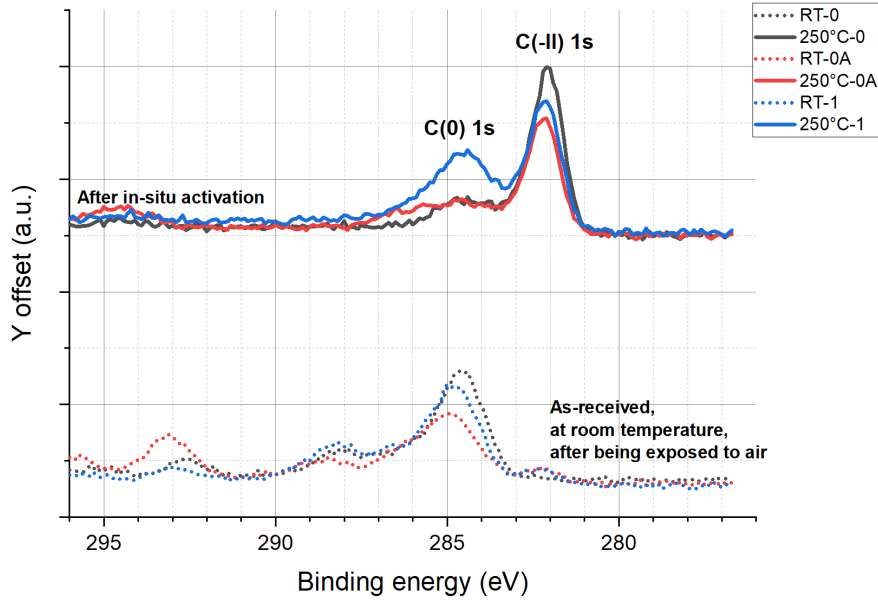


**Figure 4.33:** XPS spectra of the C 1s peaks of the witness samples from the low pressure experiment in as-received condition and after the in-situ activation

**Metal Content** The chemical state of the surface metal content of the witness samples from the low pressure experiment was analyzed as well, and the XPS spectra of Ti (fig. 4.34), Zr (fig. 4.35), and V (fig. 4.36) show a clear indication of the metals being in an oxidized state in as-received condition, and the surface metals being reduced by the in-situ activation, observed in all cases by the appearance of dominant core level peaks that are shifted towards lower binding energies after the in-situ activation.

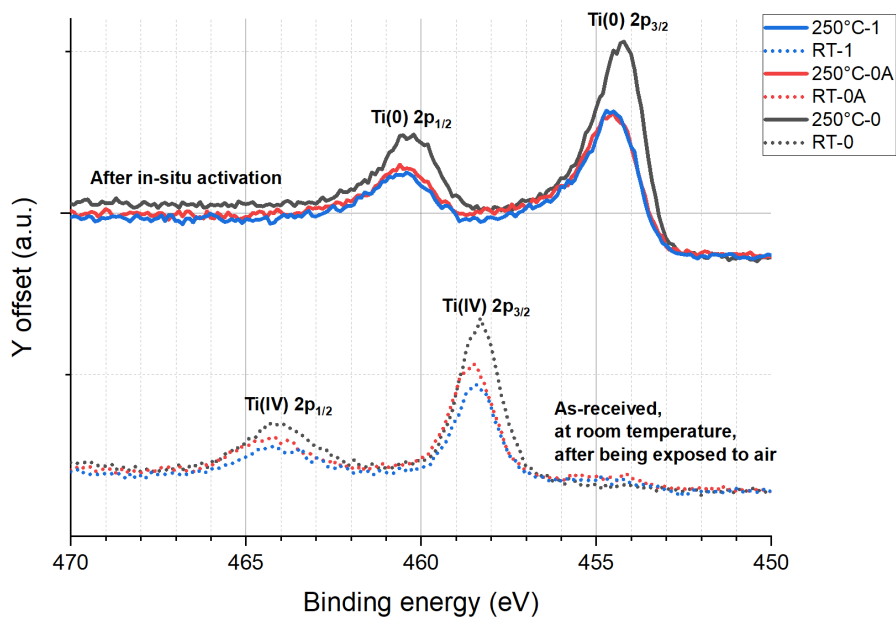


**Figure 4.34:** XPS spectra of the Ti 2p peaks of the witness samples from the low pressure experiment in as-received condition and after the in-situ activation

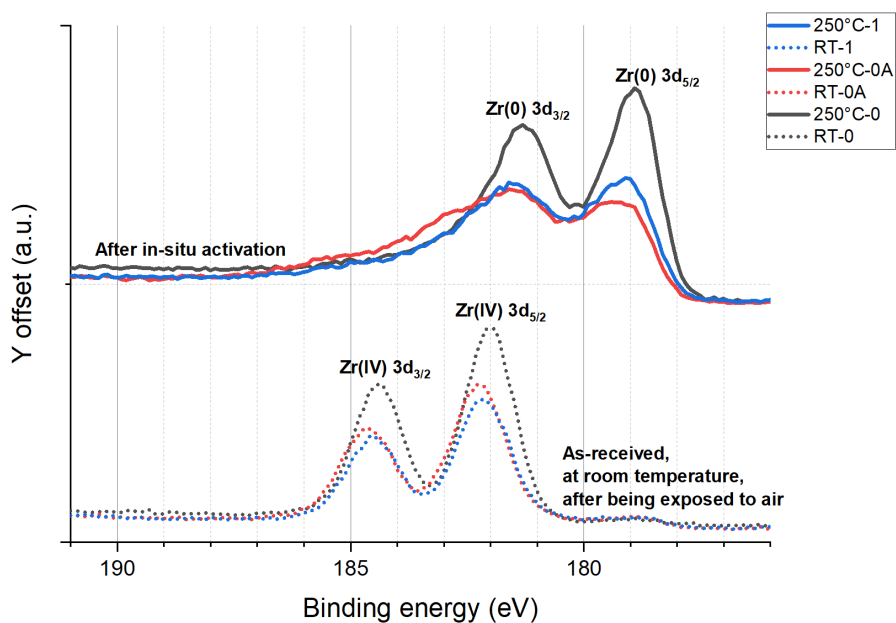


**Figure 4.35:** XPS spectra of the Zr 3d peaks of the witness samples from the low pressure experiment in as-received condition and after the in-situ activation

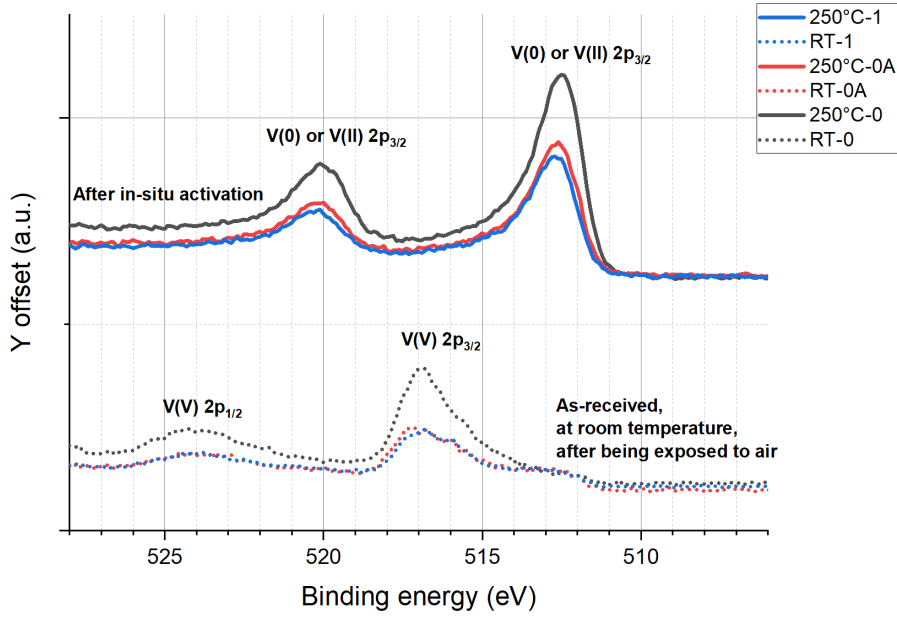


**Figure 4.36:** XPS spectra of the V 2p peaks of the witness samples from the low pressure experiment in as-received condition and after the in-situ activation

### Secondary Electron Yield

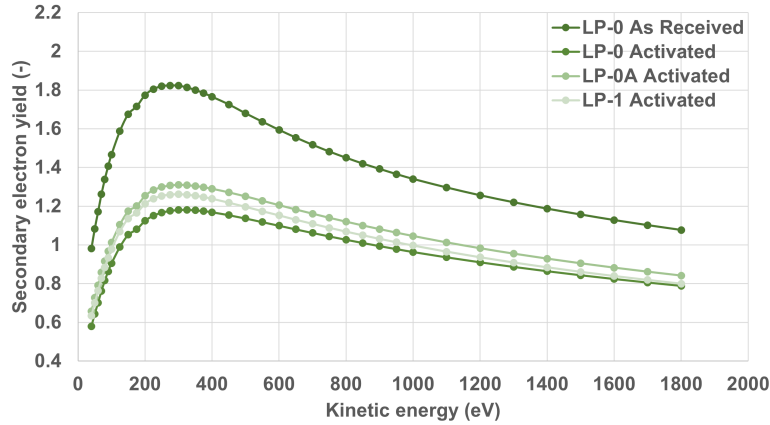


**Figure 4.37:** SEY of the witness samples in as-received condition of the as-deposited LP-0 sample, and after the in-situ activation of the LP-0, LP-0A, and LP-1 samples from the low pressure experiment

The results of the SEY measurements on the LP-0, LP-0A, and LP-1 are shown in fig. 4.37. Similarly to the SEY results in the high pressure experiment, the initial SEY maximum value in the as-received condition of the samples (1.82 for LP-0) were observed to decrease significantly as a result of the in-situ activation (1.18 for LP-0, 1.31 for LP-0A, and 1.26 for LP-1), attributed to the desorption of the adsorbed

layer on top of the native oxide, as well as the removal of oxygen (and therefore insulating metal-oxides) from the sample surface. However, in accordance with the higher O content on the surface of the LP-0A and LP-1 samples, the SEY after the in-situ activation is also observed to be higher for these samples than that of the as-deposited LP-0 sample. While direct conclusion cannot be drawn to discriminate the effect of aging from the effect of the hydrogen injection from these samples due to the aforementioned alkali surface contamination, these measurements again underline the relationship between the residual O content of the surface, and its SEY.

## Chapter 5

# Conclusion

The research presented in this work was aimed at studying the  $H_2$  sorption behavior of the state-of-the-art TiZrV non-evaporable getter (NEG) coating when subjected to the sorption of  $H_2$  quantities at which the saturation and embrittlement of the coating could occur, as it was not studied previously in literature.  $H_2$  sorption experiments were carried out at two injection pressure conditions, under vacuum and at room temperature, on TiZrV coated stainless steel pipes with witness samples placed inside for materials characterization. Overall, visual signs of embrittlement, such as flaking, peel-off, or powdering of the coating inside the pipes was not observed as a result of the  $H_2$  injections, proving the amorphous TiZrV coating more robust to  $H_2$  embrittlement than other non-evaporable getter materials.

The high pressure experiment, which consisted of 6 cycles of instantaneous injection of  $H_2$  at the nominal pressure of 1 hPa showed that the coating on the pipe preserves its mechanical integrity even after 6 absorption and release cycles of at minimum 0.2–0.4 H/TiZrV (mol/mol) hydrogen quantities, which is significantly higher than for other non-evaporable getter materials. The  $H_2$  sticking coefficient in ultra-high vacuum, as well as the  $H_2$  sorption rate of the coating in medium vacuum have both shown a clear dependence on the hydrogen content in the coating at the investigated injection quantities, showing a decreasing trend when increasing quantity of hydrogen is absorbed in the coating. The ability of the coating to dissolve its surface oxygen content during activation was studied by X-ray photoelectron spectroscopy (XPS) via measuring the surface composition during an in-situ activation in the XPS set-up. With increasing number of  $H_2$  injection cycles, the oxygen dissolution rate into the coating was found to progressively decrease, which was reflected also in the progressive increase of the surface metal content of the coating remaining in an oxidized chemical state. The carbon-to-carbide conversion of the surface carbon content of the coating during the in-situ activation also showed progressive decrease throughout the injection cycles, attributed to be a consequence of increased oxygen content remaining on the surface after the in-situ activation as well. From measurements of the secondary electron yield (SEY) of activated samples, an increasing trend in SEY was also observed as a function of the high pressure  $H_2$  injection cycles, which is in accordance with the progressively increasing

content of oxygen remaining on the surface after activation. The SEY of activated samples exceeded the upper technical limit of 1.35 SEY already after the 2<sup>nd</sup> cycle, however, these results are only an indication of the lower oxygen dissolution rate during activation. The in-situ activations were carried out at 250 °C only with 1 h duration, while activation with a longer, 24 h duration is expected to result in a better regeneration of the metallic surface with its SEY potentially decreasing below the technical specification limit, which has to be studied in a future work.

A significant decrease in both H<sub>2</sub> sticking coefficient and oxygen dissolution rate during activation was observed already after the 1<sup>st</sup> high pressure experimental cycle. The decrease of the H<sub>2</sub> sticking coefficient and the oxygen dissolution rate during activation has been previously reported to occur as a result of repeated venting-activation cycles by the formation of an oxygen-enriched layer near the surface of the coating owing to inhomogeneous oxygen dissolution during 24 h 230 °C activations, which was also used in this work. This phenomenon, referred to as aging, however, was previously observed to occur after a much higher number of venting-activation cycles than 1. Therefore, the results of this work suggest that residual hydrogen quantity remaining in the coating from the H<sub>2</sub> injections after reactivation have the potential to exacerbate the effect of aging, potentially by the sorbed hydrogen content lowering the diffusion rate of oxygen in the coating.

The effect of hydrogen sorption on the sticking coefficient and the sorption rate can be attributed to potentially both the decrease of the diffusion rate of hydrogen in the coating as a result of hydrogen sorption, as well as hydrogen sorption related surface modifications that decrease the number of available dissociation sites for hydrogen sorption. To determine the rate-limiting step of the sorption process in coatings with high hydrogen content, experiments with thermal desorption spectroscopy (TDS) with varying heating rates are proposed. Further investigation of samples subjected to H<sub>2</sub> injections without reactivation is also considered to study potential alterations in the coating that the reactivations used in this work might have prevented from identifying. To further discriminate the effect of hydrogen injection cycles from aging, it is proposed to prepare and study reference samples not subjected to H<sub>2</sub> injections, as well as the current witness samples by XPS depth-profiling. In order to quantify the adhesion of the coating to the substrate as well as its potential degradation as a result of the H<sub>2</sub> injections, flat samples are proposed for a future H<sub>2</sub> sorption study to perform nanomechanical tests on.

In the low pressure experiment, H<sub>2</sub> was continuously injected at the nominal pressure of  $5 \times 10^{-7}$  hPa over a period of 4 months to study the hydrogen saturation behavior of the coating in high vacuum which was previously not reported in literature. The sticking coefficient was observed to decrease as a function of sorbed H<sub>2</sub> quantity up to 0.026 H/TiZrV (mol/mol) where the experiment was terminated as the sorption rate of the coating has been observed to approach zero. These results also indicate that at higher absorbed H<sub>2</sub> quantities, H<sub>2</sub> also influences the sticking coefficient of the coating, although potentially by different mechanisms than N<sub>2</sub> and CO. Besides, it was seen that after excessive H<sub>2</sub> sorption, the sticking coefficient of the coating decreased also for both N<sub>2</sub> and CO, indicating that excessive H<sub>2</sub> sorption can also affect the sticking coefficient of both N<sub>2</sub> and CO. To study the exact mechanism behind these

---

observations, samples from interrupted sorption experiments are proposed to be characterized. The difference between the maximal sorbed quantity between the high pressure and the low pressure experiment highlights the relationship between the injection pressure and the equilibrium solubility of hydrogen, as well as the hydrogen sorption rate; both being higher at higher injection pressures of  $H_2$ .

The results of this work contribute to the better estimation of the  $H_2$  saturation limit of the TiZrV coating at 1 hPa and at  $5 \times 10^{-7}$  hPa injection pressures, determined as at least 0.4 H/TiZrV (mol/mol) and 0.026 H/TiZrV (mol/mol) at the two injection pressure conditions, respectively. Although the embrittlement limit of the coating was not obtained, as embrittlement of the coating in the test pipes was not observed throughout the experiments, it is determined that the embrittlement limit of the coating is higher than 0.4 H/TiZrV (mol/mol) based on the results of this work. The direct technical relevance of this work arises from the fixed target experiments conducted at the Large Hadron Collider beauty (LHCb) experiment at the European Organization for Nuclear Research (CERN) during which  $H_2$  injections are performed directly into the vacuum system of the experiment over the Run 3 and Run 4 of the experiment between 2022 and 2032. In order to assess the safe operation limit for the  $H_2$  injections during these fixed target experiments with regard to the TiZrV coated surfaces in the LHCb vacuum system, the results of this work must be complemented with a careful assessment of the available pumping capacity of the TiZrV coated surfaces in the LHCb experiment, parts of which are subjected to lower temperature activation than the activation used in this work. In conclusion, the results of this work have demonstrated the relationship between the sorption capability and the sorbed hydrogen quantity of the TiZrV coating at higher injected hydrogen quantities previously not noted, contributed to determining its  $H_2$  sorption limit at an ultra-high and at a medium vacuum level injection pressure condition, and provide a crucial input for the estimation of the safe operation limit for the  $H_2$  injections during the fixed target operation at LHCb experiment.



# Appendices



# Appendix A

## Appendix

### A.1 Literature Review

Solubility limit (at %)				
	H	O	N	C
$\alpha$ -Ti	3 (at 300 K)	32 (at 0–1800 K)	-	0.8 (at 293 K)
$\alpha$ -Zr	1 (at 500 K)	29 (at 473–773 K)	22 (at 973 K)	<1 (at 293 K)
V	3 (at 300 K)	3.5 (at 473–773 K)	1.5 (at 400 K)	<0.1 (at 293 K)

**Table A.1:** A subset of the solubility limits of H, O, and N in atomic % in pure Ti, Zr, and V from the collection of Prodromides [4], and solubility limit of C in the respective metals [87–89]

Metal – metal-oxide	$\Delta H_{ox}$ (kJ/mol per O atom)	$\Delta H_{ss}$ (kJ/mol)
Ti – TiO	–542.9	–560.67
Zr – ZrO <sub>2</sub>	–550.65	–619.23
V – VO	–432.0	–422.15

**Table A.2:** Heat of dissolution of oxygen ( $\Delta H_{ss}$ ) in pure metals compared to the heat of formation of the stable oxide ( $\Delta H_{ox}$ ) containing the lowest number of oxygen atoms per atom of metal [4]

## A.2 Materials and Methods

### A.2.1 Calibration Constants of the Ionization Pressure Gauges

	Test bench 1 (HP experiments)			
	ECG-1	ECG-2	ECG-3	FRG
N <sub>2</sub>	1	1	1	1
H <sub>2</sub>	0.4600	0.3965	0.3341	0.4166
	Test bench 2 (LP experiments)			
	ECG-1	ECG-2	ECG-3	FRG
N <sub>2</sub>	1	1	1	1
H <sub>2</sub>	0.4506	0.4505	0.4558	0.4166
CO	1.0500	1.0408	1.0500	1

**Table A.3:** Calibration constants of the different ionization gauges used at the test benches of the vacuum experiments. Dividing the read out N<sub>2</sub> equivalent pressures by the calibration constants yields the H<sub>2</sub> or CO equivalent pressures

### A.2.2 Activation

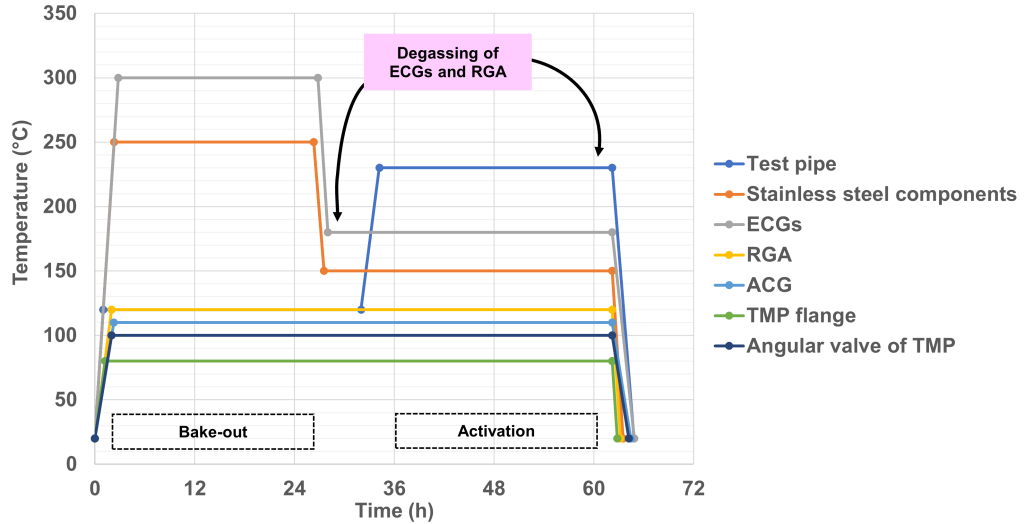


**Figure A.1:** The temperature profile during the bake-out of the test bench followed by the activation of the coated test pipe. The temperatures during activation of the test bench are referred to as degassing temperature

### A.2.3 Sticking Coefficient Measurement by Transmission Method

The sticking coefficient of the TiZrV coating was estimated through the transmission method as introduced in [90]. During the measurement, a stable flow of the test gas, in this case,  $H_2$  is injected in steps of increasing flow rates up to  $1 \times 10^{-7}$  hPa into the test bench (see fig. A.2). At every step, the ratio of the residual pressure at the entrance and the end of the pipe,  $\frac{p_{ECG-2}}{p_{ECG-3}}$ , denoted as the transmission ratio, is indicative of the sticking coefficient of the coated pipe. Based on the relationship between the sticking coefficient and the transmission ratio established by the test particle Monte Carlo simulations in section 3.6.3, the sticking coefficient is calculated at every injection step, and the extracted sticking coefficient is the average value of the estimated sticking coefficients from the steps during a transmission method measurement.

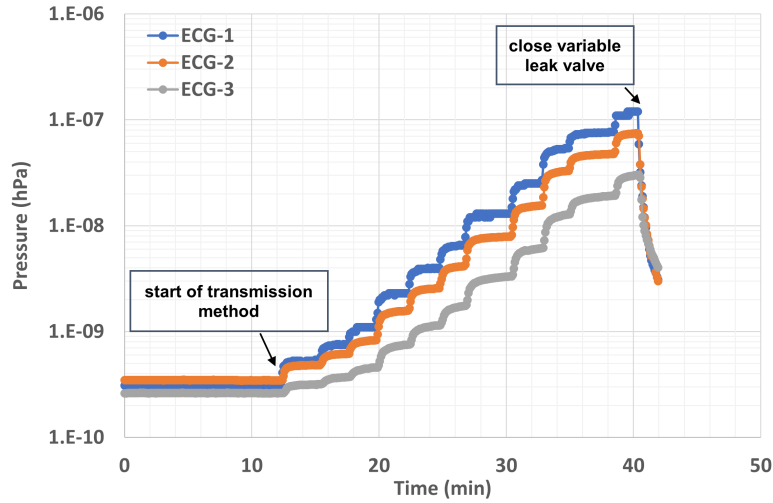


**Figure A.2:** Pressure profile during a typical transmission method measurement where  $H_2$  is injected into the test dome in steps of increasing flow rates

### A.2.4 Injection Procedure

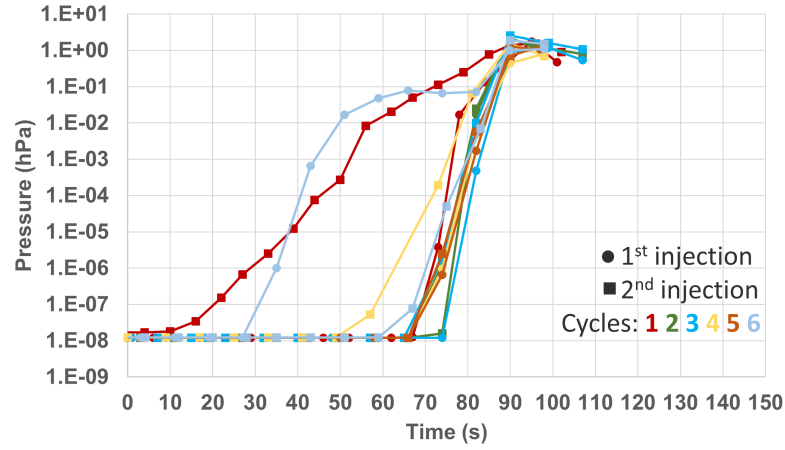


**Figure A.3:** Pressure profile during the high pressure (1 hPa)  $\text{H}_2$  injections showing the ramp up to the target pressure (at the 90 s mark in the plot) after which the variable leak valve is closed, the FRG is turned off, and the TiZrV coating is allowed to pump the injected  $\text{H}_2$  in static vacuum

### A.2.5 Calibration Factors from Calibration with the Uncoated Reference Test Pipe

Test bench 1 (high pressure experiment)			
ECG-1	ECG-2	ECG-3	FRG
0.88	1	2.04	0.81
Test bench 2 (low pressure experiment)			
ECG-1	ECG-2	ECG-3	FRG
0.73	1	0.61	0.70

**Table A.4:** Correction factors for the  $\text{H}_2$  equivalent residual pressure reading of the ionizing gauges obtained from the transmission method measurements of the calibration run on Test bench 1 and Test bench 2 using the reference uncoated test pipe

### A.3 Results and Discussions

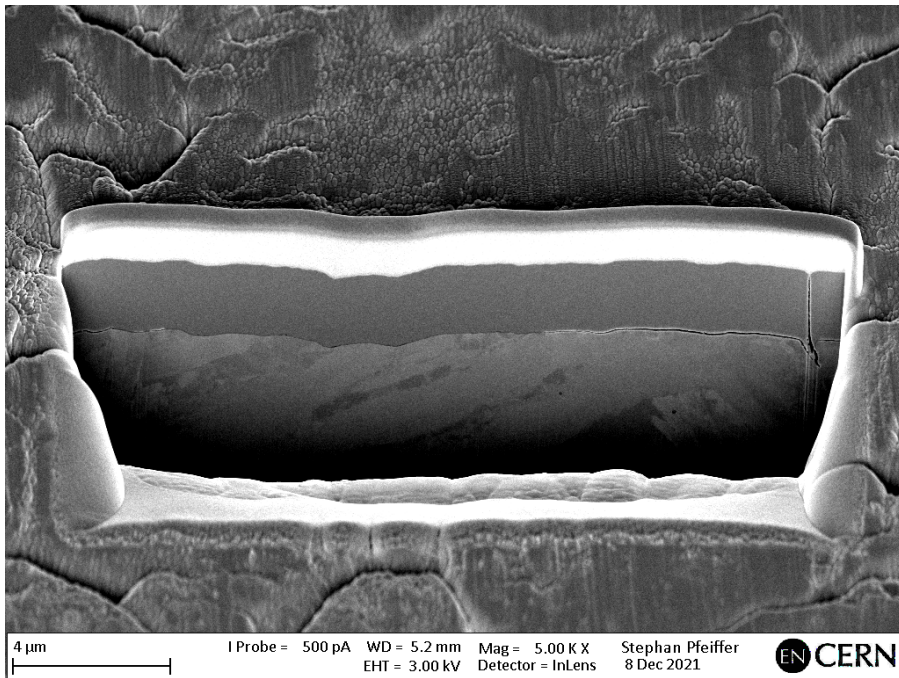


**Figure A.4:** Focused ion beam (FIB) micrograph of the cross-section of an as-deposited LP-0 sample displaying a groove at the right end of the cross-section extending through the thickness of the TiZrV coating

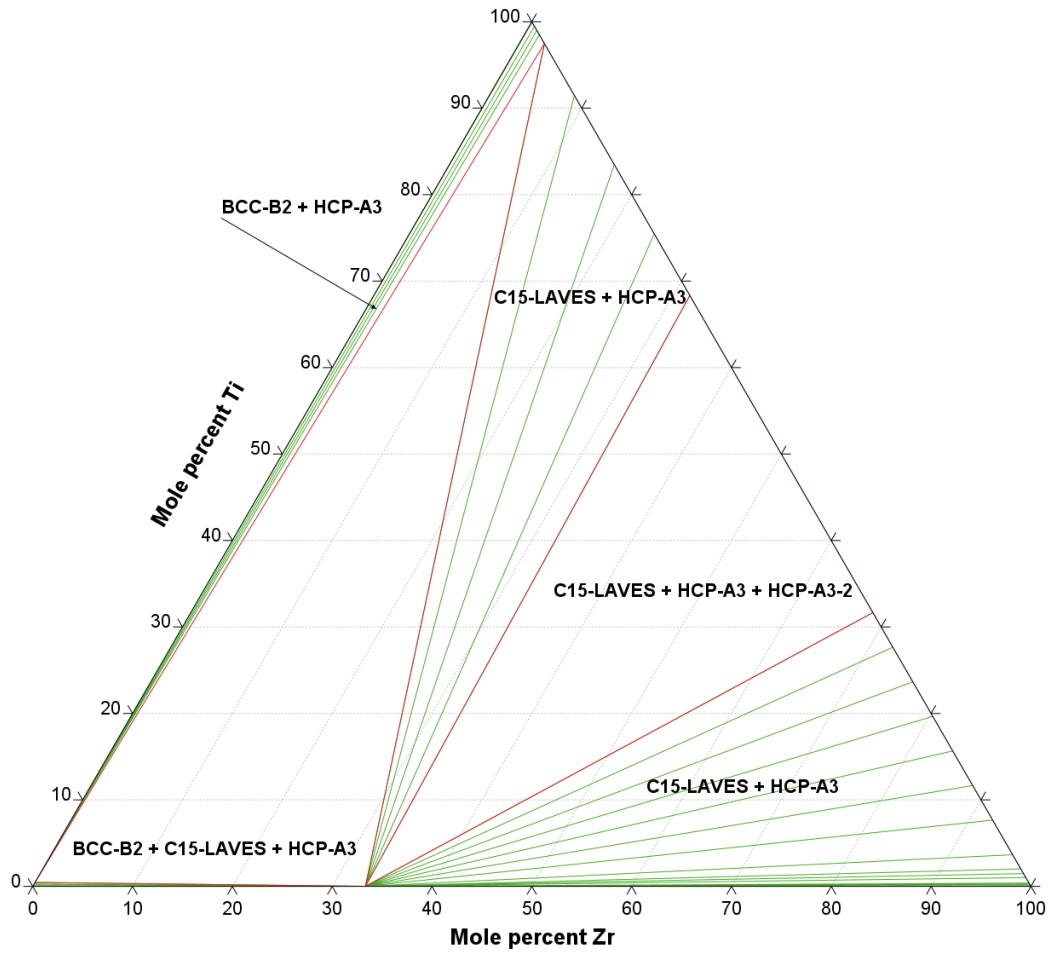


**Figure A.5:** Simulated ternary phase diagram of the Ti-Zr-V material system at 293.15 K and 1 atm pressure

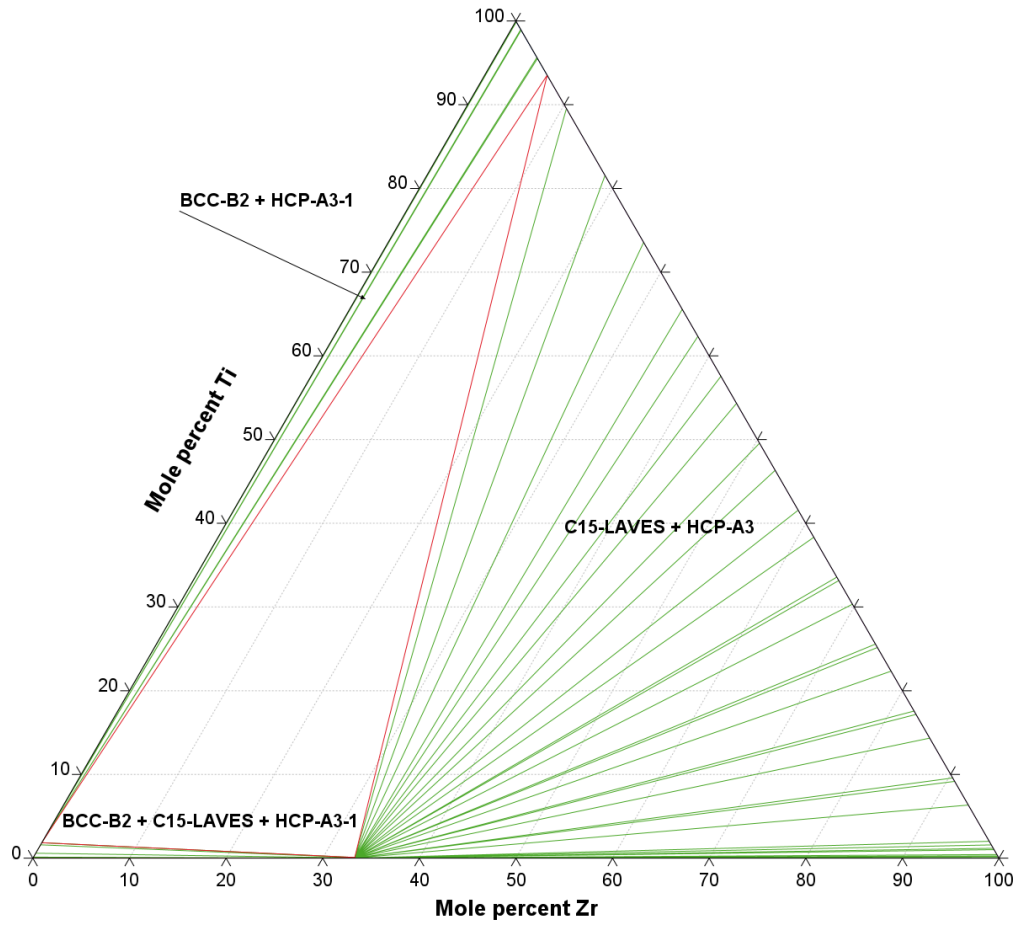


**Figure A.6:** Simulated ternary phase diagram of the Ti-Zr-V material system at 393.15 K and 1 atm pressure

## A.3.1 High Pressure Experiment

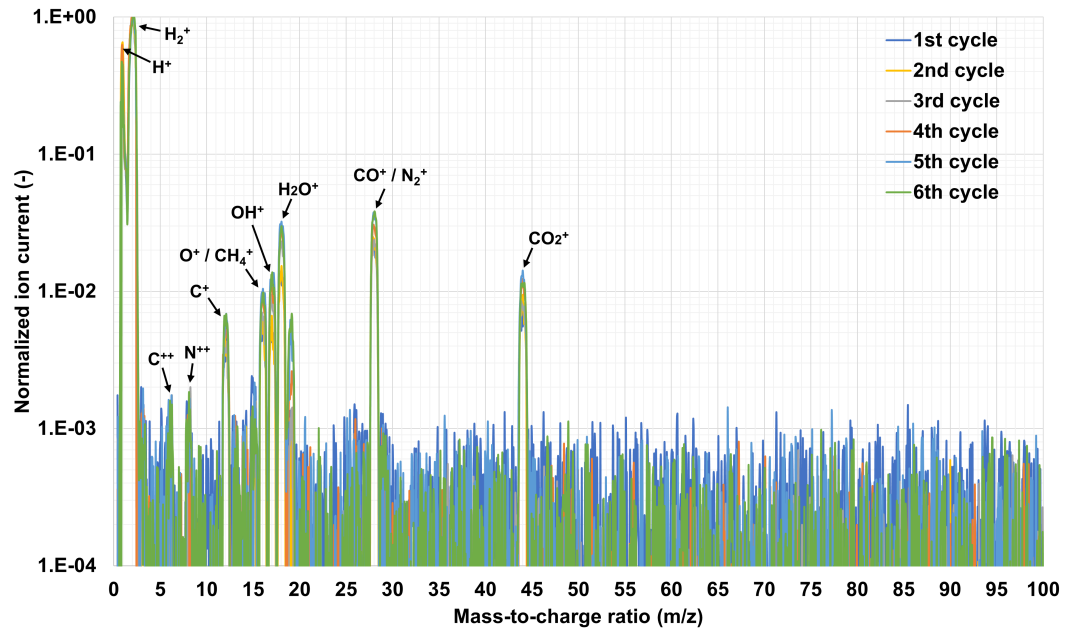


**Figure A.7:** Normalized mass-to-charge spectra showing the composition of vacuum throughout the high pressure experimental cycles measured 24 h after cooling down to room temperature after the activation in each cycle

		Ti	Zr	V	O	N	C	Na
HP-0	20°C	0.048	0.09	0.107	0.543	0.021	0.191	-
	160°C	0.059	0.11	0.107	0.515	0.019	0.192	-
	200°C	0.073	0.155	0.142	0.458	0.032	0.149	-
	250°C	0.103	0.186	0.242	0.218	0.039	0.212	-
HP-1	20°C	0.047	0.071	0.085	0.479	0.022	0.288	0.008
	160°C	0.059	0.096	0.103	0.46	0.014	0.255	0.012
	200°C	0.08	0.138	0.145	0.332	0.023	0.268	0.014
	250°C	0.091	0.149	0.16	0.299	0.025	0.263	0.013
HP-2	20°C	0.046	0.079	0.085	0.503	0.019	0.257	0.009
	160°C	0.05	0.092	0.093	0.487	0.016	0.25	0.009
	200°C	0.063	0.108	0.084	0.461	0.015	0.258	0.009
	250°C	0.073	0.136	0.118	0.392	0.02	0.254	0.009
HP-3	20°C	0.06	0.101	0.095	0.533	0.011	0.199	-
	160°C	0.071	0.117	0.104	0.517	0.011	0.179	-
	200°C	0.077	0.138	0.101	0.495	0.017	0.173	-
	250°C	0.078	0.146	0.103	0.482	0.02	0.172	-
HP-4	20°C	0.057	0.096	0.083	0.526	0	0.223	0.017
	160°C	0.064	0.11	0.094	0.514	0.008	0.199	0.011
	200°C	0.072	0.129	0.089	0.48	0.012	0.207	0.012
	250°C	0.08	0.142	0.087	0.463	0.008	0.207	0.014
HP-5	20°C	0.057	0.097	0.074	0.479	0	0.288	0.006
	160°C	0.063	0.108	0.08	0.467	0.004	0.271	0.007
	200°C	0.067	0.121	0.071	0.446	0.004	0.283	0.008
	250°C	0.066	0.136	0.078	0.437	0.005	0.27	0.008
HP-6	20°C	0.058	0.115	0.086	0.468	0.007	0.25	0.007
	160°C	0.064	0.127	0.091	0.438	0.007	0.267	0.007
	200°C	0.064	0.134	0.095	0.4	0.01	0.281	0.007
	250°C	0.063	0.14	0.105	0.41	0.009	0.257	0.007

**Table A.5:** Elemental surface composition in mole fractions of the witness samples from the high pressure experiment as measured with X-ray photoelectron spectroscopy (XPS) in as-received condition at room temperature (20 °C), and after 1 h in-situ activations at temperatures of 160 °C, 200 °C, and 250 °C

Spectral line	Binding energy (eV)
C 1s (in C–C bond)	284.5
C 1s (in O–C=O bond)	288.5
C 1s (in TiC)	281.6
C 1s (in VC)	282.2
C 1s (in ZrC)	281.1
O 1s (in V <sub>2</sub> O <sub>5</sub> )	529.9
O 1s (in TiO <sub>2</sub> )	529.9
O 1s (in ZrO <sub>2</sub> )	530.1
Ti 2p <sub>3/2</sub> (metal)	454.1
Ti 2p <sub>3/2</sub> (in TiO <sub>2</sub> )	458.8
V 2p <sub>3/2</sub> (metal)	512.2
V 2p <sub>3/2</sub> (in VO)	513
V 2p <sub>3/2</sub> (in V <sub>2</sub> O <sub>3</sub> )	515.7
V 2p <sub>3/2</sub> (in VO <sub>2</sub> )	516.3
V 2p <sub>3/2</sub> (in V <sub>2</sub> O <sub>5</sub> )	517.4
Zr 3d <sub>5/2</sub> (metal)	178.9
Zr 3d <sub>5/2</sub> (in ZrO <sub>2</sub> )	182.2

**Table A.6:** Reference spectral lines for the analysis of the XPS results from [33, 57, 73]

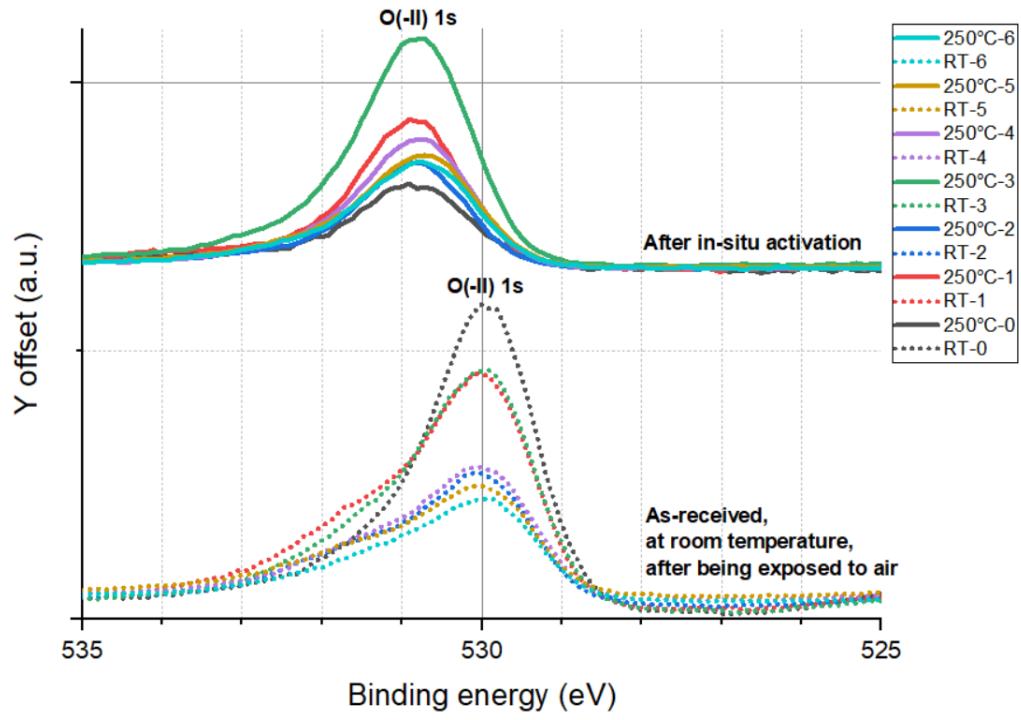


**Figure A.8:** X-ray photoelectron spectroscopy spectra of the O 1s peaks of the witness samples in as-received condition and after the in-situ activation



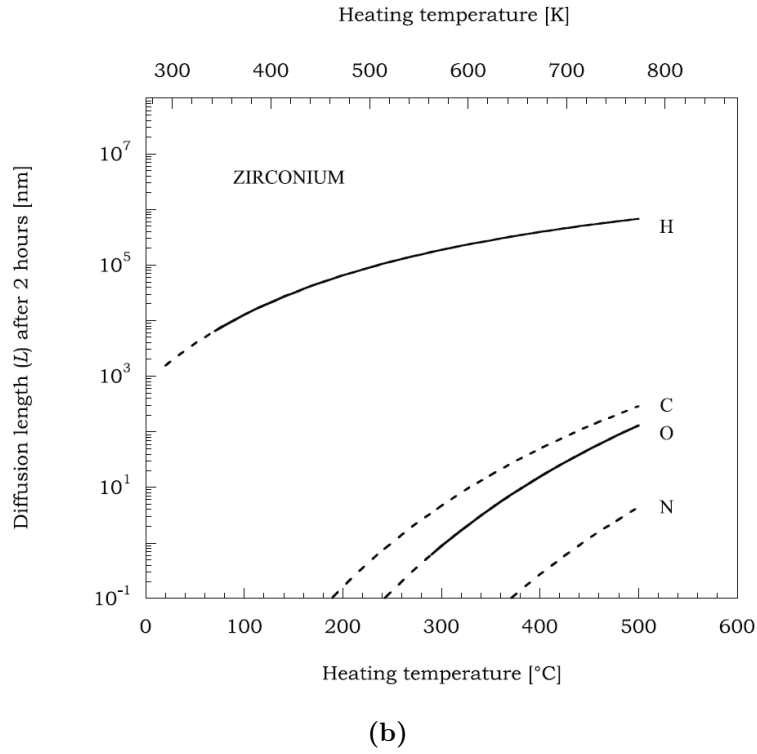
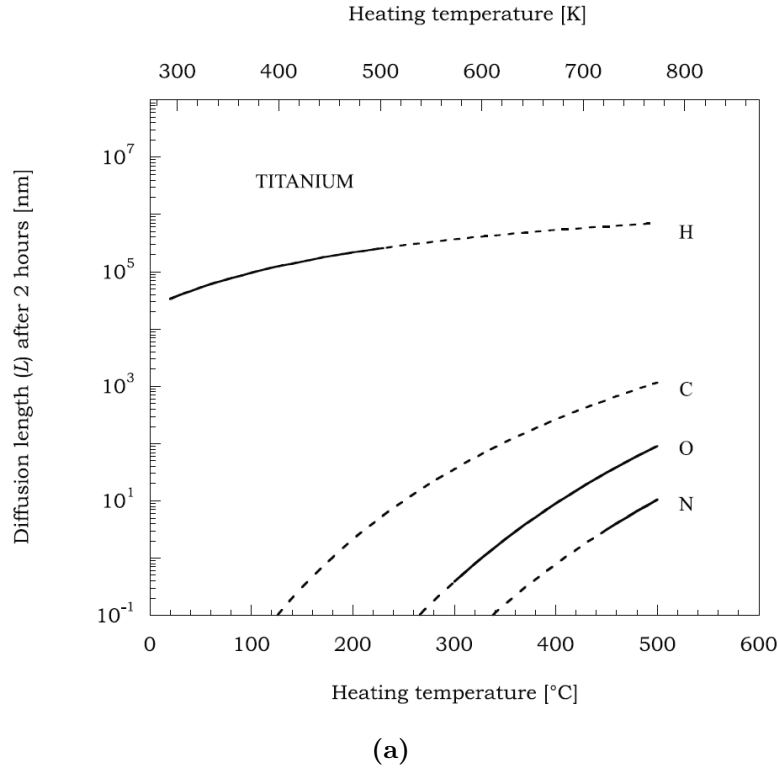


**Figure A.9:** Diffusion length after 2 h for H, C, O, and N in Ti (a), Zr (b), and V (c) as a function of heating temperature, with extrapolated data in dashed lines [4]

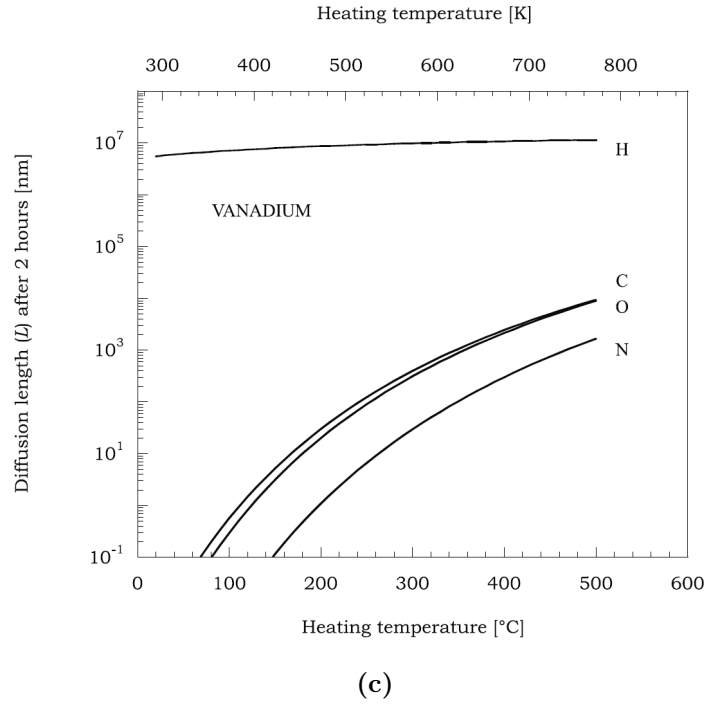


**Figure A.9:** Diffusion length after 2 h for H, C, O, and N in Ti (a), Zr (b), and V (c) as a function of heating temperature, with extrapolated data in dashed lines [4] (cont.)

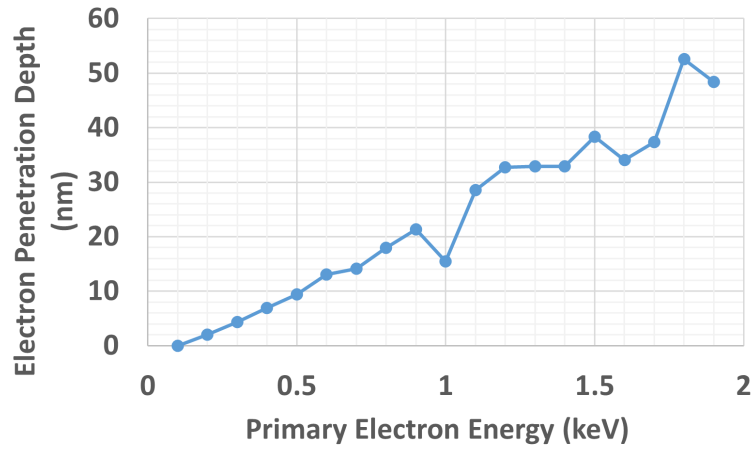


**Figure A.10:** Electron penetration depth as a function of incident electron energy from simulations with Casino software on a multilayer of 1000 nm  $\text{Ti}_{31}\text{Zr}_{18}\text{V}_{52}$  on top of a 304L stainless steel substrate

## A.3.2 Low Pressure Experiment

		Ti	Zr	V	O	N	C	Na	K
<b>LP-0</b>	20°C	0.070	0.097	0.083	0.527	0.022	0.187	0.010	0.005
	160°C	0.085	0.143	0.101	0.460	0.022	0.168	0.012	0.009
	200°C	0.146	0.199	0.183	0.156	0.044	0.257	0.007	0.008
	250°C	0.144	0.199	0.184	0.144	0.042	0.269	0.013	0.005
<b>LP-0A</b>	20°C	0.071	0.098	0.073	0.509	0.005	0.194	0.027	0.022
	160°C	0.078	0.109	0.079	0.485	0.004	0.202	0.021	0.023
	200°C	0.090	0.129	0.092	0.438	0.008	0.195	0.024	0.025
	250°C	0.121	0.186	0.132	0.242	0.018	0.263	0.024	0.014
<b>LP-1</b>	20°C	0.060	0.089	0.065	0.480	0.006	0.263	0.032	0.006
	160°C	0.073	0.108	0.072	0.410	0.008	0.295	0.029	0.006
	200°C	0.093	0.159	0.102	0.237	0.023	0.352	0.031	0.003
	250°C	0.112	0.162	0.108	0.191	0.025	0.373	0.025	0.003

**Table A.7:** Elemental surface composition in mole fractions of the witness samples from the low pressure experiment as measured with XPS in as-received condition at room temperature (20 °C), and after 1 h in-situ activations at temperatures of 160 °C, 200 °C, and 250 °C



# Bibliography

- [1] G. Apollinari, O. Brüning, T. Nakamoto, and L. Rossi, “High luminosity large hadron collider HL-LHC,” *arXiv preprint arXiv:1705.08830*, 2017.
- [2] P. Chiggiato and P. C. Pinto, “Ti–Zr–V non-evaporable getter films: From development to large scale production for the large hadron collider,” *Thin Solid Films*, vol. 515, no. 2, pp. 382–388, 2006.
- [3] A. Prodromides, C. Scheuerlein, and M. Taborelli, “Lowering the activation temperature of TiZrV non-evaporable getter films,” *Vacuum*, vol. 60, no. 1-2, pp. 35–41, 2001.
- [4] A. Prodromides, “Non-evaporable getter thin film coatings for vacuum applications,” Ph.D. dissertation, Ecole Nat. Sup. Ing. Caen, 2002.
- [5] C. Benvenuti, P. Chiggiato, A. Mongelluzzo, A. Prodromides, V. Ruzinov, C. Scheuerlein, M. Taborelli, and F. Lévy, “Influence of the elemental composition and crystal structure on the vacuum properties of Ti–Zr–V nonevaporable getter films,” *Journal of Vacuum Science & Technology A: Vacuum, Surfaces, and Films*, vol. 19, no. 6, pp. 2925–2930, 2001.
- [6] K. Welch, *Capture pumping technology*. Elsevier, 2001.
- [7] F. Mazzolini, “The use of NEG pumps and coatings in large vacuum systems: experience and limitations,” 2007.
- [8] P. C. Pinto, S. Calatroni, P. Chiggiato, H. Neupert, W. Vollenberg, E. Shaposhnikova, M. Taborelli, and C. Y. Vallgren, “Thin film coatings for suppressing electron multipacting in particle accelerators,” in *Proceedings of 2011 Particle Accelerator Conference, New York, NY, USA*, vol. 40, 2011.
- [9] P. C. Pinto, “History and potential of non evaporable getter (NEG) technology,” in *Workshop on Advanced Materials and Surfaces, CERN, Geneva, Switzerland*, 2013.
- [10] H.-C. Hseuh, C. Hetzel, S. Leng, K. Wilson, H. Xu, and D. Zigrosser, “National synchrotron light source II storage ring vacuum systems,” *Journal of Vacuum Science & Technology A: Vacuum, Surfaces, and Films*, vol. 34, no. 3, p. 031603, 2016.

- [11] P. F. Tavares, E. Al-Dmour, Å. Andersson, F. Cullinan, B. N. Jensen, D. Olsson, D. K. Olsson, M. Sjöström, H. Tarawneh, S. Thorin *et al.*, “Commissioning and first-year operational results of the MAX IV 3 GeV ring,” *Journal of synchrotron radiation*, vol. 25, no. 5, pp. 1291–1316, 2018.
- [12] G. Bregliozzi, J. Hansen, V. Baglin, J. Jiménez, S. Blanchard, and K. Weiss, “Achievement and evaluation of the beam vacuum performance of the LHC long straight sections,” Tech. Rep., 2008.
- [13] A. Chambers, *Modern vacuum physics*. CRC Press, 2004.
- [14] T. Giorgi, B. Ferrario, and B. Storey, “An updated review of getters and gettering,” *Journal of Vacuum Science & Technology A: Vacuum, Surfaces, and Films*, vol. 3, no. 2, pp. 417–423, 1985.
- [15] G. Bregliozzi, V. Baglin, T. Porcelli, G. Lanza, and J. Jimenez, “Evaluation of the NEG coating saturation level after 3 years of LHC beam operation,” in *Conf. Proc.*, vol. 130512, no. CERN-ACC-2013-0090, 2013, p. THPFI049.
- [16] C. Benvenuti, “Getter pumping,” *R&B Energy Research, Geneva, Switzerland*, 2007.
- [17] P. C. Pinto, “Vacuum chambers for lhc lss,” in *TS Workshop, Archamps*, 2004.
- [18] P. Chiggiato, “Outgassing properties of vacuum materials for particle accelerators,” *arXiv preprint arXiv:2006.07124*, 2020.
- [19] R. Knize and J. Cecchi, “Theory of bulk gettering,” *Journal of Applied Physics*, vol. 54, no. 6, pp. 3183–3189, 1983.
- [20] C. B. Nakhosteen and K. Jousten, *Handbook of vacuum technology*. John Wiley & Sons, 2016.
- [21] P. Manini and E. Maccallini, “NEG pumps: Sorption mechanisms and applications,” *arXiv preprint arXiv:2006.01537*, 2020.
- [22] A. Bursche, G. Manca, N. Neri, F. Fleuret, M. Schmelling, P. Robbe, H. P. Dembinski, G. Graziani, L. L. Pappalardo, M. Ferro-Luzzi *et al.*, “Physics opportunities with the fixed-target program of the LHCb experiment using an unpolarized gas target,” Tech. Rep., 2018.
- [23] O. Steinkamp, L. Collaboration *et al.*, “LHCb upgrades,” in *Journal of Physics: Conference Series*, vol. 1271, no. 1. IOP Publishing, 2019, p. 012010.
- [24] L. Collaboration *et al.*, “LHCb SMOG upgrade,” Tech. Rep., 2019.
- [25] P. Di Nezza, B. K. Popovic, C. Vollinger, G. Bregliozzi, A. Vasilyev, G. Ciullo, G. Iadarola, C. Zannini, E. Steffens, P. M. Gebolis *et al.*, “The SMOG2 project,” Tech. Rep., 2018.

- 
- [26] E. Mobs, “The CERN accelerator complex – 2019,” <https://cds.cern.ch/record/2684277>, 2019, [Online; accessed 17-Dec-2021].
- [27] D. J. Hucknall and A. Morris, *Vacuum technology: calculations in chemistry*. Royal society of chemistry, 2003.
- [28] P. Chiggiato, “Vacuum technology for particle accelerators,” *molecules*, vol. 900, p. 3, 2016.
- [29] C. Benvenuti, P. Chiggiato, P. C. Pinto, A. E. Santana, T. Hedley, A. Mongeluzzo, V. Ruzinov, and I. Wevers, “Vacuum properties of TiZrV non-evaporable getter films,” *Vacuum*, vol. 60, no. 1-2, pp. 57–65, 2001.
- [30] P. C. Pinto, B. Bartova, B. Holliger, S. M. Dos Santos, V. Nistor, A. Sapountzis, M. Taborrelli, I. Wevers, S. J. Ahlbäck, E. Al Dmour *et al.*, “Development and production of non evaporable getter coatings for the vacuum chambers of the 3 GeV storage ring of MAX IV,” *Proceedings of IPAC, (Richmond, USA)*, p. 3145, 2015.
- [31] T. Porcelli, M. Puro, S. Raimondi, F. Siviero, E. Maccallini, P. Manini, and G. Bongiorno, “NEG coating deposition and characterisation of narrow-gap insertion devices and small-diameter chambers for light sources and particle accelerators,” *Vacuum*, vol. 138, pp. 157–164, 2017.
- [32] C. Benvenuti *et al.*, “Non-evaporable getters: from pumping strips to thin film coatings,” in *EPAC*, vol. 98, 1998, pp. 200–204.
- [33] C. Scheuerlein, “The activation of non-evaporable getters monitored by AES, XPS, SSIMS and secondary electron yield measurements,” Ph.D. dissertation, School of Engineering, U. Surrey, Guildford, 2002.
- [34] C. Benvenuti, J. Cazeneuve, P. Chiggiato, F. Cicoira, A. E. Santana, V. Johaneck, V. Ruzinov, and J. Fraxedas, “A novel route to extreme vacua: the non-evaporable getter thin film coatings,” *Vacuum*, vol. 53, no. 1-2, pp. 219–225, 1999.
- [35] S. G. Sammartano, “Outgassing rates of PEEK, Kapton® and Vespel® polymers,” 2020.
- [36] R. Kersevan, “Ageing of non-evaporable getter (NEG) thin film coatings,” in *BPPC Meeting*, 2013.
- [37] Y. Fukai, *The metal-hydrogen system: basic bulk properties*. Springer Science & Business Media, 2006, vol. 21.
- [38] P. Modi and K.-F. Aguey-Zinsou, “Room temperature metal hydrides for stationary and heat storage applications: A review,” *Frontiers in Energy Research*, vol. 9, p. 128, 2021.

- [39] A. San-Martin and F. Manchester, “The H-Ti (hydrogen-titanium) system,” *Bulletin of alloy phase diagrams*, vol. 8, no. 1, pp. 30–42, 1987.
- [40] E. Zuzek, J. Abriata, A. San-Martin, and F. Manchester, “The H-Zr (hydrogen-zirconium) system,” *Bulletin of alloy phase diagrams*, vol. 11, no. 4, pp. 385–395, 1990.
- [41] G. K. Pálsson, “Influence of self-trapping, clamping and confinement on hydrogen absorption,” Ph.D. dissertation, Acta Universitatis Upsaliensis, 2011.
- [42] J. Crank, *The mathematics of diffusion*. Oxford university press, 1979.
- [43] T. Chapman, D. Dye, and D. Rugg, “Hydrogen in Ti and Zr alloys: industrial perspective, failure modes and mechanistic understanding,” *Philosophical Transactions of the Royal Society A: Mathematical, Physical and Engineering Sciences*, vol. 375, no. 2098, p. 20160418, 2017.
- [44] A. Efron, Y. Lifshitz, I. Lewkowicz, and M. Mintz, “The kinetics and mechanism of titanium hydride formation,” *Journal of the Less Common Metals*, vol. 153, no. 1, pp. 23–34, 1989.
- [45] A. Andreasen, “Predicting formation enthalpies of metal hydrides,” 2004.
- [46] J. Kapischke and J. Hapke, “Measurement of the pressure-composition isotherms of high-temperature and low-temperature metal hydrides,” *Experimental thermal and fluid science*, vol. 18, no. 1, pp. 70–81, 1998.
- [47] J. Bloch and M. H. Mintz, “Kinetics and mechanisms of metal hydrides formation—a review,” *Journal of Alloys and Compounds*, vol. 253, pp. 529–541, 1997.
- [48] S. Lynch, “Hydrogen embrittlement phenomena and mechanisms,” *Corrosion reviews*, vol. 30, no. 3-4, pp. 105–123, 2012.
- [49] O. Barrera, D. Bombac, Y. Chen, T. Daff, E. Galindo-Nava, P. Gong, D. Haley, R. Horton, I. Katzarov, J. Kermode *et al.*, “Understanding and mitigating hydrogen embrittlement of steels: a review of experimental, modelling and design progress from atomistic to continuum,” *Journal of materials science*, vol. 53, no. 9, pp. 6251–6290, 2018.
- [50] W. Qin, J. Szpunar, and J. Kozinski, “Hydride-induced degradation of zirconium alloys: a criterion for complete ductile-to-brittle transition and its dependence on microstructure,” *Proceedings of the Royal Society A: Mathematical, Physical and Engineering Sciences*, vol. 471, no. 2182, p. 20150192, 2015.
- [51] M. Malinowski, “Decreases in deuterium pumping by St707 getter alloy caused by carbon dioxide preexposure,” *Journal of Vacuum Science & Technology A: Vacuum, Surfaces, and Films*, vol. 3, no. 3, pp. 483–486, 1985.

- 
- [52] A. Santucci, L. Farina, S. Tosti, and A. Frattolillo, “Novel non-evaporable getter materials and their possible use in fusion application for tritium recovery,” *Molecules*, vol. 25, no. 23, p. 5675, 2020.
- [53] CERN, “Thin film coatings for improved vacuum performance,” <https://knowledge-transfer.web.cern.ch/technologies/thin-film-coatings-improved-vacuum-performance>, 2022, [Online; accessed 17-Dec-2021].
- [54] V. Baglin, P. Chiggiato, C. Garion, and G. Riddone, “Vacuum system,” *CERN Yellow Reports: Monographs*, vol. 10, pp. 229–229, 2020.
- [55] “Operating procedure for chemical degreasing of parts for high-vacuum and ultra-high-vacuum applications.” [Online]. Available: [https://edms.cern.ch/ui/file/1390437/2/Degreasing\\_procedure\\_UHV\\_parts\\_doc\\_cp.pdf](https://edms.cern.ch/ui/file/1390437/2/Degreasing_procedure_UHV_parts_doc_cp.pdf)
- [56] K. Jousten, “Pressure measurement with ionization gauges,” *CERN EUROPEAN ORGANIZATION FOR NUCLEAR RESEARCH-REPORTS-CERN*, pp. 75–88, 1999.
- [57] A. V. Naumkin, A. Kraut-Vass, S. W. Gaarenstroom, and C. J. Powell, “NIST standard reference database 20, version 4.1,” *The National Institute of Standards and Technology NIST*, pp. 1–49, 2012.
- [58] R. Cimino and T. Demma, “Electron cloud in accelerators,” *International Journal of Modern Physics A*, vol. 29, no. 17, p. 1430023, 2014.
- [59] L. Lutterotti, “Total pattern fitting for the combined size–strain–stress–texture determination in thin film diffraction,” *Nuclear Instruments and Methods in Physics Research Section B: Beam Interactions with Materials and Atoms*, vol. 268, no. 3-4, pp. 334–340, 2010.
- [60] P. C. Pinto, “EDMS N.2104700: Studies on the ageing of NEG films,” <https://edms.cern.ch/document/2104700/1>, internal document (restricted access).
- [61] G. L. Doll and P. J. Shiller, “Thermal desorption spectroscopy,” 2019.
- [62] “Thermo-Calc software version 2022a, TCTI2: Ti-alloys database version 2.2.” [Online]. Available: <https://thermocalc.com/>
- [63] D. Drouin, A. R. Couture, D. Joly, X. Tastet, V. Aimez, and R. Gauvin, “Casino v2. 42—a fast and easy-to-use modeling tool for scanning electron microscopy and microanalysis users,” *Scanning: The Journal of Scanning Microscopies*, vol. 29, no. 3, pp. 92–101, 2007.
- [64] M. Ady, R. Kersevan *et al.*, “Introduction to the latest version of the test-particle monte carlo code molflow+,” *Proc. of IPAC*, p. 2348, 2014.

- [65] R. Kersevan, M. Ady *et al.*, “Recent developments of Monte-Carlo codes molflow+ and synrad+,” in *Proceedings of the 10th International Particle Accelerator Conference (IPAC’19), Melbourne, Australia*, 2019, pp. 19–24.
- [66] M. Ady, “Monte Carlo simulations of ultra high vacuum and synchrotron radiation for particle accelerators,” EPFL, Tech. Rep., 2016.
- [67] C. Barcellini, “Non evaporable getter thin film coatings for vacuum applications,” 2014.
- [68] R. Alvarez, J. M. Garcia-Martin, M. C. Lopez-Santos, V. Rico, F. J. Ferrer, J. Cotrino, A. R. Gonzalez-Elipe, and A. Palmero, “On the deposition rates of magnetron sputtered thin films at oblique angles,” *Plasma Processes and Polymers*, vol. 11, no. 6, pp. 571–576, 2014.
- [69] N. Nedfors, D. Primetzhofer, I. Zhirkov, J. Palisaitis, P. O. Persson, J. E. Greene, I. Petrov, and J. Rosen, “The influence of pressure and magnetic field on the deposition of epitaxial thin films from dc magnetron sputtering,” *Vacuum*, vol. 177, p. 109355, 2020.
- [70] A. Rossi, “H<sub>2</sub> equilibrium pressure with a neg-coated vacuum chamber as a function of temperature and h<sub>2</sub> concentration,” Tech. Rep., 2006.
- [71] H. Sharifi, M. Aliofkhazraei, G. B. Darband, and S. Shrestha, “A review on adhesion strength of peo coatings by scratch test method,” *Surface Review and Letters*, vol. 25, no. 03, p. 1830004, 2018.
- [72] M. Hasegawa, “Ellingham diagram,” in *Treatise on Process Metallurgy*. Elsevier, 2014, pp. 507–516.
- [73] E. Hryha, E. Rutqvist, and L. Nyborg, “Stoichiometric vanadium oxides studied by XPS,” *Surface and interface analysis*, vol. 44, no. 8, pp. 1022–1025, 2012.
- [74] F. Ruiz, Z. Benzo, Á. Garaboto, J. Salas, and J. L. Brito, “Xps characterization of vanadium carbide species formed during the atomization process in electrothermal atomic absorption spectroscopy,” *Journal of Analytical Atomic Spectrometry*, vol. 37, no. 3, pp. 668–676, 2022.
- [75] B. Henrist, N. Hilleret, C. Scheuerlein, and M. Taborrelli, “The secondary electron yield of TiZr and TiZrV non-evaporable getter thin film coatings,” *Applied surface science*, vol. 172, no. 1-2, pp. 95–102, 2001.
- [76] T. French, “The secondary electron yield of non-evaporable getter films for repeated activation/venting cycles,” internal document (restricted access).
- [77] V. Baglin, J. Bojko, C. Scheuerlein, O. Gröbner, M. Taborrelli, B. Henrist, and N. Hilleret, “The secondary electron yield of technical materials and its variation with surface treatments,” Tech. Rep., 2000.

- 
- [78] D. Bajek, S. Wackerow, D. Zanin, L. Baudin, K. Bogdanowicz, E. Valdivieso, S. Calatroni, B. Di Girolamo, M. Sitko, M. Himmerlich *et al.*, “Role of surface microgeometries on electron escape probability and secondary electron yield of metal surfaces,” *Scientific reports*, vol. 10, no. 1, pp. 1–8, 2020.
- [79] K. Nishimura, T. Itotani, and K. Ohya, “Influence of surface roughness on secondary electron emission and electron backscattering from metal surface,” *Japanese journal of applied physics*, vol. 33, no. 8R, p. 4727, 1994.
- [80] L. Liu, G. Feng, B. Chen, N. Wang, and W. Cui, “Characteristics of secondary electron emission and multipactor from a nested microtrap structure surface,” *AIP Advances*, vol. 11, no. 2, p. 025332, 2021.
- [81] M. Taborrelli, “Secondary electron yield of surfaces: what we know and what we still need to know,” in *CERN Yellow Reports: Conference Proceedings*, vol. 7, 2020, pp. 97–97.
- [82] A. Shih, J. Yater, C. Hor, and R. Abrams, “Secondary electron emission studies,” *Applied surface science*, vol. 111, pp. 251–258, 1997.
- [83] C. Borchers, T. Khomenko, A. Leonov, and O. Morozova, “Interrupted thermal desorption of  $\text{TiH}_2$ ,” *Thermochimica acta*, vol. 493, no. 1-2, pp. 80–84, 2009.
- [84] M. Ma, W. Xiang, B. Tang, L. Liang, L. Wang, and X. Tan, “Non-isothermal and isothermal hydrogen desorption kinetics of zirconium hydride,” *Journal of Nuclear Materials*, vol. 467, pp. 349–356, 2015.
- [85] S. Kumar, A. Jain, and Y. Kojima, “Thermodynamics and kinetics of hydrogen absorption–desorption of vanadium synthesized by aluminothermy,” *Journal of Thermal Analysis and Calorimetry*, vol. 130, no. 2, pp. 721–726, 2017.
- [86] K. Verbeken, “Analysing hydrogen in metals: bulk thermal desorption spectroscopy (tds) methods,” in *Gaseous hydrogen embrittlement of materials in energy technologies*. Elsevier, 2012, pp. 27–55.
- [87] M. Ozerov, D. Klimenko, L. Rtishcheva, V. Kopylov, N. Stepanov, and S. Zhrebtssov, “Effect of carbon on microstructure and mechanical properties of titanium,” in *IOP Conference Series: Materials Science and Engineering*, vol. 1014, no. 1. IOP Publishing, 2021, p. 012039.
- [88] S. Kovacevic, R. Pan, D. Sekulic, and S. D. Mesarovic, “Interfacial energy as the driving force for diffusion bonding of ceramics,” *Acta Materialia*, vol. 186, pp. 405–414, 2020.
- [89] V. Lipatnikov, A. Gusev, P. Ettmeier, and W. Lengauer, “Order-disorder phase transformations and specific heat of nonstoichiometric vanadium carbide,” *Physics of the Solid State*, vol. 41, no. 3, pp. 474–480, 1999.

- [90] A. Bonucci, A. Conte, P. Manini, and S. Raimondi, “The transmission factor method: in-situ characterization of getter coated pipes,” in *AIP Conference Proceedings*, vol. 879, no. 1. American Institute of Physics, 2007, pp. 432–435.